Aus dem Institut für Neurowissenschaft und Medizin–7
des Forschungszentrums Jülich
Direktor: Universitätsprofessor Dr. med. Dr. rer. nat. P. A. Tass

Mechanismen der Multistabilität neuronaler Synchronisation und ihre effektive Kontrolle mittels Coordinated Reset Stimulation

Inaugural-Dissertation zur Erlangung
der Würde eines doctor rerum medicinalium
der Hohen Medizinischen Fakultät
der Universität zu Köln

vorgelegt von
Borys Lysyansky
aus Kiew/Ukraine

Promoviert am: 24.02.2010

Gedruckt mit Genehmigung der
Medizinischen Fakultät der Universität zu Köln

2010

Druck & Bindung
Graphische Betriebe, Forschungszentrum Jülich
52425 Jülich

Dekan: Universitätsprofessor Dr. med. J. Klosterkötter

1. Berichterstatter: Universitätsprofessor Dr. med. Dr. rer. nat. P. A. Tass
2. Berichterstatter: Universitätsprofessor Dr. med. L. Timmermann

Erklärung

Ich erkläre hiermit, dass ich die vorliegende Arbeit ohne unzulässige Hilfe Dritter und ohne Benutzung anderer als der angegebenen Hilfsmittel angefertigt habe; die aus fremden Quellen direkt oder indirekt übernommenen Gedanken sind als solche kenntlich gemacht.

Bei der Auswahl und Auswertung des Materials sowie bei der Herstellung des Manuskriptes habe ich keine Unterstützungen erhalten.

Weitere Personen waren an der geistigen Herstellung der vorliegenden Arbeit nicht beteiligt. Insbesondere habe ich nicht die Hilfe eines Promotionsberaters in Anspruch genommen. Dritte haben von mir weder unmittelbar noch mittelbar geldwerte Leistungen für Arbeit erhalten, die im Zusammenfassung mit dem Inhalt der vorgelegten Dissertation stehen.

Die Arbeit wurde von mir bisher weder im Inland noch im Ausland in gleicher oder ähnlicher Form einer anderen Prüfungsbehörde vorgelegt und ist auch noch nicht veröffentlicht.

Köln, den 28. April 2009 Borys Lysyansky

Acknowledgements

I am grateful to Prof. Dr. Dr. Peter A. Tass from the Research Center Juelich for supervising my work and for his scientific stimulations, which were of high importance for me during the writing of the thesis.

I would like to thank PD Dr. Oleksandr Popovych for his undiminishing interest to my work, for his advices concerning nonlinear dynamics and for a general support during my work.

I would like also to thank all my collegues at the INM-7, Research Center Juelich for their help.

Table of Contents

Table of Contents **v**

Index of figures **viii**

1 Introduction **1**

1.1 Mathematical models in neuroscience 7

1.1.1 General characteristics of neurons 7

1.1.2 Classification of mathematical neuronal models 10

1.2 Structure of the thesis 15

2 The Kuramoto model with synaptic plasticity **18**

2.1 The Kuramoto system of coupled oscillators 18

Order parameter 20

2.2 Spike timing-dependent plasticity and its model 23

2.3 The role of STDP asymmetry 27

2.4 Properties of the synchronized state 33

2.5 Multistability in system of $N = 3$ oscillators 35

2.6 High-dimensional systems 37

2.7 Conclusions 40

3 Multistability in the delayed Kuramoto model **42**

3.1 Kuramoto model with delayed interaction 43

3.1.1 Detecting synchronized states 45

3.1.2 Coexistence of different stable modes 48

3.1.3 Basins of attraction of synchronized states 52

3.2 The delayed Kuramoto model with feedback 55
3.2.1 Model and its synchronized solutions 55
3.2.2 Special features of the delayed model with feedback 56
3.3 Conclusions 64

4 Coordinated Reset Stimulation **66**
4.1 Coordinated Reset of the system of phase oscillators 68
4.1.1 Model of the CR stimulation 68
4.1.2 Resetting properties of CR stimulation 76
4.1.3 Averaged state of the model under permanent CR stimulation 82
4.1.4 Post-stimulus transient dynamics 87
4.1.5 Effect of frequency mismatch on CR stimulation 99
4.1.6 On-Off stimulation 105
4.2 CR stimulation of FitzHugh-Nagumo neurons 113
4.2.1 The FitzHugh-Nagumo model 113
4.2.2 FitzHugh-Nagumo neurons under CR stimulation: model description 117
4.2.3 Estimation of CR stimulation effect 119
4.3 Conclusions 124

5 Conclusions **126**
Prospects 131

6 Summary **132**

7 Zusammenfassung **134**

8 References **137**

9 Preliminary publications **149**

10 Lebenslauf **150**

List of Figures

1.1 Schematic model of the basal ganglia 3

1.2 Schematic model of the neuron 8

1.3 Illustration of the event-related phases 14

2.1 Schematic illustration of the order parameter 20

2.2 Properties of the first order parameter 22

2.3 Experimental observation of STDP 24

2.4 Averaged frequencies: symmetric and asymmetric learning rule for $N = 2, 3$ 28

2.5 STDP: Different dynamical modes in the plane (α, τ_p) 29

2.6 Vector field transformation: symmetric case $\tau_p = \tau_d$ 30

2.7 Vector field transformation: asymmetric case $\tau_p < \tau_d$ 31

2.8 Exemplary dynamics of coupling strengths in the desynchronized state 33

2.9 Multistability in the system of $N = 3$ oscillators 36

2.10 Coexistence of different modes for $N = 3$ and $\omega_2 = 1.4$ 37

2.11 Frequency diagram for the system of $N = 5$ oscillators 38

2.12 Frequency diagram for the system of $N = 10$; 20 oscillators 39

2.13 Estimation of sizes of basins of attraction, $N = 5$, 10 40

3.1 Finding frequencies of the synchronized states 46

3.2 Diagrams $\Omega(K)$ and $\alpha(K)$ 47
3.3 Eigenvalues: 3 different cases 48
3.4 Critical value $K_{\rm cr} = K_{\rm cr}(\tau)$ 49
3.5 Coexistence of synchronized and desynchronized modes for $\tau = 0.2$, $\tau = 0.6$, $\tau = 2$ 50
3.6 Coexistence of synchronized and desynchronized modes for $\tau = 5$, symmetric case 51
3.7 Averaged frequencies of the stable solutions on the plane (Ω_1, Ω_2), $\tau = 5, 10$. 52
3.8 Basins of attraction for the delayed Kuramoto model 54
3.9 Diagrams $\Omega = \Omega(K)$ and $\alpha = \alpha(K)$ for the delayed system with feedback 57
3.10 Spectra of the synchronized solution undergoing Hopf bifurcation . . 58
3.11 Graphs of $K_{\rm bif}(\overline{\omega})$ and $K_{\rm cr}(\overline{\omega})$ for different $\Delta\omega$ 59
3.12 Diagram of system behavior on the plane $(\overline{\omega}, K)$, identical oscillators 60
3.13 Diagram of system behavior on the plane $(\overline{\omega}, K)$, detuning $\Delta\omega = 3.25$ 61
3.14 Diagram of system states in the plane $(\Delta\omega, K)$, $\overline{\omega} \approx 13.86$ 62
3.15 The averaged frequencies of the stable solutions of the system with self-feedback 63
3.16 Effect of frequency discretization in the model with self-feedback . . . 64

4.1 Schematic model of the 4-contact stimulating electrode 69
4.2 4-contact stimulating electrode: oscillators and contacts 70
4.3 Decays of stimulation strengths for $N_c = 4$-contact system 72
4.4 Stimulation signals of the contacts 75
4.5 Impact of the permanent HF stimulation 77
4.6 Cross-trial analysis of the short-term HF stimulation 79

4.7 Different states of the phase model under CR stimulation 81
4.8 Oscillations of the order parameters $R_{1,4}$ during CR stimulation . . . 83
4.9 Averaged order parameters $\langle R_{1,4} \rangle$ 83
4.10 CR stimulation: clustered state 85
4.11 CR stimulation: desynchronized state 86
4.12 Phase distribution for desynchronized state 86
4.13 Illustration of the post-stimulus transient 88
4.14 Transient versus stimulation break 89
4.15 Transient time and the order parameters 91
4.16 Maximal averaged transient versus (I, σ) 92
4.17 The order parameters in the optimal moment of the stimulus break . 94
4.18 Transient versus (I, σ) after usual end of stimulation 95
4.19 Examples of time courses of Kuiper index 97
4.20 The averaged Kuiper index for the clusterizing CR stimulation 98
4.21 The averaged Kuiper index for the desynchronizing CR stimulation . 99
4.22 The order parameters $R_{1...4}$ versus stimulation period 100
4.23 System behavior for $T = 2.33$ 102
4.24 The Kuiper index for CR stimulation with $T = 2.33$, $T = 2$ 102
4.25 Stimulation periods: $T = 4$, 6, 8 105
4.26 On-off CR stimulation, signals of the contacts 107
4.27 On-off CR stimulation, time courses of R_1 108
4.28 On-off CR stimulation, results for the integer m, n values 108
4.29 Time courses of R_1 for different values of m 110
4.30 Effectiveness of on-off stimulation $r(n)$ for different values of m 110
4.31 On-Off CR stimulation, results for real m, n values 111

4.32 Nullclines of the FitzHugh-Nagumo model 114
4.33 Different dynamical states of the FitzHugh-Nagumo model 115
4.34 Dependence of the frequency of the FHN model on small parameter . 116
4.35 Smoothed Heaviside function, synaptic current 118
4.36 FHN trajectory and its phase 120
4.37 Mean field of the FHN-based model in different system states 121
4.38 The averaged order parameter $\langle R_1 \rangle$ vs. I: FHN-based model and phase-based model 123
4.39 Standard deviation of the mean field S_V vs. I 124

Chapter 1

Introduction

The aim of this thesis is to study multistability properties of synchronized neuronal dynamics caused by time-delayed coupling and spike-timing dependent plasticity, as well as to investigate theoretical models of deep brain stimulation (DBS) and their possible applications. The work is relevant not only from the mathematical point of view, but also for medical application, namely, for the development of novel brain stimulation techniques for the treatment of Parkinson's disease (PD) or essential tremor.

Parkinson's disease is a movement disorder characterized by a broad variety of symptoms, e.g., predominant resting tremor at a frequency range $4 - 8$ Hz, akinesia (inability to initiate movement) and rigidity (an increase in muscle tone leading to a resistance to passive movement throughout the range of motion). The pathological hallmark of this disease is the destruction of dopaminergic neurons leading to a decrease in the striatal dopamine content [9]. The neuronal mechanisms of parkinsonian resting tremor are nowadays rather unclear [17, 22].

We mention two hypotheses on mechanisms underlying parkinsonian symptoms. Both hypotheses involve the pathological neuronal activity in the basal ganglia. The basal ganglia are a group of subcortical brain nuclei involved in voluntary movement, association, emotion and cognition. Their schematic model is depicted in Figure 1.1. The key concepts for the basal ganglia are the *direct* and *indirect* pathways of the neuronal signaling [2]. The direct pathway is a neuronal circuit going directly

from striatum to the output of the basal ganglia, globus pallidus internal (GPi) and substantia nigra reticulata (SNr). This pathway is responsible for initiation and execution of voluntary movements. The indirect pathway is another circuit, connecting striatum and GPi with SNr via globus pallidus external (GPe)- subthalamic nucleus (STN) nuclei. This pathway helps to prevent unwanted muscle contractions from competing with voluntary movements. As mentioned above, Parkinson's disease is characterized by a decrease of dopamine contents in the striatum. This results in a depression of the direct pathway and an abnormal activation of the indirect pathway. We mention two hypotheses of the mechanisms of appearance of the symptoms of PD.

1. This hypothesis is based on the idea of a STN-GPe pacemaker, which is depicted in Figure 1.1 by dashed rectangle. It was shown by in vitro studies of the neuronal cultures from the brain of a rat [60] that significant part of neurons from STN and GPe demonstrate synchronized activity on several frequencies ranging from 0.4 to 1.8 Hz. The phase shifts between different synchronized neurons were either close to zero (in-phase oscillations) or to π (anti-phase oscillations). It was also revealed that both components of the excitatory-inhibitory loop are needed for the demonstrated strong synchronization. Since the above studies have been carried out under the condition of the dopamine depletion, it has been concluded that the conditions of this in vitro study were similar to the PD state. Thus, abnormal synchronization of the STN-GPe loop may cause symptoms of Parkinson's disease.

2. The second hypothesis is that basal ganglia loops lose their ability to separately process information [8, 57, 67]. This hypothesis is a result of in vivo studies of MPTP-treated monkeys. It has been revealed that neurons in different nuclei of basal ganglia demonstrate coherent firing, whereas they oscillate in an uncorrelated manner in a healthy monkey. Neuronal activity is synchronized not only within a single nucleus in basal ganglia, but also between different nuclei.

Summarizing both hypotheses, the most probable reason of the PD symptoms can be a pathological neuronal synchronization in the basal ganglia. Abnormally synchro-

nized activity may result in the increasing of the inhibiting GPi→thalamus output, which leads to akinesia and rigidity, whereas the strongly synchronized oscillations in the basal ganglia loops may cause parkinsonian tremor [9]. Moreover, a study of the directionality of the brain-muscle interaction [76] revealed a nonlinear driving of the muscles by the subcortical oscillations.

The characteristic property of the correlated neuronal activity in the basal ganglia is the change of the firing patterns of neurons. High-frequency tonic activity is usual for a healthy state, whereas low-frequency bursting in the basal ganglia is one of the characteristics of PD [12, 99]. Thus, rhythmic bursting activity at frequency bands $4-10$ Hz and $15-30$ Hz was observed in the STN, GPe and other parts of the basal ganglia [9, 16, 47, 57].

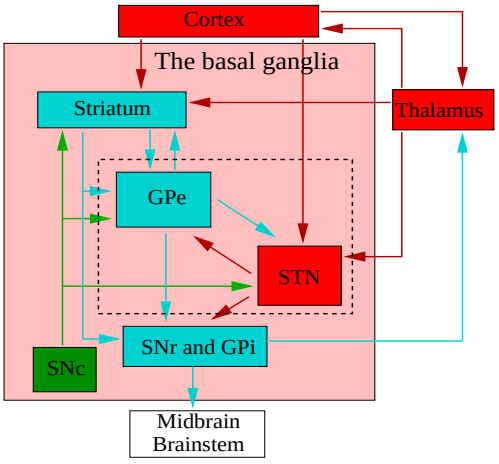

Figure 1.1: Schematic model of the basal ganglia. The basal ganglia is marked by rose rectangle. Green arrows depict the dopaminergic connections, red arrows depict the glutamatergic connections and blue arrows depict the GABAergic connections. Dashed box depicts the STN-GPe pacemaker.

Oscillations at tremor frequencies ($4-8$ Hz) are common in recordings of brain activities [9]. A significant coherence between STN neurons and muscle electromyogram (EMG) activities on the tremor frequencies has been shown [3]. Such coherence has been found to be significant for 76 out of 145 (52.4%) neurons, whereas the coherence in the beta band occured only in 10 out of 145 (6.9%) neurons. This

study also established that synchronous neuronal activity in subthalamic nucleus at the tremor frequency contributes to the pathogenesis of Parkinsonian tremor. The cerebro-muscular coherence during rest tremor was found not only in a tremor frequency range, but also in a double tremor frequency range [95]. On the other hand, the prominent high-frequency (15-30 Hz) synchronization has been revealed in the STN between different neurons [51].

We can conclude that strongly synchronized neuronal activity in the STN-GPe loop in the basal ganglia is involved in the pathogenesis of the PD symptoms generally. Along this line, there are studies showing that reduction of the synchrony in the basal ganglia is tightly connected with the clinical improvement in Parkinson's disease. Thus, it has been found [50] that dopaminergic medication reduces a high-frequency (15-30 Hz) synchrony between different STN cells. It was shown that a levodopa-induced reduction of the peak in the frequency band $8-35$ Hz is strongly positively correlated with an improvement of the motor score [17, 47] . Such a correlation supports the hypothesis that levodopa-induced suppression of synchronized oscillatory activity in a $8-35$ Hz band may be related to an improvement in Parkinsonism, e.g. akinesia and rigidity. Therefore, the suppression of the pathological synchronization is an important problem for the therapy of Parkinson's disease.

In the case of advanced PD or essential tremor where patients do not respond to drug therapy, depth electrodes are permanently implanted in target areas, such as ventral intermedius nucleus (Vim) or the subthalamic nucleus [5, 6, 15, 98]. The high-frequency electrical stimulation is administered via the implanted electrodes. High-Frequency (HF) DBS has been developed empirically based on intraoperative observations mainly. Nowadays HF DBS is the golden standard, but it may have some side effects, its clinical effect decreases with time, or the patients do not respond to this therapy in spite of the proper electrode placement [68].

In order to improve the deep brain stimulation and to avoid possible unwanted side effects, novel methods of stimulation based on nonlinear dynamics and statistical physics have been developed by P. Tass, O. Popovych and C. Hauptmann [30, 34, 35, 61, 79, 83–85].

The goal of these techniques based on resetting principles and delayed feedback is to

selectively counteract the pathological synchronization process. The advantages of the mentioned methods are their robustness with regard to the parameter variation and mildness, e.g., decay of the stimulation strength under the improving of the system state, i.e., breaking down the synchrony.

In previous papers [34, 90] several stimulation techniques were reviewed. The standard HF DBS is compared in a modelling approach with the following novel techniques

- coordinated reset (CR) stimulation,
- multisite delayed feedback (MDF) stimulation,
- nonlinear delayed feedback (NDF) stimulation.

The novel methods are based on the idea of suppression of the synchronization in the target neuronal area by re-establishing a normal physiological activity in a highly synchronized population of neurons. On the other hand, the outcome of the HF DBS is a significant modulation of the neuronal activity. It has been shown [72, 78] that the effect of the high-frequency stimulation is similar to the tissue lesioning, i.e., it results in the suppression of the neuronal activity, but with less pronounced unwanted side effects. It has been also revealed [24, 25] that HF DBS can induce effect resembling the overactivation of the neuronal firing with the frequency of the HF stimulation. HF DBS uses a high-frequency pulse train permanently applied via the stimulation electrode. The numerical simulations of the HF stimulation and its impact on the basal ganglia were performed in the work [70].

CR stimulation employs short pulse trains to sequentially reset the individual subpopulations of the neuronal network inducing clustered state. This type of stimulation is the main object of investigation in this thesis. The stimulation is applied via a small number of stimulation sites, which are equally spaced in the neuronal population. Stimulation signals administered via individual stimulation contacts induce the resetting of the neuronal subpopulation assigned to the corresponding stimulation site. Furthermore, in this thesis we will consider the dependence of stimulation effects on the stimulation parameters, such as stimulation intensity and spread of the electrical current in the brain tissue. The effect of desynchronization is achieved

here by utilizing self-organization principle [29] based on the slaving principle appeared due to the pathological neuronal interactions. We investigate a transient from the stimulation-induced clustered state to the synchronized state, which goes through the desynchronization [83].

During the last years many theoretical modeling studies [35, 36] have been devoted to coordinated reset stimulation. These works revealed that CR stimulation can achieve an effective desynchronization in neuronal networks. It was supposed that systems under consideration involve spike-timing dependent plasticity for the coupling strength. The important effects of rewiring and long-lasting desynchronization imposed by the CR stimulation have been found. Summarizing, we can conclude that CR stimulation is a perspective technique providing an effective desynchronization in neuronal population. The clinical study of coordinated reset stimulation is currently being performed at the Institute of Neuroscience and Medicine-Neuromodulation (INM-7), Research Center Juelich in collaboration with the Clinic for Stereotaxy and functional Neurosurgery of the University of Cologne.

The MDF stimulation and NDF stimulation techniques utilize delayed feedback to stabilize a desynchronized state, which is supposed to be the closest one to the physiological healthy state. The local field potential (LFP) of the population to be desynchronized is measured, preprocessed, multiplied by some factor, delayed and fed back into the target neuronal population.

Short description of MDF stimulation: The delayed LFP is applied via a small number of stimulating contacts where each administered stimulation signal has its own time delay. The temporal evolution of the delayed LFP signal controls the onset of cell bursting in the corresponding neuronal subarea. Providing the appropriate choose of time delays for all contacts, neuronal subpopulations from the vicinity of the corresponding sites start their activity at different times, which gives rise to the desynchronization. This method was described in the articles [30, 31].

Short description of NDF stimulation: The measured and delayed LFP is nonlinearly combined with the instantaneous signal and is applied via a single contact. Such combined signal compensates the synchronized synaptic input for all cells in the population and the synchronization is breaking down. Investigation of this method

was performed in works [61, 62].

The first goal of the present thesis is to study the coexistence of different states in the complex neuronal systems modeling neuronal networks with spike timing-dependent synaptic plasticity and interaction among neurons with time delay. Several coexisting states, which can be considered as desired (healthy) and undesired (pathological) modes of the neuronal activity, allow to switch the dynamics of neuronal population from the pathological to the healthy state. The coexistence of different states (multistability) means that these states are simultaneously stable for the same parameter values. Therefore, different initial conditions can give rise to the qualitatively different states. For the real applications multistability allows to obtain a long-lasting therapeutic effect of the stimulation. Indeed, if the system has been switched to the healthy state, it stays in this state for a long period of time.

Another part of the study is devoted to CR stimulation technique. This method provides an effective desynchronization of a strongly synchronized neuronal system even in the case of a single attracting pathological state, i.e., without coexistence of different states. The aim of the present study is to describe the mechanism of action and to find the optimal parameter values for this stimulation technique. As we will show in Chapter 4 different values of CR stimulation parameters can lead to different dynamical states. We study the efficiency of this stimulation in the corresponding Chapter for different parameter values. The main parameters, which need to be considered, are the intensity of the stimulation, the stimulation period and the coefficient of the current decay in the neuronal tissue with the distance to the stimulation site. We also consider the robustness of CR stimulation with respect to parameter variations in detail.

1.1 Mathematical models in neuroscience

1.1.1 General characteristics of neurons

During the last hundred years biological science has accumulated a huge amount of knowledge about the structure and functions of the human brain. The elementary

processing units of the central nervous system are *neurons*, and their connections form a very complex network. For example, in the cortex there are more than 10^4 cells and several kilometers of their "connections" per cubic millimeter [26]. Not only neurons, but also another types of cells, namely glia cells, which are involved into energy supply processes, are present in the cortex.

A typical neuron consists of three functionally different parts: *dendrites*, *soma* and *axon*, see Figure 1.2. Dendrites can be considered as 'input devices' of the neuron, collecting signals from other cells and transmitting them to the soma. The soma performs nonlinear signal processing in such a way that, if the total input overcomes some threshold, an output signal is generated. This output signal is transmitted via an axon providing output to other neurons. Many of axonal branches are quite short and have an influence only on the neuronal neighborhood, but axon can also have length of several centimeters and reach neurons in other brain areas. The connection between two cells, transmitting signal from one cell to the other, is called *synapse*. Neuron sending the signal is usually denoted as a *presynaptic* cell, whereas the neuron obtaining the signal is identified as a *postsynaptic* neuron. A typical cell receives more than 10000 inputs from other neurons [26, 40].

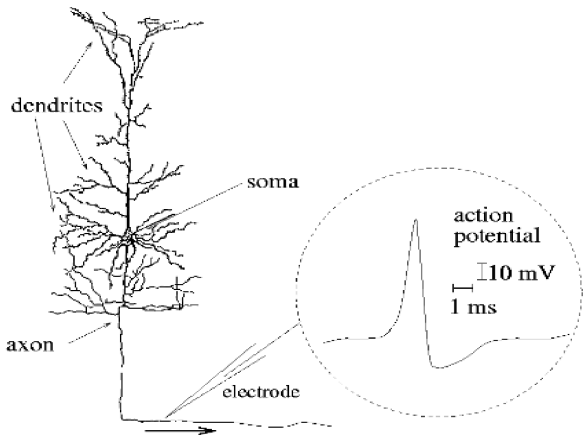

Figure 1.2: Schematic model of the neuron. In the inset a the typical action potential is shown. Source: [26].

The inputs imply electrical transmembrane currents changing the membrane poten-

tial of the neuron. Thus, synaptic currents produce post-synaptic potentials (PSP). Small input currents generate small PSPs, larger currents produce significant PSPs. Post-synaptic currents can be amplified by the voltage-sensitive ion channels in the cell membrane and lead to the generation of *action potentials* or *spikes*. Spike is a sharp and fast change of the membrane potential, which propagates to other neurons. Action potentials have usually an amplitude of $\sim$ 100 mV and duration of $1-2$ ms. Spikes are the main means of communication between neurons. The main patterns of activity of a single neuron are silence, tonic spiking and bursting.

The *silent* neuron in the absence of external input stays in the *resting* state, i.e., its membrane potential does not change and equals ~ -65 mV. If the incoming current is not large enough, neuron responses by a small post-synaptic potential, whereas its reaction on the quite strong input is the action potential followed by the so-called *refractory period* of the cell. During this time the neuronal membrane is hyperpolarized, i.e., its potential is lower than the resting potential level, and the neuron is not able to produce a new spike even after a strong input. If we consider such a neuron as a dynamical system, this state corresponds to a stable fixed point.

The *tonically spiking* neuron permanently produces the spike train, i.e., a sequence of stereotypical events, which occur in regular or irregular time intervals. The action potentials in a spike train are usually clearly separated by the refractory periods. The main characteristic of such a neuron is usually the frequency spectrum of its spiking. From the point of view of nonlinear dynamics, repetitively spiking neuron corresponds to a stable limit cycle in the state space.

The *bursting* neuron produces so-called *bursts*, i.e., a series of spikes intermittent by the periods of silence of the fixed or variable length. There is a great amount of the theoretical studies devoted to the modeling of the bursting neurons, see [40, 66, 74]. Such neurons are characterized by the presence of several time scales in their dynamics. The fastest time scale is responsible for the spike emitting, whereas the slowest scale is present in the intermittence of the silent/spiking states.

1.1.2 Classification of mathematical neuronal models

The first comprehensive mathematical description of the dynamical properties of an excitable cell membrane was given in the work [38] where the famous Hodgkin-Huxley model of the squid giant axon was presented. Nowadays such a formalism is the paradigm for the neuronal behavior in many different models [20, 40, 94]. The Hodgkin-Huxley method allows to build models with the different level of detalization of the processes of interest, in order to achieve more complete physiological description or to obtain a simpler model for further analysis.

There are numerous different models for the single neurons, which differ by their complexity and by the neuronal properties demonstrated by the models. The single-neuron models can be subdivided in five groups as conductance-based models, generic bifurcation models, threshold-type models, phase models and rate models. The different classes of models correspond to the different levels of detalization in modeling of their dynamics. All these types have their own fields of applications and also some limitations.

Conductance-based models are described by complicated systems of ordinary or partial differential equations, which take into account the effects of ionic currents going through membrane, gating variables etc. The advantage of using conductance-based models is that all parameters and variables have clear physiological meaning and could be found experimentally. These models usually have the same properties as the original cells. However, these models are mostly too complicated for the analytical study. Also, the numerical simulations of these models are comparably time consuming. Therefore, under certain conditions it is reasonable to use simpler models for simulations of large neuronal networks. The most known example of the models of this type is the Hodgkin-Huxley model [38].

Generic bifurcation models are not intended for precise modeling of activity of the certain cell. The aim of these models is to achieve qualitatively the same behavior as neurons. Generic bifurcation models are usually described by ordinary differential equations or maps. These models are simpler from the point of view of computer simulations and usually allow precise analytical description of their behavior. The well-known examples of this type are FitzHugh-Nagumo model [23] modeling spiking

neuron dynamics and Hindmarsh-Rose model [37] modeling bursting activity.

Threshold models represent neurons as a series of spikes. These models reflect an evolution of membrane potential up to the moment where it reaches a certain threshold. This moment is fixed as a point of spike emission, and membrane potential is reset to some initial value. Such a process gives a so-called *spike train*. The main idea of such models is to discard information about the exact form and amplitude of spike and to consider only *spike timing*, i.e., times between different spikes. These models are comprehensively described in works [26, 40].

Phase models give the phase from of neuronal processes. It is well known that periodic processes allow their phase representation [48, 59, 101] if we discard the amplitude dynamics from the model. These models have a huge advantage of their numerical simplicity allowing to study large neuronal networks. On the other hand, phase models are very similar to the threshold models and, as a consequence, are not able to imitate the complex neuronal dynamics, e.g., bursting activity. The phase models allow to detect different characteristic macroscopic phenomena in the model, e.g., synchronized or clustered states of the system. Therefore, we will consider the phase Kuramoto model as one of the main object of the study in this thesis. Indeed, due to the large number of neurons in populations it is relevant to consider them as phase oscillators. We will describe the methods of representation of the typical neuronal dynamics in terms of phases below.

Rate models do not take into account spike timing information and model only the neuronal spiking rate. These models are studied in works [39, 42, 75].

The detailed description of the phase models and generic bifurcation models will be given in the following chapters of this thesis. The brief describtion of the conductance-based models will be presented below.

Conductance-based models

Electrical activity of neurons is sustained and propagated through cell membrans via ionic currents. There are four main types of ions involved in majority of transmembrane currents: sodium Na^+, potassium K^+, calcium Ca^{2+} and chloride Cl^- [40].

These ions have different concentrations inside and outside the cell giving rise to electrochemical gradients, which are the main driving forces of the neural activity. Thus, the extracellular liquid has high concentration of Na^+, Cl^- and Ca^{2+}, whereas there are high concentrations of K^+ and negatively charged molecules A^- inside the cell. The cell membrane contains large protein molecules, which are the *channels*, providing flow of ions, but not A^-, through neuron membrane.

The total current via membrane is formed by the above ionic currents. If we do not take into account variabilities of all conductances, the dynamics of the membrane potential V is given by the equation

$$C\dot{V} = -I_{\mathrm{K}} - I_{\mathrm{Na}} - I_{\mathrm{Ca}} - I_{\mathrm{Cl}} - I_{\mathrm{syn}} + I_{\mathrm{ext}}, \tag{1.1}$$

where C is the membrane capacitance. Writing the ionic currents in a more detailed way we obtain

$$\begin{aligned} C\dot{V} = &- g_{\mathrm{K}}\,(V - E_{\mathrm{K}}) - g_{\mathrm{Na}}\,(V - E_{\mathrm{Na}}) - g_{\mathrm{Ca}}\,(V - E_{\mathrm{Ca}}) - \\ &- g_{\mathrm{Cl}}\,(V - E_{\mathrm{Cl}}) - I_{\mathrm{syn}} + I_{\mathrm{ext}} \end{aligned} \tag{1.2}$$

where $g_{\mathrm{K}}, \ldots, g_{\mathrm{Cl}}$ are the constant conductances for the corresponding ions, I_{syn} is a synaptic current from other neurons, which will be described below, and I_{ext} is some external current. The value of V providing zero net current via membrane, which corresponds to zero value of the right-hand side of equation (1.2), is called *resting potential*. The real neurons have variable conductances. This property is reflected in the neuronal models [38, 40] where the *gating variables* governed by differential equations are introduced. For example, the Hodgkin-Huxley model contains three gating variables. Each conductance is given by a product of powers of one or several gating variables.

Because of its high dimensionality, original Hodgkin-Huxley model is complicated for the analytic study as well as for the modeling of networks with large number of elements. That is the reason for attempts of its simplyfication. The famous example of the simplified Hodgkin-Huxley model is the two-dimensional *Morris-Lecar* system [55]

$$\begin{aligned} \dot{V} &= -g_{\mathrm{L}}\,(V - V_{\mathrm{L}}) - g_{\mathrm{K}} w\,(V - V_{\mathrm{K}}) - g_{\mathrm{Ca}} m_\infty(V)\,(V - V_{\mathrm{Ca}}) + I_{\mathrm{ext}}, \\ \dot{w} &= \epsilon\,(w_\infty(V) - w)\cosh\left((V + 0.1)/0.3\right) \end{aligned} \tag{1.3}$$

where $V_{\mathrm{L}} = -0.1$, $g_{\mathrm{L}} = 0.5$, $g_{\mathrm{K}} = 2$, $V_{\mathrm{K}} = -0.7$, $g_{\mathrm{Ca}} = 1$, $V_{\mathrm{Ca}} = 1$, $\epsilon = 0.1$, and the functions $m_\infty(V)$ and $w_\infty(V)$ are given by

$$m_\infty(V) = 0.5\,(1 + \tanh\left((V - 0.01)/0.145\right)),$$
$$w_\infty(V) = 0.5\,(1 + \tanh\left((V + 0.1)/0.15\right)).$$

Detailed analysis of the bifurcations in this system has been carried out in works [55, 66].

Synaptic connection Here we present a brief description of the synaptic mechanism allowing to transmit signal between two neurons, from the presynaptic to the postsynaptic cell. Activation of the presynaptic neuron leads to the release of neurotransmitters in synapse from vesicles into the synaptic cleft, i.e., space between axon and dendrite. The molecules of transmitter diffuse in the cleft and activate receptors on the post-synaptic side leading to the opening of ionic channels. This results in the change of the membrane potential of the dendrite of the post-synaptic neuron. The synapses can be subdivided into two classes, excitatory and inhibitory ones. Activation of the excitatory synapse leads to the depolarization of the post-synaptic cell (increase of the membrane potential), while the activation of inhibitory synapse implies the hyperpolarization of the post-synaptic neuron (decrease of the membrane potential). An example of inhibitory neurotransmitter is GABA, and glutamate is a typical excitatory transmitter.

The mathematical models of the synaptic currents transmitted via a so-called chemical synapses are usually written in the following way:

$$I_{\mathrm{syn}} = g_{\mathrm{syn}} s\,(V - V_{\mathrm{syn}}) \tag{1.4}$$

where g_{syn} is the coupling strength and s is some delayed indicator characterizing the state of the pre-synaptic neuron. V_{syn} is a reversal potential determining the type of the synapse. Thus, for an excitatory synapse V_{syn} is larger than usual values of the membrane potential V, and for inhibitory synapse V_{syn} is smaller than usual values of the membrane potential V. An indicator variable $s \in (0, 1)$ is usually modelled by the following differential equation

$$\dot{s} = \alpha H(V_{\mathrm{pre}})(1 - s) - \beta s$$

where $H(V)$ is a (smoothed) Heaviside function, and α and β characterize the velocity of synapse.

Phase representation of the neuronal dynamics Here we briefly describe two methods of the phase representation of the neuronal dynamics. Introduction of phases allows to study the macroscopic effects in neuronal populations like phase synchronization or clusterization. It also justifies using of the phase models for investigation of the neuronal behavior.

The first technique is based on the Hilbert transform [59, 92]. For a given signal $v(t)$ the complex analytical signal $v(t) + iw(t)$ is constructed. Afterwards the phase can be calculated as an angle in the complex plane $\mathbb{C}$ between the real axis and the vector connecting origin with the point $v(t) + iw(t)$ in this plane.

The second technique defines so-called event-related phases [59]. This method is suitable if dynamics of the original signal to be analyzed is characterized by the prominent events at the time moments $\{t_k : k \geq 1\}$. For the cases of spiking (or bursting) neurons these events can be the spike (or burst) beginnings. This technique is illustrated in Figure 1.3. Between the kth and $(k+1)$th events phase is supposed to grow linearly from $2\pi k$ to $2\pi(k+1)$. The expression for phase is then given by the formula

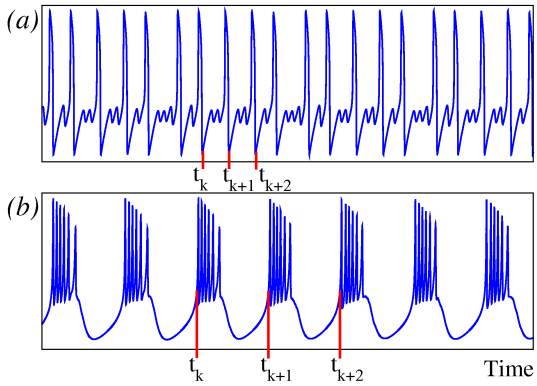

Figure 1.3: Exemplary time courses of the membrane potential of (a) spiking neuron and (b) bursting neuron. Events are depicted by red segments.

$$\theta(t) = 2\pi k + 2\pi \frac{t - t_k}{t_{k+1} - t_k},\ t \in [t_k,\, t_{k+1}]. \tag{1.5}$$

1.2 Structure of the thesis

This thesis consists of three logical parts. The first part presented in Chapter 2 gives a theoretical description of the model of a neuronal system with synaptic plasticity. First of all, the general properties of the usual Kuramoto system of N oscillators are given. Afterwards, a new theoretical model of synaptic plasticity is introduced and its properties are described. Thus, we consider the stability of different dynamical states under the variation of system parameters. The coupling structures for different states revealing the rewiring mechanism of the synaptic plasticity are also considered. We investigate the impact of the variables defining the time scale of the plasticity learning rules and the coupling strength among the oscillators on the system dynamics. Discussion about possible applications of the obtained results to the DBS techniques concludes this chapter. The main results of this chapter have been already published in the work [53].

In the second part given in Chapter 3 two modifications of the Kuramoto system of two oscillators coupled with delay are considered. Each oscillator of these systems simulate the behavior of some large neuronal subpopulation, inside which all neurons are synchronized. This approach allows to consider each subpopulation as a single oscillator. It is supposed that neurons are coupled with time delay, which reflects, e.g., the brain activity under multiple sclerosis [43]. The role of the coupling strength between the oscillators and the time delay is studied. We thus find that increasing time delay or coupling strength leads to the larger number of stable states. The main results of the chapter have been published in the work [52].

The goal of the mentioned two parts of the present thesis is to study different cases and conditions for multistability in systems of coupled oscillators. As an important part of these chapters, sizes and structures of the basins of attraction of the different stable states are considered. This approach allows to estimate the parameters of DBS applied to reach some predefined dynamical state. The property

shared by both physiological phenomena, by the spike-timing dependent plasticity and the coupling delay, is the coexistence of different stable states. This phenomenon is extremely important for the real applications since shift of the system dynamics from the pathological to the healthy state performed by DBS results in a long-lasting therapeutic effect.

The last part of the thesis given in Chapter 4 studies two different models of neuronal networks under impact of coordinated reset stimulation. The first model is based on the Kuramoto system of coupled phase oscillators and the second model represents the population of FitzHugh-Nagumo neurons. The main attention is paid to the study of the effectiveness of the stimulation under parameter variation. The main parameters to be studied are the period of stimulation and stimulation strength since these parameters can be changed in the real application of the method. We also consider distibution width σ of the current spread in the neuronal population with the distance from the stimulation site. This parameter is difficult to control since it depends on the electrochemical properties of the brain tissue. Therefore, we have to know the optimal values of the other stimulation parameters for any values of σ. Consequently, the decay rate σ is one of the important parameters in the present study. For the estimation of the stimulation effectiveness the order parameter technique is used. The second estimation technique is based on the length of the post-stimulus *transient time* when the stimulation is switched off. This method is particularly important since the general idea of the coordinated reset stimulation technique is to decrease the total duration of the stimulus in order to prevent unwanted side effects. Transient time allows to estimate for how long the stimulus can be switched off without resynchronization of the system. Therefore, the longer transient time is, the more effective the stimulation is. We also estimate the extent of desynchronization in the system during the transient time. The Kuiper index technique is used to quantify the state of the system during and after the stimulation.

A modification of CR stimulation protocol corresponding to the real application with the rest periods between the stimulation intervals is considered in subsection 4.1.6. We investigate the dependence of the stimulation effect on the lengths of the active and rest intervals in this stimulation protocol.

For a system of coupled FitzHugh-Nagumo oscillators considered in section 4.2 we use two different techniques for the estimation of CR stimulation effect. The first approach is based on the values of the order parameters. Since we use phase-based order parameters, we also introduce the phases for the FitzHugh-Nagumo oscillators. The second technique utilizes the mean field of the neuronal population to estimate the impact of the stimulation. We use the standard deviation of the system's mean field under CR stimulation.

Conclusions and prospects complete the thesis.

Chapter 2

The Kuramoto model with synaptic plasticity

2.1 The Kuramoto system of coupled oscillators

The Kuramoto model is a large system of weakly coupled phase oscillators, modelling synchronization transition in large ensembles of interacting oscillatory units. It has been shown [48] that, as coupling strength among oscillators increases, the large fraction of the ensemble starts to oscillate with the same frequency, whereas the natural frequencies of its elements are different. This phenomenon is called *synchronization* and numerous natural biological examples of it are described in [27, 59]. Among them we can mention networks of heart pacemakers [58], synchronous activity of the fireflies [18] and circadian rhythms of all living organisms.

An important example of synchronization between electrical activity in the human brain (MEG measurements) and muscles (EMG-signal) was revealed in the work [92]. It was found that EMG-signals with frequency ~ 6 Hz are $2:1$ synchronized with MEG-signals with frequency ~ 12 Hz. This means that for one oscillation of the EMG signal one in average observes precisely two oscillations of the MEG signal.

In terms of the phases of oscillatory signals we can give a general definition of $n:m$ synchronization as follows.

Definition [59]: Two oscillators with phases $\phi(t)$, $\psi(t)$ are $n : m$ synchronized if for some positive integers n and m there exists a constant C such that for all $t > 0 : \ |n\phi(t) - m\psi(t)| < C$.

One of the first mathematical description of synchronization was given in work [100]. He considered an ensemble of coupled phase oscillators described by the following system of differential equations:

$$\dot{\theta}_i = \omega_i + \left(\sum_{j=1}^{N} F\left(\theta_j\right) \right) Z\left(\theta_i\right), \quad i = \overline{1, N} \tag{2.1}$$

where N is the number of oscillators in the ensemble, θ_i are the oscillator phases, and ω_i are the natural frequencies. Each oscillator performs a phase-dependent influence $F\left(\theta_j\right)$ on all other elements. Response of the ith oscillator depends on its phase and is given by the sensitivity function $Z\left(\theta_i\right)$. It was shown that model (2.1) can reach synchronized state (what means that the whole system behaves with the common frequency as a single oscillator, maybe with presence of some "wild" units, oscillating with other frequencies). The synchronization is achieved if the spread of natural frequencies is comparably small and the system shows desynchronized behavior otherwise.

The Kuramoto model was firstly presented in the book [48] to describe behavior of a large system of nearly identical limit-cycle oscillators with weak coupling. The model has a universal form as a system of phase oscillators:

$$\dot{\theta}_i = \omega_i + \sum_{j=1}^{N} \Gamma_{ij}\left(\theta_j - \theta_i\right), \quad i = \overline{1, N}, \tag{2.2}$$

where Γ_{ij} denotes the interaction functions, which can be calculated as an integral from original limit-cycle model. Model (2.2) represents huge simplification of the original system and, nevertheless, it is still quite complicated because of the possibility to have arbitrarily many Fourier harmonics and unspecified connection topology. Further definition of the Γ_{ij} function is given by the following expression [48]:

$$\Gamma_{ij}\left(\theta_j - \theta_i\right) = \frac{K}{N} \sin\left(\theta_j - \theta_i\right), \quad K \geq 0,$$

where K is the coupling strength and $1/N$ factor provides a mean-field meaning of the system coupling among oscillators and guarantees that the system will be well behaving as $N \to \infty$.

It is supposed that the natural frequencies ω_i are distributed according to some probability density function $g(\omega)$, which is unimodal and symmetric, i.e., exists some Ω such that for all ω : $g(\Omega+\omega) = g(\Omega-\omega)$. According to the rotational symmetry of the model, it is possible to redefine the variables $\theta_i \to \theta_i + \Omega t$, $i = \overline{1, N}$. This variable ansatz allows us to go into a coordinated frame rotating with frequency Ω. We can therefore claim that, without loss of generality, the mean value of $g(\omega)$, in other words, the mean frequency of the ensemble, equals zero.

Order parameter

One of the most fruitful approaches to study the synchronization phenomenon in the Kuramoto system is the method of *the order parameter*. Formally, the mth complex order parameter is given by the following expression [29, 48]:

$$R_m e^{i\psi_m} = \frac{1}{N}\sum_{j=1}^{N} e^{im\theta_j}. \tag{2.3}$$

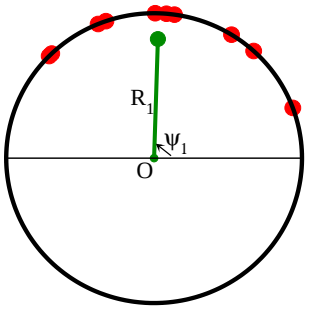

Figure 2.1: Schematic illustration of the order parameter in the complex plane (x, y). Red circles depict $N = 10$ oscillator phases θ_j where the coordinates $x_j = \cos\theta_j$, $y_j = \sin\theta_j$, the green segment connects the complex order parameter (2.3) for $m = 1$ with origin where the length of the segment is its absolute value R_1.

The order parameter is a macroscopic quantity used to estimate the collective rhythm of the whole population. An example of the distribution of the phases and the corresponding order parameter for $m = 1$ are shown in Figure 2.1. R_1 quantifies coherence of the phases, whereas $\psi_1(t)$ gives the mean phase. Fully coherent state

where all phases are equal to each other corresponds to $R_1 = 1$. Desynchronized state where the phases are uniformly distributed on the unit circle (center is situated in origin and radius equals one), is characterized by the order parameter values close to zero. The order parameters of higher degree ($m > 1$ in Eq. (2.3)) are used to detect the clustered state in the system where the oscillator phases split into m groups called clusters such that the phases are coherent within each cluster, but not among the clusters. For example, a perfect m-cluster state is characterized by $R_1 = R_2 = \ldots = R_{m-1} = 0$, and $R_m = 1$, here the oscillator phases split into m equal-size clusters, which are symmetrically distributed on the unit circle. In what follows we will call the absolute value R_m of the complex order parameter (2.3) also as the (real) order parameter of the mth degree.

With the use of the first complex order parameter ($m = 1$ in Eq. (2.3)) the original Kuramoto system

$$\dot{\theta}_i = \omega_i + \frac{K}{N} \sum_{j=1}^{N} \sin\left(\theta_j - \theta_i\right), \tag{2.4}$$

can be rewritten in a compact form. For this, we divide Eq. (2.3) (for $m = 1$) by $\mathrm{e}^{i\theta_i}$, which gives

$$R_1 \mathrm{e}^{i(\psi_1 - \theta_i)} = \frac{1}{N} \sum_{j=1}^{N} \mathrm{e}^{i(\theta_j - \theta_i)}.$$

Taking the imaginary part of this equality we obtain

$$R_1 \sin\left(\psi_1 - \theta_i\right) = \frac{1}{N} \sum_{j=1}^{N} \sin\left(\theta_j - \theta_i\right),$$

and the Kuramoto system (2.4) can be now written in the following form:

$$\dot{\theta}_i = \omega_i + K R_1 \sin\left(\psi_1 - \theta_i\right), \; i = \overline{1,\, N}. \tag{2.5}$$

The mean-field character of the Kuramoto system follows from the latter equation. Indeed, as it is shown by Eq. (2.5), each oscillator is "uncoupled" from the others, but there is a clear coupling between every oscillator and the mean field $Z_1 = R_1 \mathrm{e}^{i\psi_1}$ of the system, characterized by R_1 and ψ_1.

There are two typical forms of dynamics of the Kuramoto system:

1. If the coupling strength is small, the oscillators rotate with different frequencies and, thus, are desynchronized where their phases are uniformly distributed on the unit circle. Then the magnitude of the order parameter R_1 is small being of order $O(N^{-1/2})$.

2. If the coupling strength in the ensemble (2.4) becomes larger than a certain threshold value $K = K_{\text{th}}$, a large group of the oscillators spontaneously starts to oscillate with the same frequency forming a *synchronized cluster*. This state is characterized by large positive values of $R_1 \in (0, 1]$, which depend on the coupling strength.

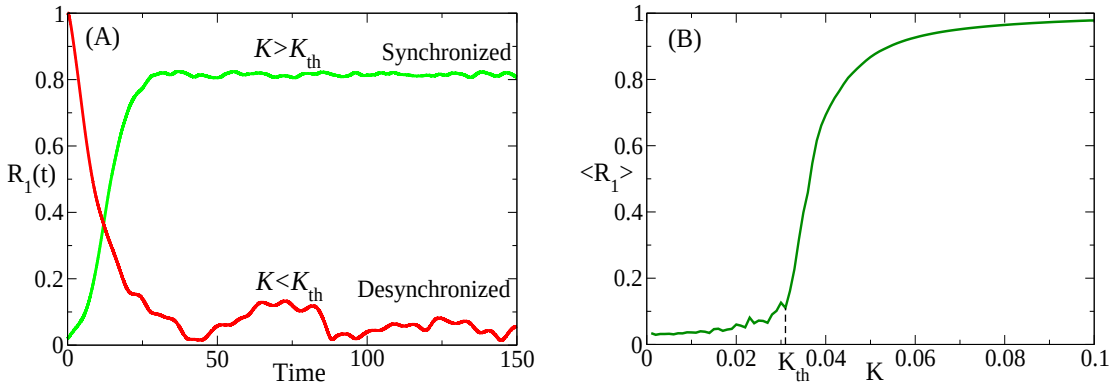

Figure 2.2: Properties of the first order parameter: (A) Time course of R_1 in synchronized (green curve) state and in desynchronized (red curve) states. (B) Values of R_1 averaged over time versus coupling strength. K_{th} denotes the coupling threshold value of the onset of synchronization in the Kuramoto model (2.4).

The exemplary behavior of the first order parameter in different system states is shown in Figure 2.2. As we can see, the bifurcation transition over the value K_{th} in the picture (B) is not very prominent due to the finite dimension of the system.

In the case of the infinite number of oscillators in the system (2.4) (thermodynamic limit) the value of K_{th} can be found explicitly by the formula [48]:

$$K_{\text{th}} = \frac{2}{\pi g(0)}, \tag{2.6}$$

where $g(\omega)$ is the density of distribution of the natural frequencies ω_i in the system, $g(\omega)$ is unimodal (has only one maximum) and the point of this maximum is 0 [48,77].

2.2 Spike timing-dependent plasticity and its model

Spike timing dependent-plasticity (STDP) is a fundamental mechanism for memory and learning in nervous systems [1, 14, 21, 54]. Synapses transmit signals from presynaptic to postsynaptic neurons. Synaptic strength strongly depends on the timing between the firings of two neurons. It was shown in the above papers that if the presynaptic spike advances the postsynaptic one, the synapse is potentiated (its synaptic weight increases), otherwise the synapse is depressed (synaptic weight decreases). The typical dependence of the changes of synaptic weight is shown in Figure 2.3 where potentiation corresponds to the upper part of the diagram (relative change > 1), depression – to the lower part (relative change < 1). Data points show the results of experimental measurements, whereas solid curves fit these results by the exponential functions. Such type of plasticity is often called asymmetric, because of non-symmetry of left and right parts of the diagram in Figure 2.3. Different types of plasticity for different types of neurons are shown in the work [1]. There are several studies devoted to the theoretical models of the synaptic plasticity [41, 73]. Thus, in the work [41] an oscillatory system with combined excitatory and inhibitory coupling was considered. It was supposed that excitatory interactions are plastic, i.e., the corresponding coupling intensities were varying. It was shown using both analytical and numerical methods that in the case of a balance between synaptic potentiation and depression a network of heterogeneous oscillators converges to a globally synchronous state under a wide range of the model parameters. Some neurons also demonstrate symmetric plasticity where relative synaptic change does not depend on the sign of neuronal timing. Several studies of neuronal networks with so called "mexican hut"-type plasticity (symmetric one) have been performed in works [35, 36, 89]. In the present work our attention will be concentrated on the plasticity of the asymmetric type. We show that the crucial role in the system be-

havior is played by the fact, that decay coefficients in the exponential functions of the plasticity rule are different.

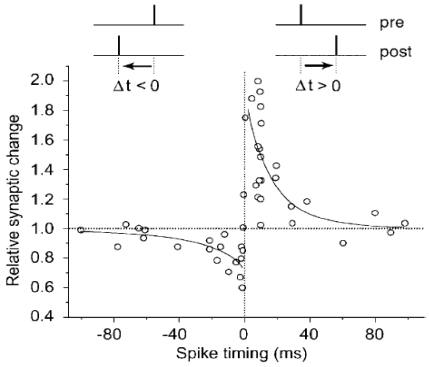

Figure 2.3: Experimental observations of STDP in hippocampal neurons: Change of synaptic weight versus synaptic timing. Source: [13].

The main attention is focused on the macroscopic effects of STDP, namely, on the questions of synchronized (desynchronized) modes in the neuronal activity, their coexistence, and connectivity patterns in the system. To build the model of neuronal network with synaptic plasticity, we incorporate variable synaptic weights (coupling strengths) into the Kuramoto model of phase oscillators. The system of differential equations can be written now in the following form:

$$\dot{\theta}_i = \omega_i + \frac{1}{N}\sum_{j=1}^{N} K_{ij}\sin\left(\theta_j - \theta_i\right), i = \overline{1,N}, \tag{2.7}$$

where K_{ij} are the time-dependent coupling coefficients. High-dimensional model of this type was deeply studied in the work [91]. The main attention there was paid to the questions of coexistence of synchronized and desynchronized modes of the system as well as of the system response to the coordinated reset (CR) stimulation [84, 85]. In the present work we study a low-dimensional model with synaptic plasticity in greater detail in order to get the better understanding of the multistability mechanism. Further, the considered plasticity rules are different (we use the continuous plasticity rules given by the differential equations, whereas in the above work the discrete changes of coupling strengths are implemented). We show

that spike timing-dependent plasticity generically implies coexistence of the different stable system states, such as synchronized as mentioned above, desynchronized and cluster states.

For the further analysis of the system dynamics we have to introduce the *averaged frequencies* $\overline{\omega}_i$

$$\overline{\omega}_i = \lim_{t\to\infty} \frac{\theta_i(t) - \theta_i(0)}{t},\ i = 1, \ldots, N.$$

These values characterize the averaged speed of phase increasing for the corresponding oscillators. We will use the $\{\overline{\omega}_i\}$ values to detect synchronized clusters in the model (2.7). We utilize this approach since the oscillators in the synchronized cluster have the same averaged frequencies.

In the standard finite-dimensional Kuramoto model without plasticity, i.e., $K_{ij} = K = \text{const}$, there exists a critical value of coupling K_c providing the *fully synchronized* state in the system for $K > K_c$ since the support of the distribution of the natural frequencies $\{\omega_i\}$ is bounded. In the fully synchronized state all oscillators are included into a single synchronized cluster of size N.

Therefore, for $K > K_c$ all averaged frequencies $\overline{\omega}_i$ are equal to the mean natural frequency $\Omega = \frac{1}{N}\sum_{i=1}^{N}\omega_i$. If the coupling strength K decays from K_c to zero, the averaged frequencies of individual oscillators $\overline{\omega}_i$ split from the common mean frequency Ω and the total number of different frequencies $\overline{\omega}_i$ grows with further decreasing of K. At some value $K = K_d$ we have fully desynchronized state where all values of $\overline{\omega}_i$ are different. It is believed that the system (2.4) has a single attractor, but this problem is not solved nowadays [77].

In order to implement the mechanism of plasticity in the Kuramoto model, we assume that synaptic strengths K_{ij} in Eq. (2.7) are changed according to the STDP learning rule in such a way: A presynaptic spike from the jth neuron arrives at the ith neuron at time t_{pre}, and a postsynaptic spike occurs in the ith neuron at time t_{post}. It is supposed that the value of K_{ij} increases (synaptic potentiation) or decreases (synaptic depression) depending on the sign of the timing difference $\Delta t = t_{post} - t_{pre}$. We have synaptic potentiation if the postsynaptic spike follows the presynaptic one: $\Delta t > 0$. Correspondingly, a depression takes place if $\Delta t < 0$. The experimental works [13, 14] show that change of synaptic weight depends exponentially on the

spike timing:

$$\Delta K_{ij} = \varepsilon_p \left(\alpha - K_{ij}\right) \exp\left(-\Delta t/\tau_p\right),\ \varepsilon_p < 1,\ (\Delta t > 0),$$

$$\Delta K_{ij} = -\varepsilon_d K_{ij} \exp\left(\Delta t/\tau_d\right),\ \varepsilon_d < 1,\ (\Delta t < 0)$$

The multiplier $\alpha - K_{ij}$ in the first equality is added to avoid the unphysiological growth of the synaptic weights. In this way all synaptic weights K_{ij} are nonnegative and lie in the interval $[0,\ \alpha]$. As we can also see that for the weak synapse (K_{ij} small) potentiation is strong and depression is mild, whereas the situation is reversed for large values of K_{ij} close to α.

In order to simplify the further analysis we can also write this learning rule in the form of differential equation taking into account slow variation of K_{ij} comparing to the fast phase dynamics:

$$\dot{K}_{ij} = \varepsilon \begin{cases} \left(\alpha - K_{ij}\right) \exp\left\{\left(\theta_i - \theta_j\right)/\tau_p\right\}, & \left(\theta_i - \theta_j\right) \in [-\pi, 0] \\ -K_{ij} \exp\left\{-\left(\theta_i - \theta_j\right)/\tau_d\right\}, & \left(\theta_i - \theta_j\right) \in (0, \pi], \end{cases} \tag{2.8}$$

where ε is a fixed small parameter.

Now we have the Kuramoto model with incorporated plasticity rule, which consists of N ordinary differential equations for the phase variables $\{\theta_i\}$ and $N(N-1)$ equations for coupling variables $\{K_{ij}\}$ (it is supposed that we do not have self-coupling items $\{K_{ii}\}$, therefore the number of coupling variables is $N^2 - N = N(N-1)$). Thus, the total dimensionality of the model (2.7) and (2.8) equals N^2. This system is defined on the direct (Cartesian) product of the N-dimensional torus $\mathbb{T}^N$ of the phase variables θ_i and the $N(N-1)$-dimensional Euclidean space $\mathbb{R}^{N(N-1)}$ of the coupling coefficients K_{ij}. Generally, time coefficients for potentiation τ_p and depression τ_d in Eq. (2.8) are unequal, giving us the necessary asymmetry of the plasticity rule. The experimental estimations show the following values of these time constants: $\tau_p \approx 16.8$ ms and $\tau_d \approx 33.7$ ms. In our numerical simulations values $\tau_p = 0.15$ and $\tau_d = 0.3$ will be used.

The plasticity model (2.7) and (2.8) reflects several important properties of the real neurons. Indeed, as we can see from equations (2.8), strong synapses undergo relatively smaller potentiation than weak ones (because of multiplier $(\alpha - K_{ij})$) and,

on the other hand, relative depression does not depend on the synaptic strength as follows from the second equation in (2.8). Another important property, prevalence of depression compared to potentiation, is determined by the unequal exponents τ_d and τ_p where $\tau_d > \tau_p$. It will be shown below that this asymmetry of STDP learning rule is crucial for the phenomenon of multistability. This phenomenon can be declared as coexistence of synchronized, desynchronized and different clustered states in wide enough domains in parameters space. As will be further shown, this property is robust with respect to the variation of parameter ε (for small enough values). The main dynamical properties of the studied dynamical regimes remain the same in the considered system if the discontinuous learning functions in equation (2.8) are approximated by smooth ones.

2.3 The role of STDP asymmetry

In this section we investigate how sensitive is our model (2.7) and (2.8) to the variation of parameter difference $\tau_d - \tau_p$. Two different cases can be distinguished: symmetric (with $\tau_d = \tau_s$) and asymmetric case ($\tau_d > \tau_p$). The process of desynchronization (under decreasing of maximal coupling strength α) can develop according to two dynamically different bifurcation scenaria: whether in a supercritical (soft) way for the symmetric case $\tau_d = \tau_d$ or in a subcritical (hard) way provided $\tau_d > \tau_p$. The typical pictures for the desynchronization transition for $N = 2$ and $N = 3$ oscillators are shown in Figure 2.4.

If we have equal values of $\tau_p = \tau_d$, then there is no multistability, and desynchronization happens in a soft way at the value $\alpha = \alpha_c$ where the fully synchronized state disappears in a saddle-node bifurcation. Therefore, for $\alpha < \alpha_c$ a desynchronized state characterized by different values $\overline{\omega}_1 \neq \overline{\omega}_2$ is stable. Otherwise, if the STDP rule is asymmetric, i.e., $\tau_d > \tau_p$, there exists the multistability interval of the parameter values α.Thus, for the system of $N = 2$ oscillators the fully synchronized state and a desynchronized state coexist on the parameter interval $\alpha \in [\alpha_c, \alpha_s]$, see Figure 2.4(c). For the system of $N = 3$ oscillators the fully synchronized state, the fully desynchronized state and the two-cluster state with the averaged frequencies

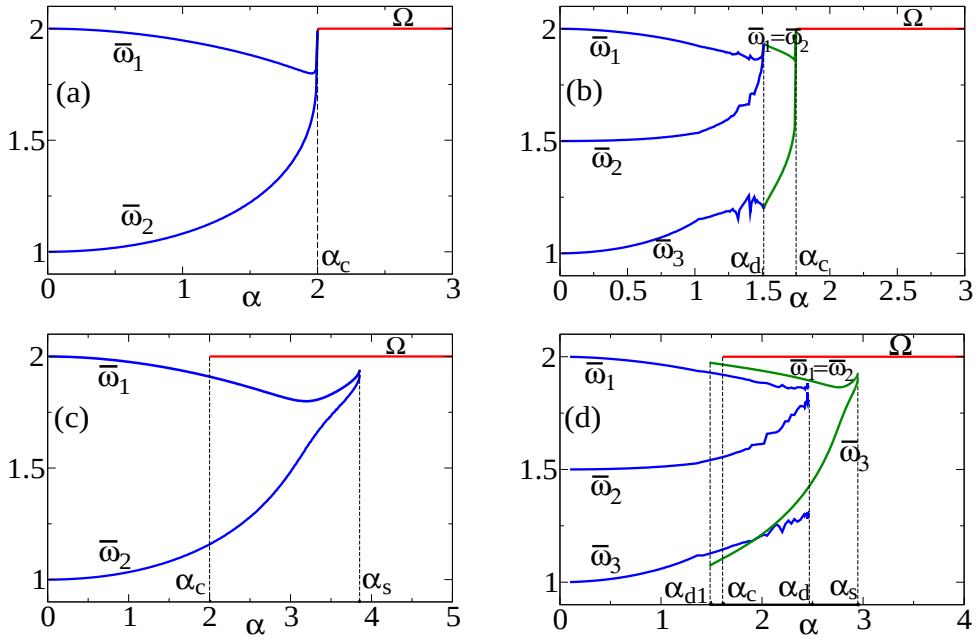

Figure 2.4: Averaged frequencies of the oscillators for the system of $N = 2$ ((a),(c)) and $N = 3$ ((b),(d)). Red line depicts fully synchronized state with common frequency $\Omega = \omega_1$; blue curve: fully desynchronized states; green curve: two-cluster states with $\overline{\omega}_1 = \overline{\omega}_2 \neq \overline{\omega}_3$. Value of ε: 0.5; (a),(b) – no multistability for symmetric STDP rule ($\tau_p = \tau_d = 0.3$); (c), (d) – multistability is present for asymmetric STDP rule ($\tau_p = 0.15$, $\tau_d = 0.3$).

$\overline{\omega}_1 = \overline{\omega}_2 \neq \overline{\omega}_3$ are stable for $\alpha \in [\alpha_c, \alpha_d]$, see Figure 2.4(d).

Summarizing, the multistability interval of α arises due to the asymmetry of the STDP rule, i.e., if τ_p becomes smaller than τ_d. There is also additional restriction providing existence of multistability interval, namely, parameter ε should not be too large ($\varepsilon < \varepsilon_M \approx 60.95$). The next Figure 2.5 reveals the dependence of the multistability interval on value of τ_p. Value of τ_d is fixed and equals 0.3. As it is mentioned before, if τ_p becomes equal to $\tau_d = 0.3$, multistability interval disappears. Reasonable to make a suggestion, that length of the multistability interval (α_c, α_s) grows to infinity, while τ_p converges to zero.

Now we will consider the multistability mechanism in the simplest case of $N = 2$

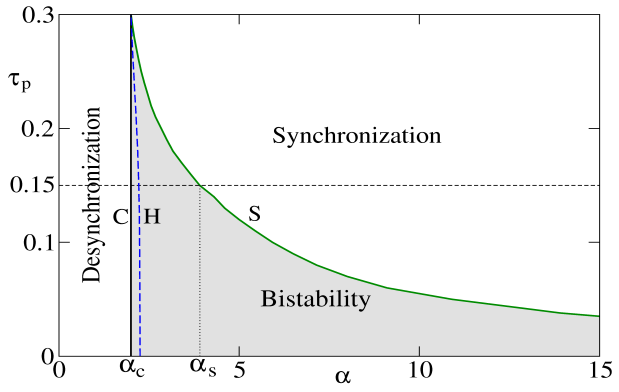

Figure 2.5: Different dynamical modes in the plane $(\alpha,\, \tau_p)$ for the system of $N = 2$ oscillators. Parameters are $\tau_d = 0.3$, $\varepsilon = 0.5$, $\omega_1 = 2$ and $\omega_2 = 1$.

oscillators, and the whole system consists of four equations (2.7) and (2.8). The state space of the system of differential equations is $\mathbb{T}^2 \times \mathbb{R}^2$ (two phase variables and two coupling strengths). But the actual system dynamics is three-dimensional, because it is enough to consider phase difference $\varphi = \theta_1 - \theta_2$ instead of two phase variables θ_1 and θ_2. Then the model (2.7) and (2.8) can be written in the following reduced form:

$$\begin{aligned} \dot{\varphi} &= \Delta_1 - \frac{K_{12} + K_{21}}{2} \sin\varphi, \\ \dot{K}_{12} &= \varepsilon \begin{cases} (\alpha - K_{12}) \exp\{\varphi/\tau_p\}, & \varphi \in [-\pi, 0] \\ -K_{12} \exp\{-\varphi/\tau_d\}, & \varphi \in (0, \pi], \end{cases} \\ \dot{K}_{21} &= \varepsilon \begin{cases} -K_{21} \exp\{\varphi/\tau_d\}, & \varphi \in [-\pi, 0) \\ (\alpha - K_{21}) \exp\{-\varphi/\tau_p\}, & \varphi \in [0, \pi], \end{cases} \end{aligned} \tag{2.9}$$

where $\Delta_1 = \omega_1 - \omega_2$ is the difference of natural frequencies. The fully synchronized state can be given in these new variables $(\varphi, K_{12}, K_{21})$ by a stable fixed point O of the system (2.9) with coordinates: $(\arcsin(2\Delta_1/\alpha),\, 0,\, \alpha)$, whereas the desynchronized mode is represented by a stable periodic orbit P_{st}.

As parameter α in system (2.7), (2.8) decreases, the desynchronization transition takes place at $\alpha_c = 2\Delta_1$ (see Figures 2.6 and 2.7) where the stable node O and a saddle $Q = (\pi - \arcsin(2\Delta_1/\alpha),\, 0,\, \alpha)$ merge and disappear in a saddle-node bifurcation at the point $O_{SN} = (\pi/2,\, 0,\, \alpha)$.

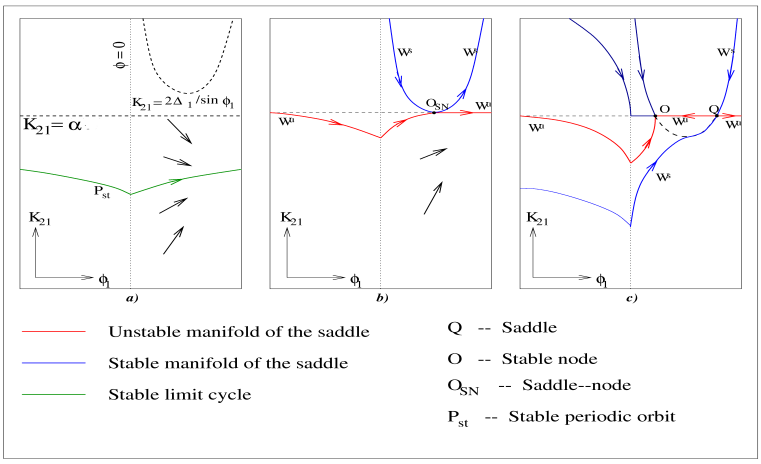

Figure 2.6: Schematic description of the transformations of the vector field in the plane (K_{21}, φ) in system (2.9) as the maximal coupling strength α increases. The symmetric case $\tau_p = \tau_d$ is considered.

The course of the desynchronization transition is qualitatively different in the case of symmetric ($\tau_d = \tau_p$) and asymmetric ($\tau_d > \tau_p$) plasticity. Indeed, in the symmetric case the saddle-node bifurcation at the moment $\alpha = \alpha_c$ is alsoa homoclinic bifurcation for the saddle Q, which gives rise to a stable periodic orbit P_{st}. It exists for all $\alpha < \alpha_c$ and corresponds to the desynchronized state of the original model (2.7), (2.8) where the averaged frequencies $\overline{\omega}_1$, $\overline{\omega}_2$ of the oscillators are different. The evolution of the vector field of the reduced system, when α increases over α_c, in such symmetric case is shown in Figure 2.6.

In the asymmetric case $\tau_d > \tau_p$ the saddle-node bifurcation does not coincide with the homoclinic bifurcation and, correspondingly, does not imply the emergency of the periodic orbit. The stable limit cycle (periodic orbit) is born for such a system at some larger parameter value $\alpha_s > \alpha_c$ as a result of a cycle saddle-node bifurcation for limit cycles where the stable cycle P_{st} appears together with an unstable saddle periodic orbit P_{sd}. The vector field transformations for asymmetric case are shown in Figure 2.7. As we can see, homoclinic bifurcation of the saddle Q occurs at the parameter value α_h, $\alpha_c < \alpha_h < \alpha_s$, Figure 2.7(d). This bifurcation takes place if the saddle unstable manifold (w^u in Figure 2.7(d)) is attracted to the same saddle

point Q. Bifurcation of this type can give rise to the stable or unstable limit cycles depending on the eigenvalues of the saddle [49]. In our system we have appearance of the unstable cycle P_{sd}.

The unstable periodic orbit P_{sd}, which is born as a result of a homoclinic bifurcation, approaches the stable cycle P_{st} with further increasing of α. The value of $\alpha = \alpha_c$ corresponds to the saddle-node bifurcation of cycles P_{sd} and P_{st}, merging together and disappearing in this bifurcation. The curve of the homoclinic bifurcation is shown in Figure 2.5 and is depicted by H. We can also see that, as τ_p decreases to zero, α_s tends to infinity, whereas H-curve is bounded and tends to some value $\alpha_H^0 \approx 2.25$.

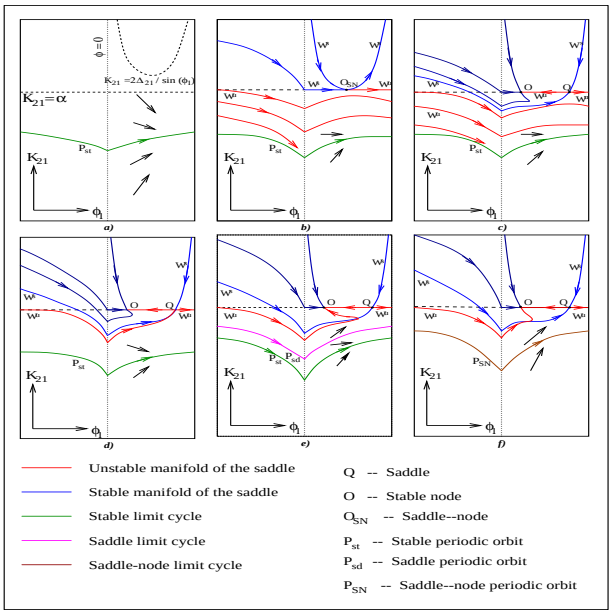

Figure 2.7: Schematic description of the transformations of the vector field in the plane (K_{21}, φ) in system (2.9) as maximal coupling strength α increases. The asymmetric case $\tau_p < \tau_d$.

Now we will describe synchronized and desynchronized dynamical states of the model (2.7) and (2.8). The synchronized state O has common frequency $\Omega = \omega_1$ and is characterized by an interesting property of *unidirectional coupling*: the faster oscillator θ_1 drives the slower one θ_2. Indeed, as we can see from equations (2.9),

phase-locked state (with the constant phase difference $\varphi > 0$) implies $K_{12} = 0$, $K_{21} = \alpha$. The phase difference φ equals $\pi/2$ at the bifurcation moment $\alpha = \alpha_c$ and decreases to zero under further increasing α to infinity. In the case $N = 2$ it is easy to calculate the first order parameter for the synchronized state:

$$R_1 = \left| \frac{1}{2} \sum_{j=1}^{2} e^{i\theta_j} \right| = \frac{1}{2} \sqrt{2 \left(1 + \sqrt{1 - \frac{4\Delta_1^2}{\alpha^2}} \right)}.$$

Therefore, one can see, that $R_1 \to 1$ if maximal coupling strength α tends to infinity.

Now we will consider the desynchronized state of the system. In this state coupling strengths K_{12} and K_{21} lie in the interval $(0, \alpha)$. In the symmetrical case the equality $K_{12} + K_{21} = \alpha$ holds. Indeed, taking the sum of the differential equations for the coupling strengths in Eq. (2.9), we obtain

$$\frac{\mathrm{d}}{\mathrm{d}t} \left(K_{12} + K_{21} \right) = \alpha - \left(K_{12} + K_{21} \right).$$

This differential equation implies that the unique stable fixed point for the sum of the coupling strengths $(K_{12} + K_{21})$ is α. On the other hand, in the asymmetrical case ($\tau_d > \tau_p$) we have inequalities $0 < K_{12} + K_{21} < \alpha$. The exemplary dynamics of these coefficients for the desynchronized state is shown in Figure 2.8.

If we consider the case of $N = 3$ oscillators, then the original system (2.7) and (2.8) has $N^2 = 9$-dimensional state space, and the actual dynamics is eight-dimensional (it is possible to consider phase differences) and acting on $\mathbb{T}^2 \times \mathbb{R}^6$. The general course of desynchronization is similar to the previous system of $N = 2$ oscillators, as one can see from Figure 2.4(b,d). However the bifurcation structure is much more complicated. For the system of $N = 3$ oscillators we also have the stable fully synchronized state with the same averaged frequencies $\overline{\omega}_i$, equal to the natural frequency of the fastest oscillator $\Omega = \omega_1$. This state disappears with decreasing α via a saddle-node bifurcation (the explicit expression will be given for critical value $\alpha = \alpha_c$ in the next section). Two nonsynchronized states (fully desynchronized and 2-cluster one characterized by the averaged frequencies $\overline{\omega}_1 = \overline{\omega}_2 \neq \overline{\omega}_3$ forming two different synchronized clusters of size two and one) cease to exist with increasing α via cycle saddle-node bifurcations at α_d and α_s values, respectively.

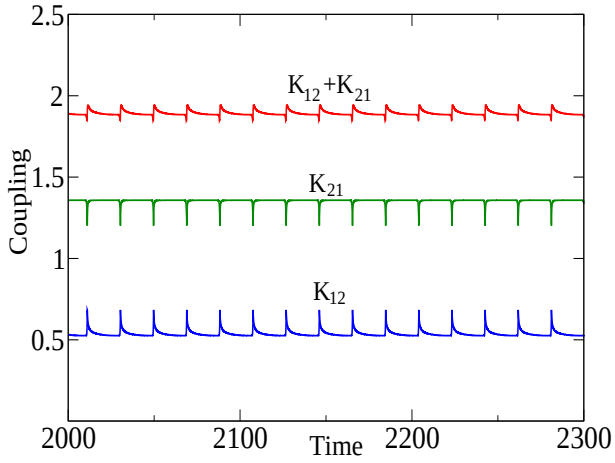

Figure 2.8: An examples of the time courses of $K_{12}(t)$, $K_{21}(t)$ and their sum in the desynchronized state. System parameters are $\alpha = 3$, $\tau_p = 0.15$, $\tau_d = 0.3$, $\varepsilon = 0.5$, $\omega_1 = 2$ and $\omega_2 = 1$.

2.4 Properties of the synchronized state

In this section we describe the features of the synchronized phase-locked state of the system (2.7) and (2.8). This state is supported by the fixed point O mentioned in the previous section. O corresponds to the stable equilibrium of the reduced system, which can be obtained if we consider the phase differences $\varphi_i = \theta_1 - \theta_{i+1}$:

$$\dot{\varphi}_i = \Delta_i - \frac{1}{N}\left[(K_{1,i+1} + K_{i+1,1})\sin\varphi_i + \sum_{j=1,j\neq i}^{N-1}(K_{1,j+1}\sin\varphi_j + K_{i+1,j+1}\sin(\varphi_i - \varphi_j))\right], \tag{2.10}$$

where $\Delta_i = \omega_1 - \omega_{i+1}$, $i = \overline{1, N-1}$. At the fixed point O each coupling strength K_{ij} is equal to either 0 or α, which follows from equations (2.8) with an additional condition of the phase-locking (phase differences are fixed). Without loss of generality, we can suppose that all natural frequencies are ordered in the descending order, i.e., $\omega_1 > \omega_2 > \ldots > \omega_N$. Indeed, it is always possible to renumber the oscillators to achieve such order (for the simplicity we consider only systems with different natural frequencies). As follows, we obtain $K_{ij} = \alpha$ for $i > j$, and $K_{ij} = 0$ otherwise. Substitution of these values of K_{ij} into Eqs.(2.10) allows us to find equilibrium O

from the system

$$\Delta_i - \frac{\alpha}{N}\left[\sin\varphi_i + \sum_{j=1}^{i-1}\sin\left(\varphi_i - \varphi_j\right)\right] = 0,\ i = \overline{1, N-1}. \tag{2.11}$$

We can now solve system (2.11) (or prove that there is no solution, which depends on the system parameters) by sequentially finding the values of φ_i, $i = \overline{1, N-1}$:

$$\begin{aligned} &\Delta_1 - \frac{\alpha}{N}\sin\varphi_1 = 0 && \Rightarrow \varphi_1 = \arcsin\left(N\Delta_1/\alpha\right) \\ &\Delta_2 - \frac{\alpha}{N}\sin\varphi_2 - \frac{\alpha}{N}\sin\left(\varphi_2 - \varphi_1\right) = 0 && \Rightarrow \varphi_2 = \ldots \end{aligned} \tag{2.12}$$

If this system is solvable, then it has two solutions: stable and unstable one. Also, we can find that the common frequency of the synchronized state Ω equals ω_1, which is the maximal natural frequency. Indeed, because equation (2.7) can be written for the first oscillator just as $\dot{\theta}_1 = \omega_1$ and all phase-locked oscillators have the same frequencies the entire ensemble oscillates with the common frequency $\Omega = \omega_1$. For system (2.11) the existence of the synchronized phase-locked state depends only on the natural frequencies ω_i and the maximal coupling strength α and does not depend on parameters τ_p, τ_d, ε.

Summarizing at this point we can formulate the following results for the synchronized phase-locked state. There exists some critical parameter value α_c, which is determined by the values of natural frequencies $\omega_1, \ldots, \omega_N$ and does not depend on the constants τ_1, τ_2, $\varepsilon > 0$, such that:

1. For the maximal coupling strength $\alpha \geq \alpha_c$, our plasticity model (2.7) and (2.8) has the stable synchronized state O corresponding to the solution of system (2.11). This state is characterized by the hierarchical unidirectional structure of coupling where the fastest oscillator drives all others.

2. There is no synchronized states for $\alpha < \alpha_c$.

As an exemplary values of α_c we can give:
$N = 2$: $\alpha_c = 2\Delta_1$;
$N = 3$: $\alpha_c = \max\left\{3\Delta_1; \frac{3\Delta_2^2}{2\sqrt{\Delta_2^2 - \Delta_1^2}}\right\}$.

2.5 Multistability in system of $N = 3$ oscillators

In this section we consider different types of multistability in the system (2.7) and (2.8) of $N = 3$ oscillators. One example of the dynamics for such a system has been already shown in Figure 2.4(d). System of $N = 3$ oscillators is characterized by a possibility to have the simplest clustered state (2-cluster state, where 2 of 3 frequencies coincide providing existence of two clusters of size one (single oscillator) and two (two synchronized oscillators), correspondingly). The clustered states in the model (2.7) and (2.8) have the coupling patterns involving the hierarchical structure within each cluster and oscillating couplings between the oscillators from different clusters.

Here we introduce the concept of resonant tongues since it will be used further in this section.

Definition: A parameter set for the system (2.7) and (2.8) is said to belong to the resonant (Arnold) tongue $D_{p/q}$ if there exists a stable solution with the averaged frequencies $\overline{\omega}_1$, $\overline{\omega}_2$ and $\overline{\omega}_3$ satisfying

$$p/q = (\overline{\omega}_2 - \overline{\omega}_3) \,/\, (\overline{\omega}_1 - \overline{\omega}_3)\,. \tag{2.13}$$

The particular examples of resonant tongues are 0/1 and 1/1 tongues. Here we present the explanation of their structure in order to give the better understanding of this concept. Considering the 0/1 tongue we obtain the expression for its averaged frequencies $\overline{\omega}_2 = \overline{\omega}_3$. This tongue corresponds to the 2-cluster state where the first cluster consists of the single 1st oscillator and the second cluster contains 2nd and 3rd oscillators with the same averaged frequencies. Similarly, for 1/1 resonant tongue we obtain $\overline{\omega}_2 = \overline{\omega}_1$. Therefore, this tongue also corresponds to the 2-cluster state with the synchronized 1st and 2nd oscillators, the 3rd oscillator forms cluster with one element. Thus, these two mentioned clusters are *partially synchronized* states where two of three oscillators are synchronized. On the other hand, the resonant tongues $D_{p/q}$ satisfying $0 < p/q < 1$ give rise to the fully desynchronized states since such values of p/q provide three different averaged frequencies $\overline{\omega}_i$.

Different possible stable states in the parameter plane (ω_2, α) are shown in Figure 2.9. As we can see, many dynamical states may coexist for the same system pa-

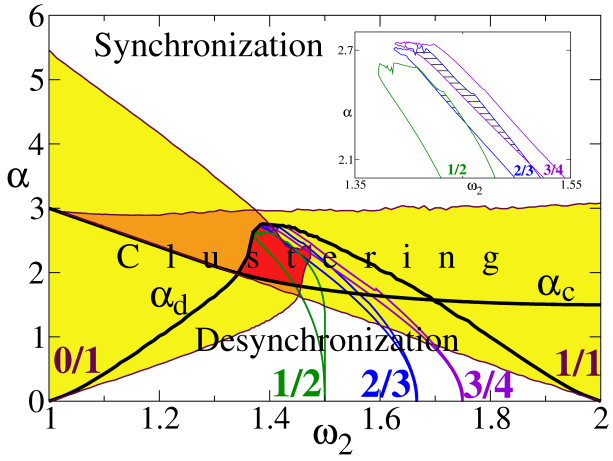

Figure 2.9: Multistability diagram in the plane (ω_2, α), other parameters are fixed: $\omega_1 = 2$, $\omega_3 = 1$, $\tau_p = 0.15$, $\tau_d = 0.3$, $\varepsilon = 0.5$. ω_2 changes on interval $[1, 2]$ between ω_3 and ω_1. Yellow domains: cluster $\overline{\omega}_1 \neq \overline{\omega}_2 = \overline{\omega}_3$ is depicted as tongue 0/1; cluster $\overline{\omega}_1 = \overline{\omega}_2 \neq \overline{\omega}_3$ is depicted as tongue 1/1. The tongues 1/2, 2/3, 3/4 are also shown. Border of the synchronization region: bold curve α_c, border of desynchronization: curve α_d.

rameters. Solid black curves α_c and α_d limit the regions of stability of the fully synchronized and desynchronized state. Yellow regions (partially synchronized) correspond to the different 2-cluster states. Orange domain depicts their overlapping (coexistence). What is especially interesting, the resonant tongues (shown in green, blue and violet) also have some narrow domains of overlapping. This means that there exists some parameter set where the system have *different* stable desynchronized states. The most interesting region from the point of view of multistability (maximal number of different overlapping domains) is depicted in red in Figure 2.9. Generally, there are infinitely many resonant tongues originating from the corresponding points on the line $\alpha = 0$, but in the Figure 2.9 only the most prominent, i.e., with the largest basins of attraction, tongues are shown.

As the next step we build the diagram of the averaged frequencies of oscillators versus parameter α, see Figure 2.10. This figure is analogous to Figure 2.4(d) with the difference that here we consider $\omega_2 = 1.4$, which is the most interesting parameter

value (from the point of view of multistability). As we can see in Figure 2.10, there is coexistence of fully synchronized state O, two-cluster states $D_{0/1}$ and $D_{1/1}$ (here we use the notation of the resonant tongues for the corresponding dynamical states) and desynchronized state (actually, there are several different desynchronized states, e.g., $D_{1/3}$, $D_{1/2}$ and $D_{2/3}$) on interval $\alpha \in [1.9.., 2.7..]$. Blue arrow indicates approximately the region where several desynchronized states are stable. In this figure we can see, how rich the system dynamics can be even in the simplest case ($N = 3$) demonstrating several coexisting dynamical modes.

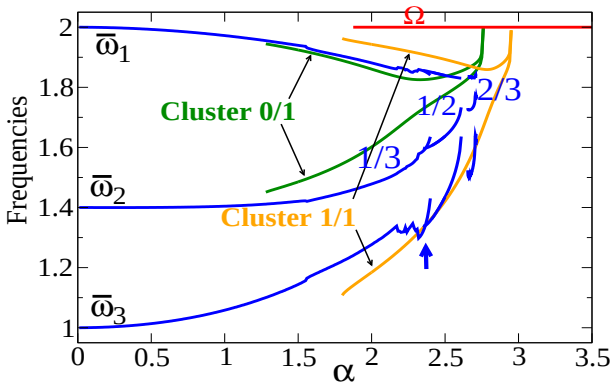

Figure 2.10: Dependence of the averaged frequencies $\overline{\omega}_i$ on parameter α for the system of $N = 3$ coupled oscillators with $\omega_1 = 2$, $\omega_2 = 1.4$, $\omega_3 = 1$. Red line depicts synchronized state, orange and green curves indicate two different 2-cluster states, and blue curves stand for different desynchronized states.

2.6 High-dimensional systems

Behavior of the model (2.7) and (2.8) becomes more complicated with increasing number N of oscillators. In this section we briefly consider stable dynamical states of the system for $N = 5$, $N = 10$ and $N = 20$ oscillators. Unfortunately, it is too difficult to perform such a detailed analysis, as was done for the systems of $N = 2$ and $N = 3$ oscillators. The main attention is devoted in this section to the transition between synchronized and fully desynchronized states under variation of parameter α.

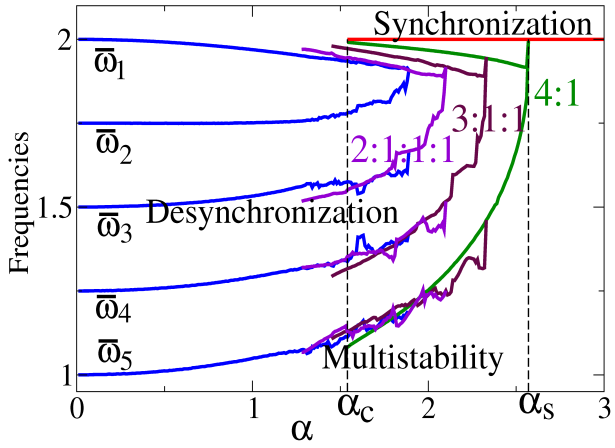

Figure 2.11: Frequency diagram for $N = 5$ oscillators. System parameters are $\omega_1 = 2$, $\omega_2 = 1.75$, $\omega_3 = 1.5$, $\omega_4 = 1.25$ and $\omega_5 = 1$, all other parameters are the same, as in the previous Figures 2.9 and 2.10.

Figure 2.11 reveals that there are different stable clustered states in the system. The numbers in the cluster notations show how much oscillators are locked in each cluster. For example, $3:1:1$ depicts 3-cluster state, for which $\overline{\omega}_1 = \overline{\omega}_2 = \overline{\omega}_3 \neq \overline{\omega}_4 \neq \overline{\omega}_5$. We found that the $4:1$, $3:1:1$, and $2:1:1:1$-clustered states are present for such system. All these clustered states have a similar structure in the sense that clusters with number of involved oscillators greater than 1 consist of elements with maximal natural frequencies, whereas other clusters consist of single oscillators. α-interval of coexistence of the fully synchronized state O with different clustered/desynchronized states is denoted as $[\alpha_c, \alpha_s]$.

In Figure 2.12(a) we plot the frequency diagram for the system of $N = 10$ oscillators. Here, the fully desynchronized state exists for the values $\alpha < 1.52...$ As α increases, this state disappears and the clustered state $2^4 : 1^2$ becomes stable (this notation means that there are four 2-element clusters and two separate oscillators). With further increasing of α the following cluster states appear: $2 : 1^8$, $3^2 : 2 : 1^2$, $3 : 1^7$, $3 : 2^3 : 1$, $4^2 : 1^2$, $5 : 2 : 1^3$, $6 : 2 : 1^2$, $7 : 1^3$, $8 : 1^2$ and $9 : 1$. The fully synchronized state becomes an unique attractor for $\alpha > \alpha_s$. The clustered states $2^3 : 1^4$, $2 : 1^8$, $5 : 2 : 1^3$ and $9 : 1$ are depicted in the diagram 2.12(a) by solid violet, blue, maroon,

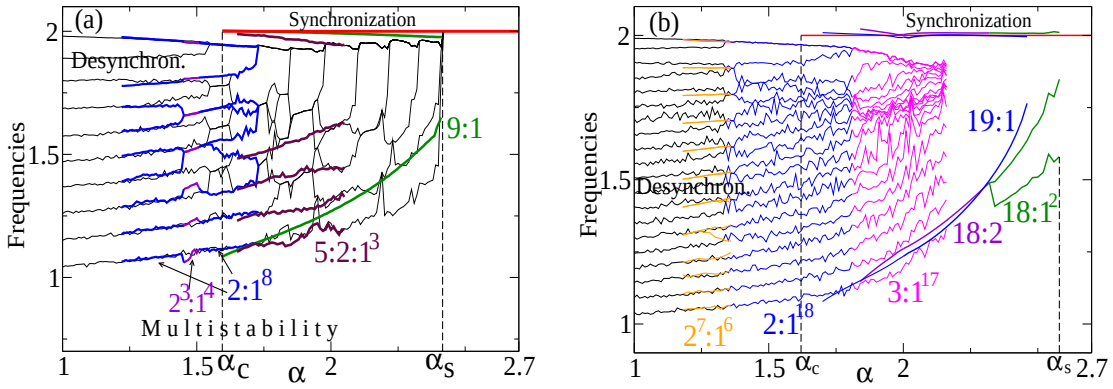

Figure 2.12: Frequency diagram for (a) $N = 10$, (b) $N = 20$ oscillators. System parameters are $\omega_i = 2 - (i-1)/(N-1)$, all other parameters are the same, as in the previous Figures 2.9, 2.10.

and green lines correspondingly.

Figure 2.12(b) reveals the transition between the fully synchronized and desynchronized states for the model of $N = 20$ oscillators. As in the previous figures, one can see different stable clustered states. We here mention that some clustered states, such as $2^7 : 1^6$, $2 : 1^{18}$ and $3 : 1^{17}$ are "close" to the desynchronized state 1^{20}, whereas the other clustered states like $18 : 2$, $19 : 1$ and $18 : 1^2$ are close to full synchronization.

We estimate the size of basins of attraction for different stable states in the systems of $N = 5$ and $N = 10$ oscillators. In order to investigate this problem, parameter $\alpha = 2.0$ will be fixed (this parameter value implies multistability of the synchronized and several clustered states, see Figures 2.11 and 2.12(a)) and a set of random initial conditions will be taken. For the case of $N = 5$ oscillators the number of different initial conditions is 2000, whereas for the system of $N = 10$ oscillators the number of trials is 1000. This procedure allows us to estimate the relative sizes of basins of attraction for different stable modes. For each given state its size is obtained as a fraction of the number of initial points leading to it to the mentioned entire number of trials. The results of calculations are shown in Figure 2.13.

The first order parameter of the corresponding solutions found by the above cal-

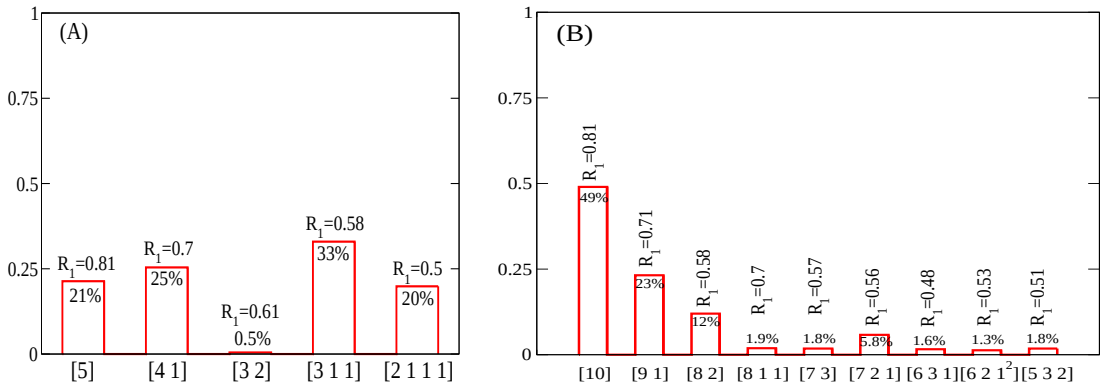

Figure 2.13: Relative sizes of basins of attraction to different stable states shown in square braces for the model (2.7) and (2.8). Number of oscillators: (A) $N = 5$, (B) $N = 10$.

culations is shown in Figure 2.13 on the top of each bar. The sizes of basins of attraction are also shown as percents of the entire volume of initial conditions. Actually, these percentage values correspond to the heights of bars in histogram. Since the total number of different stable states for the system of $N = 10$ oscillators (Figure 2.13(B)) is too large to display them on such histogram, we have shown only the states with the relative volume greater than 1%. As we can see, the sizes of the basins of attraction for different states are large enough, providing the possibility of switching between these modes by appropriate perturbations of the system with STDP (2.7) and (2.8).

2.7 Conclusions

In this section we have investigated multistability in the low-dimensional systems of coupled phase oscillators with spike timing-dependent plasticity. The underlying mechanism has been described in detail for the models of the low dimensionality ($N = 2$ and $N = 3$). We can conclude that STDP implies fascinating coexistence of many different dynamical states ranging from desynchronized up to the fully synchronized one, and this multistability keeps for different sizes of system N. The

plasticity mechanism allows to perform an effective rewiring in the model. An appropriate perturbation of the system dynamics also change the coupling topology in the model since the different stable states are characterized by the different structure of the coupling matrix K_{ij}. It was shown that the couplings within each synchronized cluster form a hierarchical one-directional structure, whereas between the oscillators from different clusters coupling strengths demonstrate oscillations around some moderate values.

Plasticity gives us also the possibility to perform a desynchronizing stimulation in a very mild way (just to switch between different basins of attraction), giving rise the long-lasting effects due to the changes of connectivity structure. The theoretical study investigating such type of stimulation, was already done in the work [91]. Our results should be considered just as a first step performed for a simple model, which can be further extended to more realistic ones, e.g., involving spiking or bursting neuronal models with synaptic coupling.

Chapter 3

Multistability in the delayed Kuramoto model

In this chapter we will investigate systems of phase oscillators coupled with delay. During the last time influence of time delay was an object of interest of many works [19, 44, 64, 104]. Delay naturally arises in systems due to the finite speed of signal propagation between their elements. Large delay can also arise in the neuronal systems, e.g., in the case of multiple sclerosis, see [43]. Appearance of delay can crucially change the dynamics (a system of ordinary differential equations has a finite dimensionality, whereas delayed system is infinite-dimensional). Time delay can induce effects of amplitude death [4,64] or coexistence of different states [71,104]. There are many published works studying different types of delayed feedback. We mention here a few studies, which are the most relevant to the scope of the present work [30, 61, 62, 69]. In the present work we will concentrate on the multistability (coexistence) of different synchronized and desynchronized states in systems of coupled phase oscillators with delay. We formulate the necessary conditions for the multistability phenomenon.

It is well known that phenomenon of multistability can be found for the systems of limit cycle oscillators coupled with delay (system of large number of phase oscillators, which are situated in a two-dimensional plane, has been investigated in the work [56]). A simplified model of delay-coupled phase oscillators has been considered

by [104]:

$$\dot{\theta}_i = \omega_i + \frac{K}{N}\sum_{j=1}^{N}\sin\left(\theta_j(t-\tau) - \theta_i(t)\right),\ i = \overline{1,N}, \tag{3.1}$$

where θ_i are the phase variables and $\tau > 0$ is an interaction time delay. The model (3.1) is a generalization of the standard Kuramoto model (2.4) providing the delayed coupling between oscillators.

We will consider two different systems of two oscillators coupled with delay. The first system has been introduced in the work [71]. It has been found that the model can have several stable synchronized solutions with different frequencies. We will concentrate on the coexistence of different synchronized and desynchronized modes and also on their basins of attraction. This model will be considered in the section 3.1. Our main interest concerns the structure of the basins of attraction of different stable states and the total number of coexisting modes. The aimed findings follow the goal of the application of this theory to the medicine. In order to suppress the undesirable synchronized activity in the brain of PD patients we look for a mild stimulation technique switching the system from one state to another stable one with further stay in this mode without any stimulation.

The second model is system (3.1) for the case of $N = 2$ oscillators. Its distinction from the first model is an additional "self-feedback" term in the right sides of the differential equations. Nevertheless, the behavior of the system changes crucially that will be shown in the following section.

3.1 Kuramoto model with delayed interaction

In this section we consider a system of two coupled phase oscillators where the interaction between the oscillators takes place with some time delay τ. The model can be written in the following form

$$\begin{aligned}\dot{\theta}_1 &= \omega_1 + K\sin\left[\theta_2(t-\tau) - \theta_1(t)\right],\\ \dot{\theta}_2 &= \omega_2 + K\sin\left[\theta_1(t-\tau) - \theta_2(t)\right].\end{aligned} \tag{3.2}$$

Note, the difference between this system and that given by Eq. (3.1) is that in system (3.2) the term of type $\sin(\theta_i(t-\tau) - \theta_i)$ is absent. The system with this term, i.e.,

system (3.1) of two oscillators, will be studied in the next section.

The model (3.2) was originally studied in the work [71]. The main finding was the revealed coexistence of different synchronized states of the type: $\theta_{1,2}(t) = \Omega t \pm \alpha/2$. One can substitute these expressions into the system equations (3.2) and obtain equations for Ω and α, which can be solved numerically. Applying the standard stability analysis for the mentioned synchronized solutions, i.e., using the linearization of system (3.2) around the analyzed solution, one can distinguish stable and unstable synchronized states. We will demonstrate this technique below. The total number of synchronized states grows linearly with increasing of the coupling strength K and of the time delay τ. In the works [102,103] it was also shown that the coexistence of the synchronized and desynchronized (with the non-equal averaged frequencies $\langle\dot{\theta}_1\rangle$ and $\langle\dot{\theta}_2\rangle$ of the oscillators) states in the model (3.2) is also possible, moreover, this phenomenon can be found for the values of delay approximately $\tau > \pi/|\omega_1 - \omega_2|$ and the number of coexisting stable states increases under further increasing of τ.

One of the main mentioned tasks is to understand the structure of the basins of attraction. Unfortunately, it is impossible to describe it precisely because of infinite dimensionality of the delayed system. We use technique originally proposed in the work [71]. The idea is to consider a two-dimensional manifold $M = (\Omega, \alpha)$, which consists of the solutions originating from the initial conditions of special type such that $\theta^0_{1,2} = \Omega t \pm \frac{\alpha}{2}$, $t \in [-\tau, 0]$. Synchronized states lie in this manifold, we can depict them as points in plane (Ω, α). We will also demonstrate the dynamics of unstable solution starting from the border between two basins of attraction of the synchronized states. For these initial conditions the trajectory is attracted by some solution of the saddle type, i.e., by the unstable solution with one positive eigenvalue. The information about the behavior of unstable solutions can be useful for applications since it usually takes more time to reach some stable state if the trajectory starts from the vicinity of an unstable solution. Therefore, the unstable solutions can be objects of interest from the point of view of *transient* after applied stimulation.

3.1.1 Detecting synchronized states

Here we consider the synchronized solutions of system (3.2) and their stability. We are looking for solutions of the form

$$\theta_{1,2}(t) = \Omega t \pm \frac{\alpha}{2}, \tag{3.3}$$

where Ω is the frequency of the synchronized solution and α is the phase difference between the two oscillators. Now we can substitute (3.3) into Eq. (3.2) and obtain equations for Ω and α:

$$\overline{\omega} - \Omega = (-1)^i K \tan(\Omega\tau)\sqrt{\cos^2(\Omega\tau) - \frac{(\Delta\omega)^2}{4K^2}}, i = 1, 2, \tag{3.4}$$

where $\overline{\omega} = (\omega_1+\omega_2)/2$ is the mean natural frequency of the system, and $\Delta\omega = \omega_1-\omega_2$ is the frequency detuning. Each of these two equations gives the values of Ω. Then the corresponding values of α can be found as

$$\alpha = \begin{cases} \pi - \arcsin\left(\frac{\Delta\omega}{2K\cos(\Omega\tau)}\right), & \text{if } \cos(\Omega\tau) > 0,\ i = 1, \\ 2\pi + \arcsin\left(\frac{\Delta\omega}{2K\cos(\Omega\tau)}\right), & \text{if } \cos(\Omega\tau) < 0,\ i = 1, \\ \arcsin\left(\frac{\Delta\omega}{2K\cos(\Omega\tau)}\right), & \text{if } \cos(\Omega\tau) > 0,\ i = 2, \\ \pi - \arcsin\left(\frac{\Delta\omega}{2K\cos(\Omega\tau)}\right), & \text{if } \cos(\Omega\tau) < 0,\ i = 2, \end{cases}, \text{ for } \Delta\omega > 0, \tag{3.5}$$

For the identical oscillators, i.e., $\omega_1 = \omega_2 = \omega$ and $\Delta\omega = 0$, the synchronized solution is determined by the values of $(\Omega,\ \alpha)$, which are the solutions of one of the following four systems of equations

1. $\omega - \Omega = K\sin(\Omega\tau),\ \alpha = 0,$
2. $\omega - \Omega = -K\sin(\Omega\tau),\ \alpha = \pi,$
3. $\sin(\Omega\tau) = 1,\ K\cos(\alpha) = \omega - \Omega,$
4. $\sin(\Omega\tau) = -1,\ K\cos(\alpha) = -\omega + \Omega.$

In what follows we mostly concentrate on the case of nonidentical oscillators. In order to understand the behavior of roots of equations (3.4) we plot the functions of Ω, corresponding to the both sides of these equations: $f_1(\Omega) = \overline{\omega} - \Omega$ and $f_2(\Omega) = K\tan(\Omega\tau)\sqrt{\cos^2(\Omega\tau) - (\Delta\omega)^2/(4K^2)}$ in Figure 3.1.

Synchronized solutions of system (3.2) correspond to the intersections of the straight line given by the $f_1(\Omega)$ in Figure 3.1 with the "butterflies" representing the functions $\pm f_2(\Omega)$. Points with different colors in the butterflies indicate the stability of the

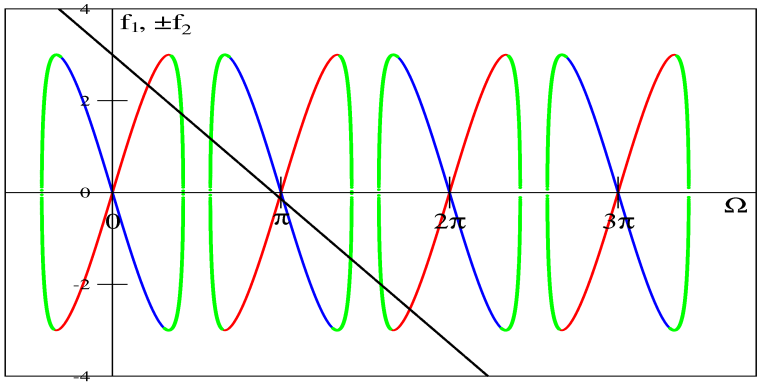

Figure 3.1: Left side of Eqs. (3.4) is shown as function $f_1(\Omega)$ (straight line) and the right sides of Eqs. (3.4) are shown as $\pm f_2(\Omega)$ (butterflies). Red points on the butterflies correspond to the stable solutions, green points correspond to the unstable solutions with one positive eigenvalue and blue points depict the unstable solutions with two positive eigenvalues. Parameters are $\omega_1 = 3.5$, $\omega_2 = 2.5$, $\tau = 1$ and $K = 4$.

corresponding solution. Thus, the red points depict the stable solutions, the green ones correspond to the saddle unstable solutions, i.e., with one positive eigenvalue, and the blue points indicate unstable solutions with two positive eigenvalues. With increasing coupling strength K the butterflies are stretched in the vertical direction such that their size increases linearly with parameter K. Therefore, more and more intersections with the straight line appear. We can conclude that the total number of the synchronized modes increases linearly with increasing K, and approximately one fourth of all solutions is stable. Indeed, each butterfly gives in general case four intersections for large enough K, among which only one corresponds to a stable synchronized state. A typical diagram for the dependence of the frequencies of synchronized solutions Ω and the corresponding phase shifts α on the coupling strength K is shown in Figure 3.2. It is worth mentioning here that there are two types of the stable synchronized solutions. Solutions of the first type have phase shift close to zero, i.e., α tends to 0 for $K \to \infty$. Solutions of another type have α close to π. This question will be important when we compare our model with model (3.7) with self-feedback term in the following section 3.2.

The central points of the butterflies (shown in Figure 3.1) are determined by the

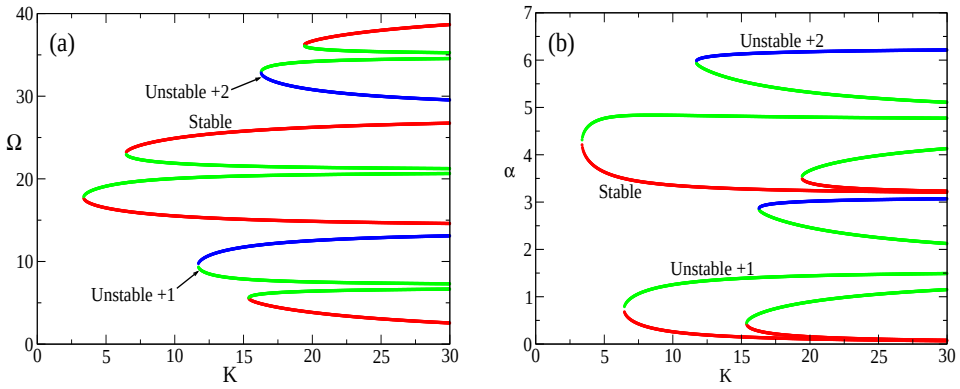

Figure 3.2: (a) Frequencies of the synchronized states $\Omega = \Omega(K)$. Different colors depict different types of stability of the solutions. (b) Corresponding values of the phase difference $\alpha = \alpha(K)$. System parameters are $\omega_1 = 6\pi + 2$, $\omega_2 = 6\pi - 2$ and $\tau = 0.225$.

equality $\tan(\Omega\tau) = 0$ and, correspondingly, $\Omega = \pi n/\tau$, $n \in \mathbb{Z}$. This can be important from the point of view of the symmetry in diagram 3.2(a). If the mean natural frequency $\overline{\omega} = 0.5\,(\omega_1 + \omega_2)$ equals one of these values $\pi n/\tau$, then the straight line in Figure 3.1 passes through the center of some butterfly. This results in the symmetry of Figure 3.2(a), there exists a value of $\Omega = \overline{\omega}$ such that the diagram is symmetric with respect to the line $\Omega = \overline{\omega}$. There is the second symmetrical case where the line $f_1(\Omega)$ passes exactly between two butterflies, this corresponds to the value $\overline{\omega} = \pi(n + 0.5)/\tau$.

In order to investigate the stability of the obtained synchronized modes we will apply the standard technique of linearization of the system in a vicinity of the solution to be analyzed. We consider characteristic quasipolynomial $S(\lambda)$, which can be written in the form of determinant of the matrix $(A + Be^{-\lambda\tau} - \lambda E)$. Here A is the partial derivative of system (3.2) taken over the variables (θ_1, θ_2), and B is the partial derivative taken over the variables $(\theta_1(t-\tau), \theta_2(t-\tau))$. Then the equation for λ has the following form

$$\begin{aligned} S(\lambda) = K^2 \cos(\Omega\tau - \alpha)\cos(\Omega\tau + \alpha) + \lambda K\left(\cos(\Omega\tau - \alpha) + \cos(\Omega\tau + \alpha)\right) + \\ + \lambda^2 - e^{-2\lambda\tau} K^2 \cos(\Omega\tau - \alpha)\cos(\Omega\tau + \alpha) = 0,\ \lambda \in \mathbb{C}. \end{aligned} \tag{3.6}$$

The spectrum of the analyzed solution of the original model (3.2), i.e., synchronized

solution with common frequency Ω and phase shift α, consists of complex roots of equation (3.6). The total number of these roots is infinite, and stability is determined by roots with the maximal real part. Stable modes have spectrum completely located in the left half-plane of the complex plane, i.e., $\mathrm{Re}\lambda < 0$. The only root with zero real part is $\lambda = 0$, corresponding to the shift along the trajectory. In Figure 3.3 we compare spectra of the three cases of stability discussed above for the coupling strength $K = 14$. From Figure 3.2 we can see that for this coupling strength system (3.2) has 6 phase-locked state, and spectra of three of them are depicted in Figure 3.3

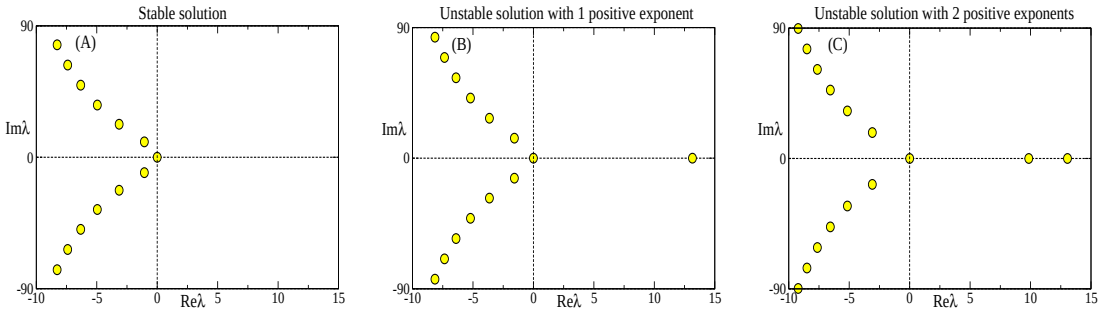

Figure 3.3: Three different types of stability in the model (3.2). (A) Stable solution with $\Omega \approx 25.64$, (B) unstable solution with $\Omega \approx 21.59$ has one positive eigenvalue, (C) unstable solution with $\Omega \approx 11.45$ has two positive eigenvalues. See also Figure 3.2. System parameters are $\omega_1 = 6\pi + 2$, $\omega_2 = 6\pi - 2$, $\tau = 0.225$ and $K = 14$ (the same parameter set, as in Figure 3.2)

3.1.2 Coexistence of different stable modes

As follow from equation (3.4) system (3.2) has phase-locked solutions only for large enough coupling strength K. More precisely K must be larger then $\Delta\omega/2$ for the delay $\tau = 0$. For the case $\tau \geq 0$ dependence $K_{\mathrm{cr}} = K_{\mathrm{cr}}(\tau)$ is shown in Figure 3.4. System (3.2) has only desynchronized solutions for $K < K_{\mathrm{cr}}$ where the oscillators rotate with different frequencies $\langle\dot{\theta}_1\rangle$ and $\langle\dot{\theta}_2\rangle$. Let us consider briefly some basic properties of the curve $K_{\mathrm{cr}}(\tau)$ in Figure 3.4. It has prominent minima and maxima

points, which we now describe explicitly. $K_{\mathrm{cr}}(\tau)$ reaches its minima in the cases where the straight line $f_1(\Omega)$ (from Figure 3.1) passes exactly through the center of some butterfly. It provides the existence of synchronized solutions (intersections of butterflies with this line) for butterflies of any size. The smallest singular butterfly is a point and exists for $K = \Delta\omega/2$. Therefore, $K \geq \Delta\omega/2$. In order to find points τ_n of minima of $K_{\mathrm{cr}}(\tau)$ we have to equate the centers of butterflies ($\pi n/\tau$) with the intersection of line $f_1(\Omega)$ with the axis x ($\overline{\omega}$). In this way points of minima in Figure 3.4 are given by the expression

$$\pi n/\tau_n^{\min} = \overline{\omega} \;\Rightarrow\; \tau_n^{\min} = \frac{\pi}{\overline{\omega}} n,\; n \geq 0.$$

We can also write explicitly the values of K_{cr} in these points. For such τ a synchronized solution exists for any coupling strength K, for which the square root in equation (3.4) is defined, i.e., radicand is non-negative. This is provided by value $K_{\mathrm{cr}}(\tau_n^{\min}) = \frac{\Delta\omega}{2}$.

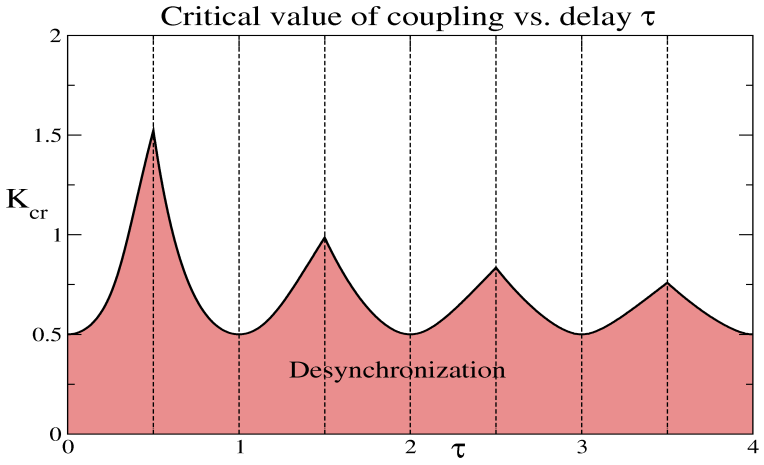

Figure 3.4: Dependence of critical coupling value K_{cr} on time delay τ. Region marked as 'Desynchronization' contains only desynchronized solutions. System parameters are $\overline{\omega} = \pi$ and $\Delta\omega = 1$.

On the other hand, points of maxima of the graph $K_{\mathrm{cr}} = K_{\mathrm{cr}}(\tau)$ in Figure 3.4 correspond to the cases where the line $f_1(\Omega)$ passes exactly between two butterflies. From this condition we obtain the points of maxima given by

$$\tau_n^{\max} = \frac{\pi}{\overline{\omega}} \left(n + \frac{1}{2} \right),\; n \geq 0.$$

For $K > K_{\rm cr}$ there are stable synchronized solutions. It has been shown in works [102,103] that they can coexist with different desynchronized solutions. We illustrate this coexistence in Figure 3.5. The synchronized modes are shown in these diagrams by red points and the desynchronized solutions are shown by black, blue and green points. Desynchronized solutions are shown by pairs of the different frequencies $\langle\dot\theta_1\rangle \neq \langle\dot\theta_2\rangle$, whereas each synchronized state is represented by the single point $\langle\dot\theta_1\rangle = \langle\dot\theta_2\rangle$. As one can see, there is no coexistence for the small value of delay $\tau = 0.2$, whereas the diagram becomes more complicated with increasing τ. For $\tau = 0.6$ we observe the coexistence of one synchronized and one desynchronized state, and for $\tau = 2.0$ we have already coexistence of four desynchronized states and one synchronized (for the value of $K = 2.8$). We can estimate the value of τ providing such coexistence as $\tau \approx \pi/(2\Delta\omega)$.

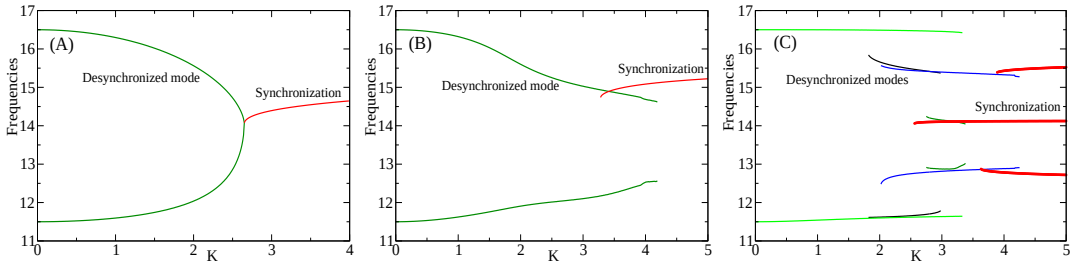

Figure 3.5: Averaged frequencies $\langle\dot\theta_{1,2}\rangle$ versus coupling strength K for different values of τ: (A) $\tau = 0.2$, (B) $\tau = 0.6$ and (C) $\tau = 2.0$. Natural frequencies are $\omega_1 = 16.5$ and $\omega_2 = 11.5$.

The similar diagram is shown in Figure 3.6 for $\tau = 5$ in the case of symmetric frequencies of the synchronized solutions, see p. 47. Indeed, Figure 3.6 is symmetric with respect to the line $\omega = 4.6\pi \approx 14.45$. It is also revealed by diagrams 3.5(c) and 3.6 that the oscillator frequencies form horizontal "shelves" under variation of K. This phenomenon has been found already in work [103]. We can see in Figure 3.6 that all stable modes have quantized frequencies. Indeed, there is some set of numbers that for all states in the system (synchronized as well as desynchronized) oscillator frequencies approximately equal numbers from this set. This mechanism is clear for the synchronized solutions since their frequencies are the roots of equation (3.4) and quantization follows from the structure of "butterflies" (see Figure 3.1).

But in the case of desynchronized solutions it is much more difficult to explain this fascinating phenomenon.

The differences between the numbers in the above mentioned set are approximately equal to $m \cdot \pi/\tau$, $m \in \mathbb{N}$ (due to the quantization). The minimal value is, correspondingly, equal to π/τ. This minimal value tends to zero as τ increases. For some desynchronized solution with averaged oscillator frequencies $\Omega_{1,2}$ both frequencies belong to the interval $[\omega_2, \omega_1]$ and their difference is bounded by 0 and $\Delta\omega = \omega_1 - \omega_2$. Moreover, interval of values of K providing the existence of desynchronized solutions is almost the same for different values of τ.

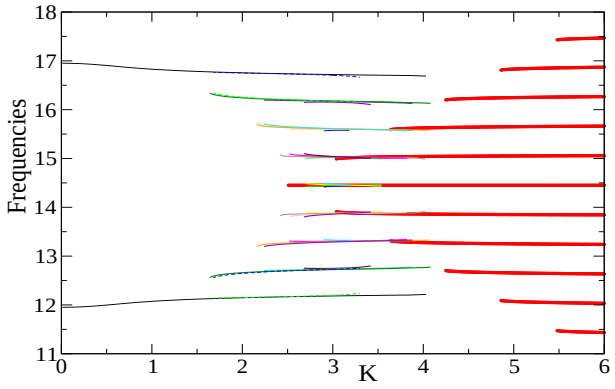

Figure 3.6: Averaged frequencies $\langle\dot{\theta}_{1,2}\rangle$ versus coupling strength K. Red points depict synchronized solutions, and the points of other colors depict desynchronized solutions. System parameters are $\omega_1 = 4.6\pi + 2.5$, $\omega_2 = 4.6\pi - 2.5$ and $\tau = 5$, which correspond to the symmetric case for the frequencies, see page 47 (symmetry with respect to the line $\Omega = 4.6\pi$).

In order to estimate the whole picture of coexisting states and its changes under variation of τ, we will use the following form of representation. The averaged frequencies of all stable solutions will be shown in the plane (Ω_1, Ω_2) as separate points. These diagrams for $\tau = 5$ and $\tau = 10$ are shown in Figure 3.7. To build such pictures system (3.2) has been numerically solved for some selected set of initial conditions and the corresponding values of Ω_1 and Ω_2 have been obtained. As the set of initial conditions the following functions have been taken: $\theta_1(t) = a_1 t + \alpha/2$, $\theta_2(t) = a_2 t - \alpha/2$ where a_1, a_2 have been equally distributed in the segment $[8 \ldots 18]$ with stepsize

0.1, whereas α – from the segment $[0 \dots 6.2]$ with the same stepsize. This method has one sufficient disadvantage where we cannot guarantee that all stable solutions have been found. On the other hand, we can conclude that solutions, which have been found by this method and are shown in Figure 3.7 have the largest basins of attraction among all stable solutions in the space of initial conditions considered above. In Figure 3.7(A) ($\tau = 5$) the minimal difference between the neighboring points is approximately 0.55 and there are totally 16 desynchronized solutions coexisting with an unique synchronized solution marked by **S**. In Figure 3.7 (B) ($\tau = 10$) the picture is more complicated where the stepsize between two points decreases by factor 2 resulting in more dense structure. For this value of delay there are already 43 desynchronized solutions and 3 synchronized solutions.

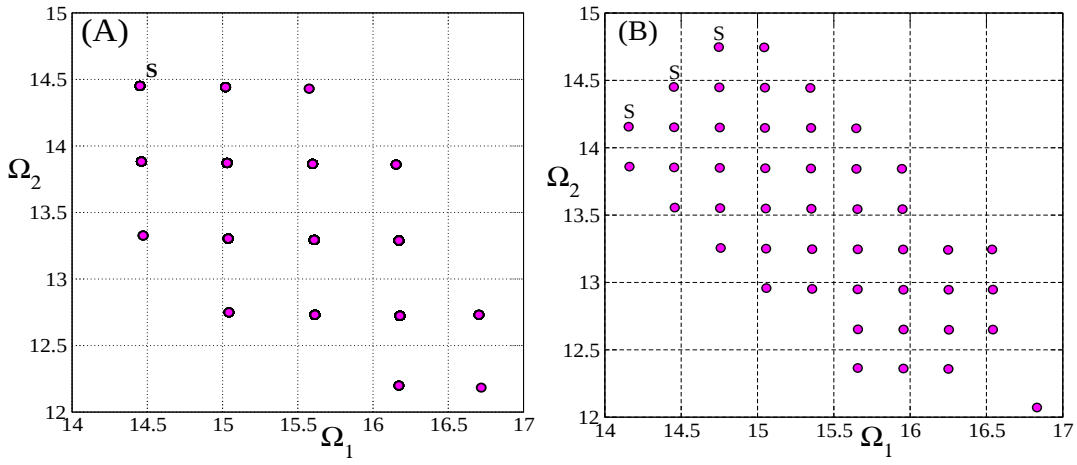

Figure 3.7: Averaged frequencies of the stable solutions illustrated in the plane (Ω_1, Ω_2). Synchronized solutions are marked by letter S. System parameters $\omega_{1,2} = 4.6\pi \pm 2.5$, $K = 3$, (A) $\tau = 5$, (B) $\tau = 10$.

3.1.3 Basins of attraction of synchronized states

Now we will study the basins of attraction of the synchronized states $\theta_{1,2}^{(i)}(t) = \Omega^{(i)}t \pm \alpha^{(i)}/2$ and the allocation of these stable states in the state space for the system (3.2). Because of the infinite dimensionality of the system with delay (3.2) it is impossible to describe the structure of the state space precisely. To overcome

this problem we will use the following method. Let us consider a two-dimensional manifold M of coordinates $(\Omega,\, \alpha)$. Then we consider the initial conditions for system (3.2) in the form of initial functions $\theta_{1,2}(t) = \Omega t \pm \alpha/2$ defined in the interval $t \in [-\tau,\, 0]$. Synchronized solutions belong to the manifold M by definition. We estimate the in-manifold basins of attraction for the synchronized modes. We also describe the structure of the boundaries between different basins of attraction in the manifold M. The basin boundaries consist of the stable manifolds (separatrixes) of the unstable synchronized solutions $\theta_{1,2}^{(u)} = \Omega^{(u)} t \pm \alpha^{(u)}/2$ of the saddle type, i.e., those having one positive eigenvalue.

In the framework of the mentioned approach, the basins of attraction will be analyzed in the two-dimensional plane $(\Omega,\, \alpha)$. Each point $\Omega = \Omega_0;\, \alpha = \alpha_0$ in the plane corresponds to solution $\theta_{1,2}(t),\ t \geq -\tau$ of system (3.2) with the following initial conditions:

$$\theta_1(t) = \Omega_0 t + \frac{\alpha_0}{2},\ \ \theta_2(t) = \Omega_0 t - \frac{\alpha_0}{2},\ \ t \in [-\tau,\, 0].$$

Typical examples of the basins of attraction for the delayed Kuramoto model (3.2) in the plane $(\Omega,\, \alpha)$ are shown in Figure 3.8. Parameters of the system are $\overline{\omega} = 6\pi$, $\Delta\omega = 4$ and $\tau = 0.225$. Basins are calculated for three different values of the coupling strength $K = 30$, $K = 50$ and $K = 70$. Unstable and stable modes are depicted by gray and black dots respectively. The unstable solutions with one positive eigenvalue, i.e., called the saddles, are denoted by S_i. The unstable modes with two positive eigenvalues, the nodes, are labeled by N_i. As we can see, boundaries of basins of attractors contain unstable states being stable manifolds of the saddle states S_i. In the first panel in Figure 3.8 ($K = 30$) we plot two exemplary trajectories (solutions), which are projected onto the plane $(\Omega,\, \alpha)$. One orbit starts at some point inside the green region (basin of the mode O_2), and the second trajectory starts at some point on the boundary separating basins of O_1 and O_2. These projections have been built in the following way: for each moment of time $t = t' > 0$ the interval of length τ, namely $(t' - \tau/2,\, t' + \tau/2)$ is fixed and the phases θ_1 and θ_2 are approximated on this interval by linear functions found by the method of least squares. The spirals in Figure 3.8 ($K = 30$) consist of the points ($\Omega = \langle\dot{\theta}_1\rangle$, $\alpha = \theta_1(t') - \theta_2(t')$) where $\langle\dot{\theta}_1\rangle$ is the result of the least square approximation of phase θ_1 on the interval. Now we analyze behavior of these two trajectories. One

of them (black spiral) starts from the basin boundary and converges to the saddle point S_1, because this basin boundary belongs to the stable manifold of S_1. The second trajectory (blue spiral) starts from the point inside the basin of attraction of stable state O_2 and converges to this state.

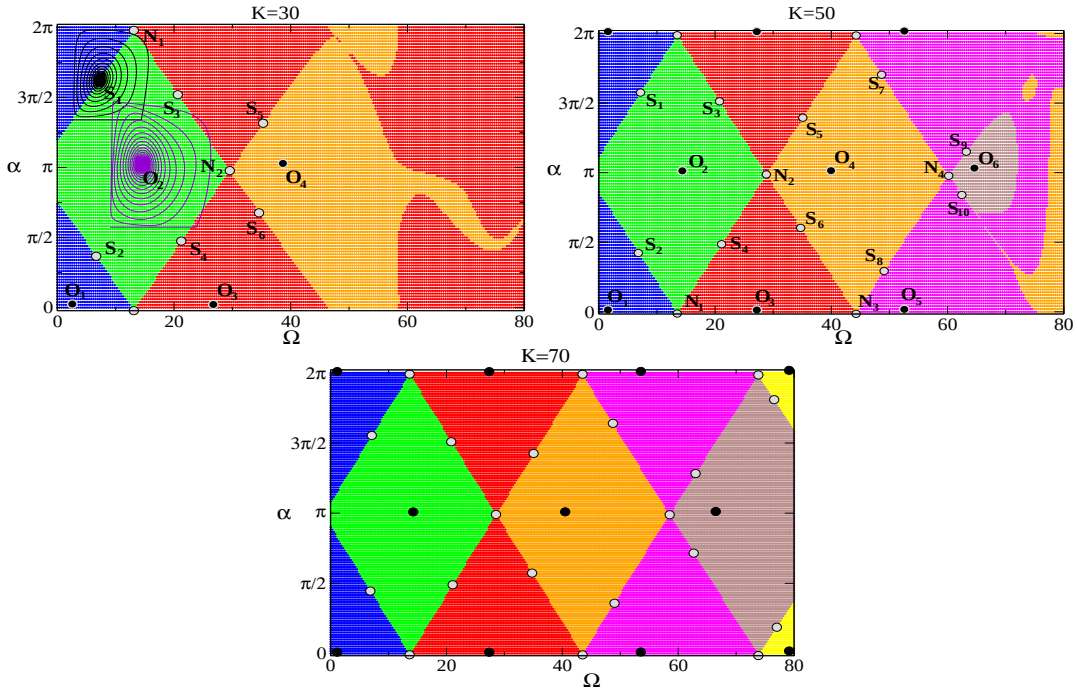

Figure 3.8: Basins of attraction for three different coupling strengths: $K = 30$, $K = 50$ and $K = 70$. Stable and unstable solutions are depicted as black and gray dots respectively: stable synchronized solutions (points O_i), unstable synchronized solutions with one positive eigenvalues (saddles S_i), unstable solutions with two positive Lyapunov exponents (nodes N_i).

We found an interesting feature of basins of attraction, which we can observe in Figure 3.8. The shape of basins of attraction for different stable states starts to resemble a rhomboidal form as K increases.

3.2 The delayed Kuramoto model with feedback

In this section we will study the two-dimensional model of the type that was firstly considered in the article [104]. In that work the high-dimensional systems and the thermodynamical limit where the number of oscillators tends to infinity were investigated. A similar two-dimensional model with delayed feedback and instantaneous interaction between different oscillators was studied in the article [45].

3.2.1 Model and its synchronized solutions

We consider a system of two delayed differential equations (3.7):

$$\begin{aligned} \dot{\theta}_1 &= \omega_1 + \tfrac{K}{2}\left[\sin\left(\theta_1(t-\tau) - \theta_1(t)\right) + \sin\left(\theta_2(t-\tau) - \theta_1(t)\right)\right], \\ \dot{\theta}_2 &= \omega_2 + \tfrac{K}{2}\left[\sin\left(\theta_1(t-\tau) - \theta_2(t)\right) + \sin\left(\theta_2(t-\tau) - \theta_2(t)\right)\right], \end{aligned} \tag{3.7}$$

where ω_1 and ω_2 are the natural frequencies, K is the coupling strength and τ is the time delay. Comparing this model with the model with delayed interaction (3.2), which was considered in section 3.1, one observes that the equations have an additional sin-term with self-delayed feedback $\sin\left(\theta_i(t-\tau) - \theta_i(t)\right)$, $i = 1, 2$. The presence of this term makes the behavior of the system much more complicated, as we will show below in this section.

In order to get better understanding of the system dynamics, we analyse the existence and stability of the synchronized solutions analogous to those studied for the system (3.2). We are looking for solutions of system (3.7)

$$\theta_{1,2}(t) = \Omega t \pm \frac{\alpha}{2} \tag{3.8}$$

where Ω is the frequency of the synchronized solution and α is its phase difference. These two values are to be found. Substituting expressions (3.8) into the system equations (3.7) we obtain the following equations for Ω

$$\overline{\omega} - \Omega = \frac{K}{2}\sin(\Omega\tau)\left(1 - (-1)^i \frac{1}{\cos(\Omega\tau)}\sqrt{\cos^2(\Omega\tau) - \frac{(\Delta\omega)^2}{K^2}}\right), \; i = 1, 2 \tag{3.9}$$

where $\overline{\omega} = 0.5\left(\omega_1 + \omega_2\right)$ is the mean natural frequency, and $\Delta\omega = \omega_1 - \omega_2$ is the

frequency detuning. The corresponding values of the phase difference α are

$$\begin{aligned} i=1 \quad : \quad \alpha &= \begin{cases} \arcsin\left(\frac{\Delta\omega}{K\cos(\Omega\tau)}\right), \text{ if } \cos(\Omega\tau)>0, \\ \pi-\arcsin\left(\frac{\Delta\omega}{K\cos(\Omega\tau)}\right), \text{ otherwise} \end{cases} \\ i=2 \quad : \quad \alpha &= \begin{cases} \pi-\arcsin\left(\frac{\Delta\omega}{K\cos(\Omega\tau)}\right), \text{ if } \cos(\Omega\tau)>0, \\ 2\pi+\arcsin\left(\frac{\Delta\omega}{K\cos(\Omega\tau)}\right), \text{ otherwise.} \end{cases} \end{aligned} \tag{3.10}$$

In order to estimate the stability of the obtained solutions, we have to use the standard method of system linearization around the solution to be studied. As in the section 3.1, we write characteristic equation for complex eigenvalues λ as $\det(A+Be^{-\lambda\tau}-\lambda E)=0$ where A and B are the partial derivatives of our system (3.7) with respect to $\theta_{1,2}(t)$ and $\theta_{1,2}(t-\tau)$, respectively. Then the characteristic equation attains the form

$$\begin{aligned} &\left(e^{-\lambda\tau}\cdot\frac{K}{2}\cos(\Omega\tau)-\lambda-\frac{K}{2}(\cos(\Omega\tau)+\cos(\Omega\tau+\alpha))\right)\times \\ &\times\left(e^{-\lambda\tau}\cdot\frac{K}{2}\cos(\Omega\tau)-\lambda-\frac{K}{2}(\cos(\Omega\tau)+\cos(\Omega\tau-\alpha))\right)- \\ &-e^{-2\lambda\tau}\cdot\frac{K^2}{4}\cos(\Omega\tau+\alpha)\cos(\Omega\tau-\alpha)=0,\ \lambda\in\mathbb{C}. \end{aligned} \tag{3.11}$$

The exemplary diagrams for the frequencies $\Omega=\Omega(K)$ and the corresponding phase shifts $\alpha=\alpha(K)$ versus the coupling strength K are shown in Figure 3.9. One can see in these graphs that one of the stable solutions undergoes a Hopf bifurcation. We will discuss this bifurcation in the following subsection 3.2.2. The phase difference α of the stable synchronized solutions is close to zero or close to π, similarly as for the phase shift for model (3.2) without feedback.

3.2.2 Special features of the delayed model with feedback

In this section we show that the special properties of model (3.7) are different from those of the delayed model (3.2) considered in the previous section 3.1. First of all, for the standard model (3.2) the stable synchronized solutions with different phase shifts, i.e., with $\alpha\approx 0$ and $\alpha\approx\pi$, appear consecutively one after another, but the model with self-feedback (3.7) has an unique stable solution $\theta_{1,2}=\Omega t\pm\alpha/2$ with $\alpha\approx\pi$ (anti-phase solution) *only* if the following condition holds

$$\cos(\overline{\omega}\tau)<0, \ \Leftrightarrow \ 2\pi n+\pi/2<\overline{\omega}\tau<3\pi/2+2\pi n,\ n\in\mathbb{Z}$$

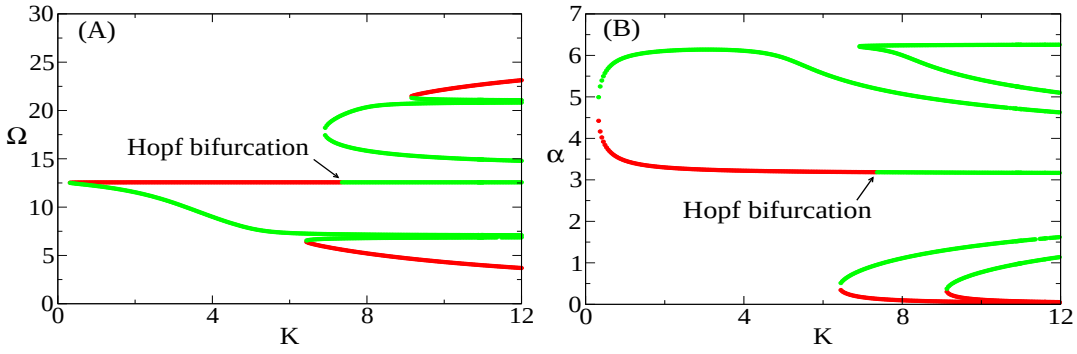

Figure 3.9: Frequencies Ω and phase shifts α for the synchronized solutions of system (3.7). (A) $\Omega = \Omega(K)$, (B) $\alpha = \alpha(K)$. Red points depict stable solutions, whereas green points correspond to unstable ones. Parameters are $\overline{\omega} = 4\pi$, $\Delta\omega = 0.3$ and $\tau = 0.225$.

otherwise the system has only in-phase ($\alpha \approx 0$) stable solutions. Figure 3.9 was created for parameter values providing existence of an anti-phase stable solution with $\cos(4\pi \cdot 0.225) = \cos(0.9\pi) < 0$. The next important feature of the system is that the stable anti-phase solution loses its stability as K increases via a Hopf bifurcation, as shown in Figure 3.9. Hopf bifurcation is characterized by a pair of eigenvalues (roots of Equation (3.11)) simultaneously crossing the imaginary axis from the left half-plane to the right half-plane. The examples of the spectrum of the anti-phase synchronized solution are shown in Figure 3.10 for three different values of coupling strength K: before bifurcation, at the moment of bifurcation and after the bifurcation. These diagrams are created for the same system parameters used for the diagrams in Figure 3.9. The point of bifurcation is denoted by an arrow $K = 7.34336$ in Figure 3.9. As a result of supercritical Hopf bifurcation, synchronized solution of the form (3.8) loses its stability and a new solution becomes stable. This solution has the same averaged frequencies, but the phase difference oscillates around the value α. If we increase the coupling strength further, this new solution undergoes a series of period doubling-bifurcations with respect to the mean period of oscillations of the phase difference and transition to chaos. Afterwards the anti-phase synchronization in system (3.7) is lost via a boundary crisis.

We derive the explicit expression for the bifurcation value K_{bif} of the Hopf bifur-

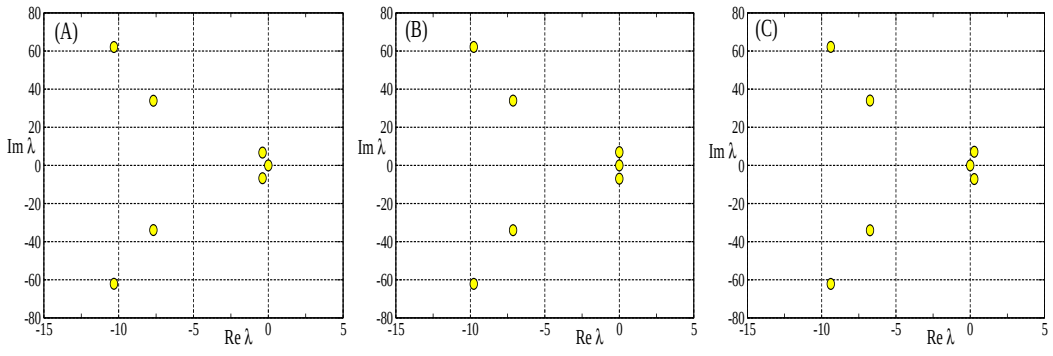

Figure 3.10: Spectra of the synchronized anti-phase solution undergoing Hopf bifurcation. (A) $K = 6.5$, before the bifurcation, (B) $K = 7.34336$, at the moment of the bifurcation, (C) $K = 8$, after the bifurcation, also see Figure 3.9.

cation for the system (3.7) of identical oscillators, i.e., with the natural frequencies $\omega_1 = \omega_2 = \omega$. For this we consider the solution of system (3.7) with the common frequency $\Omega = \omega$ and the phase shift $\alpha = \pi$. For the solution $\theta_{1,2}(t) = \Omega t \pm \frac{\pi}{2}$ the characteristic quasi-polynomial (3.11) can be written in the following simplified form

$$\lambda \left(\lambda - Ke^{-\lambda\tau}\cos(\omega\tau)\right) = 0,\ \lambda \in \mathbb{C}. \tag{3.12}$$

In order to find the bifurcation value of the coupling strength, we have to find such a value of K that implies the presence of roots of equation (3.12) of the type $\lambda = ix$, $x \in \mathbb{R} \setminus \{0\}$. We explicitly look for a pair of purely imaginary eigenvalues since the bifurcation moment is characterized by that a pair of eigenvalues crosses the imaginary axis $\mathrm{Re}\lambda = 0$. Substituting such imaginary roots into (3.12) we obtain

$$x = \frac{\pi}{2\tau}, \text{ and}$$

$$K_{\text{bif}} = -\frac{\pi}{2\tau\cos(\omega\tau)}. \tag{3.13}$$

We briefly consider the stability of the in-phase synchronized solution in the case of identical oscillators ($\omega_1 = \omega_2 = \omega$) $\theta_1(t) = \theta_2(t) = \Omega t$. The frequency Ω of the in-phase synchronized solution can be found from equation

$$K\sin(\Omega\tau) = \omega - \Omega. \tag{3.14}$$

The solution of equation (3.14) always exists, and we will write the conditions of its stability. The characteristic equation (3.11) can be rewritten for this case in the following way:

$$(\lambda + K\cos(\Omega\tau))(K\cos(\Omega\tau)(e^{-\lambda\tau} - 1) - \lambda) = 0,\ \lambda \in \mathbb{C}. \tag{3.15}$$

Analyzing equations (3.14) and (3.15) we can conclude that the in-phase synchronized solution for the system of identical oscillators (3.7) is stable if K is greater than some critical value K_{cr}

$$K_{\text{cr}} = \begin{cases} \min\limits_{n\in\mathbb{Z}} \left|\omega - \dfrac{1}{\tau}\left(\dfrac{\pi}{2} + \pi n\right)\right|, \text{ if } \cos(\omega\tau) < 0. \\ 0, \text{ otherwise.} \end{cases} \tag{3.16}$$

In Figure 3.11 we illustrate dependencies of K_{cr} and K_{bif} on the mean natural frequency $\overline{\omega}$ for the case of identical oscillators $\Delta\omega = 0$. The numerically obtained values K_{cr} and K_{bif} are plotted versus $\overline{\omega}$ in Figure 3.11 also for the case of non-identical oscillators for $\Delta\omega = 1$ and $\Delta\omega = 2$. The graphs of K_{bif} are shown by the solid lines and the graphs of K_{cr} are depicted by the dashed lines. We can see that as frequency detuning $\Delta\omega$ increases the values of K_{cr} and K_{bif} also increase.

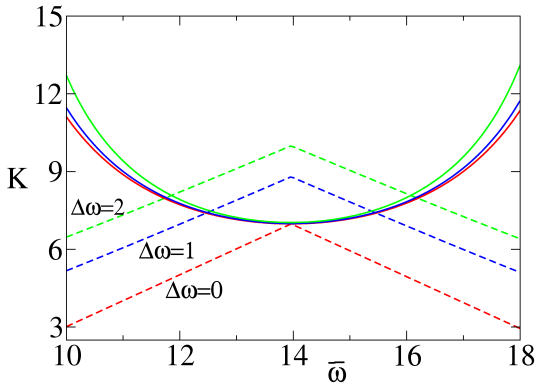

Figure 3.11: The bifurcation values of K_{bif} (solid lines) and K_{cr} (dashed lines) are shown versus $\overline{\omega} = 0.5(\omega_1 + \omega_2)$ for three fixed values of $\Delta\omega$: $\Delta\omega = 0$ (red curves), $\Delta\omega = 1$ (blue curves) and $\Delta\omega = 2$ (green curves). Time delay $\tau = 0.225$.

A more general diagram in the plane $(\overline{\omega}, K)$ describing the system dynamics for the case of identical oscillators is presented in Figure 3.12. A similar diagram for the case

of non-zero detuning is presented in Figure 3.13. Figure 3.12 in particular illustrates what kind of the stable states system (3.7) of identical oscillators exhibits as the coupling strength K increases. In the parameter regions denoted in Figure 3.12 by the letters A-D we observe the following dynamics in system (3.7): (A) only an anti-phase solution is stable; (B) stable in-phase synchronized solution appears; (C) the stable synchronized anti-phase solution undergoes a supercritical Hopf bifurcation and loses its stability and a solution with the same frequency but with oscillating phase difference is born; (D) the oscillating solution loses its stability via a boundary crisis and only in-phase solutions are stable.

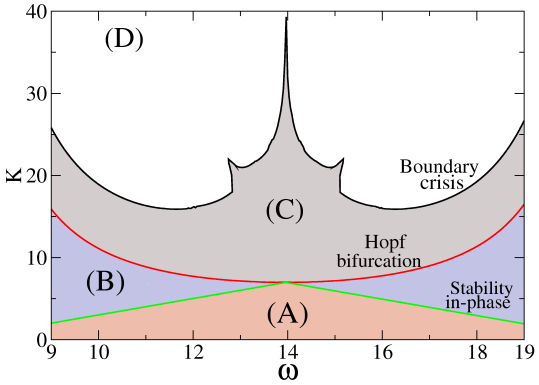

Figure 3.12: System (3.7) of identical ($\Delta\omega = 0$) oscillators, for $\tau = 0.225$. (A) The system has an unique stable anti-phase synchronized solution; (B) Appearance of the in-phase synchronized solution; (C) After a Hopf bifurcation, a synchronized solution with oscillating phase difference is stable; (D) After boundary crisis: only in-phase synchronized solutions are stable.

In Figure 3.13 we can see much more rich dynamics of system (3.7) in the case of non-zero detuning ($\Delta\omega = 3.25$). The lowest (blue) curve corresponds to the appearance of the first synchronized solution in the system where the central part of the curve corresponds to the anti-phase solution and the side parts of the curve show the appearance of in-phase solutions, see also Figure 3.11 and rose line in Figure 3.13. The red curve depicts the points of the Hopf bifurcation of the anti-phase solution where a new synchronized solution with oscillating phase difference becomes stable. Black curve shows the boundary crisis of this synchronized solution. The most

interesting part of the diagram is a green region where desynchronized (with the different averaged frequencies) solution is stable, although the coupling strength is large enough. In this region system (3.7) demonstrates multistability in the sense that the synchronized in-phase solutions and the desynchronized solution are stable for the same parameter values. Such a situation is preserved in all parameter regions of $\overline{\omega}$ satisfying condition $\cos(\overline{\omega}\tau) < 0$.

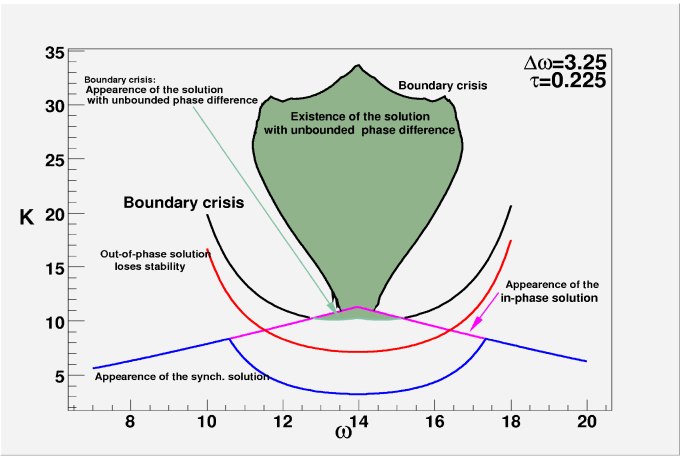

Figure 3.13: System (3.7) of non-identical oscillators with the frequency detuning $\Delta\omega = 3.25$ and $\tau = 0.225$. Green region corresponds to the existence of stable desynchronized solution for large coupling K. Blue curve indicates the appearance of the synchronized solution. Rose curve $K_{\rm cr} = K_{\rm cr}(\overline{\omega})$ depicts appearance of the in-phase synchronized solution. Red curve indicates a Hopf bifurcation $K_{\rm bif} = K_{\rm bif}(\overline{\omega})$ of the anti-phase solution, see also Figure 3.11. Black curves correspond to a boundary crisis of the anti-phase solution (lower line) and of desynchronized solution (upper line surrounding green domain).

The parameter regions where system (3.7) exhibits different dynamical behavior are depicted in Figure 3.14 in $(\Delta\omega, K)$-parameter plane for the fixed value of $\overline{\omega} = \pi/\tau - 1$, time delay is $\tau = 0.225$

Red and violet curves in Figure 3.14 depict the bifurcation curves of the appearance of the first synchronized anti-phase solution and the curve of Hopf bifurcation of the synchronized anti-phase solution $K_{\rm bif}$, correspondingly, see also Figure 3.11.

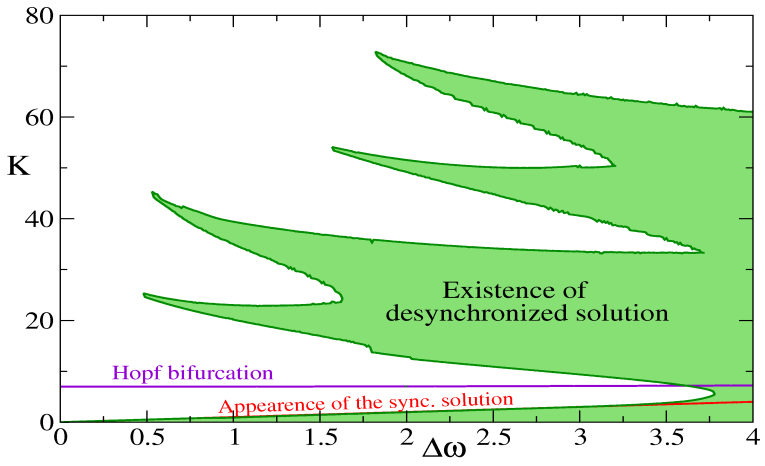

Figure 3.14: Parameter regions of different dynamical regimes of system (3.7) in the plane $(\Delta\omega, K)$, $\tau = 0.225$ and $\overline{\omega} = \pi/\tau - 1 \approx 13.86$. Red line indicates the appearance of the synchronized anti-phase synchronized solution. Violet line K_{bif} depicts the Hopf bifurcation of the anti-phase synchronized solution. Green color depicts a region where the desynchronized solution of the system with self-feedback (3.7) is stable.

The main object of interest in Figure 3.14 is the green region of stability of the desynchronized solution with different averaged frequencies. Part of this region below the curve K_{cr} is easy to understand: here the coupling strength is not large enough to synchronize system (3.7) and the desynchronized solution is stable. For the small values of $\Delta\omega$ the border of this region coincide with the appearance of the stable anti-phase solution. Therefore, there is no multistability for the small values of $\Delta\omega$ and K. Much more interesting for us is the upper part of the green region above the curve of K_{cr} where synchronized and desynchronized solutions coexist for system (3.7) indicating the multistability in the system for such parameter values. One observes in Figure 3.14, however, the presence of "tongues" of the green domain. If we consider $\Delta\omega$ fixed and change the coupling strength, there will be several non-connected intervals of stability of desynchronized solution what we have not observed in the previous section 3.1 devoted to the delayed system without self-feedback.

Figure 3.15 reveals the dependence of the averaged frequencies of the stable solution

of model (3.7) on the coupling strength. The considered parameter values correspond to the case $\cos(\overline{\omega}\tau) < 0$ where one synchronized solution with the common frequency $\Omega = 2\pi$ loses its stability via a Hopf bifurcation and a new solution depicted by orange points appears.

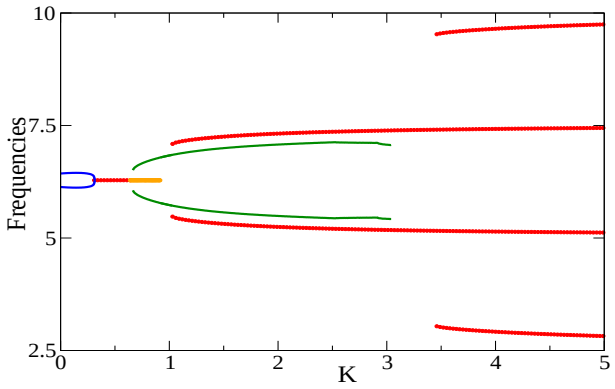

Figure 3.15: The averaged frequencies of the stable solutions of the system (3.7) with parameters $\omega_{1,2} = 2\pi \pm 0.15$ and $\tau = 2.5$. Red points depict phase-locked synchronized solutions, orange points indicate synchronized solution with oscillating phase difference, which appears as a result of Hopf bifurcation, and blue and green points correspond to desynchronized solution.

As mentioned above, in Figure 3.15 we see two non-overlapping parameter intervals of stable desynchronized solutions. The first region of desynchronization (for $K < 0.315$) almost has no overlapping (multistability) with the synchronized solutions, whereas the second one ($0.665 \leq K \leq 3.04$) has prominent overlapping with interval of stable synchronized solution indicating multistability.

The system with self-feedback (3.7) has the same property of frequency discretization as the previous model (3.2). The frequencies of synchronized solutions tend to the values from some grid with increasing coupling strength where the step of this grid is proportional to $1/\tau$. It follows from the properties of equation (3.9) determining the frequencies Ω of the synchronized solution. The functions of the right side of Eq. (3.9) have structure close to that was shown in section 3.1 (butterflies). Thus, solutions of Eq. (3.9) tend to values from some grid with the stepsize proportional to $1/\tau$ as coupling strength K increases. Concerning the averaged frequencies of

the desynchronized solutions, we will demonstrate the quantization effect in the following Figure 3.16.

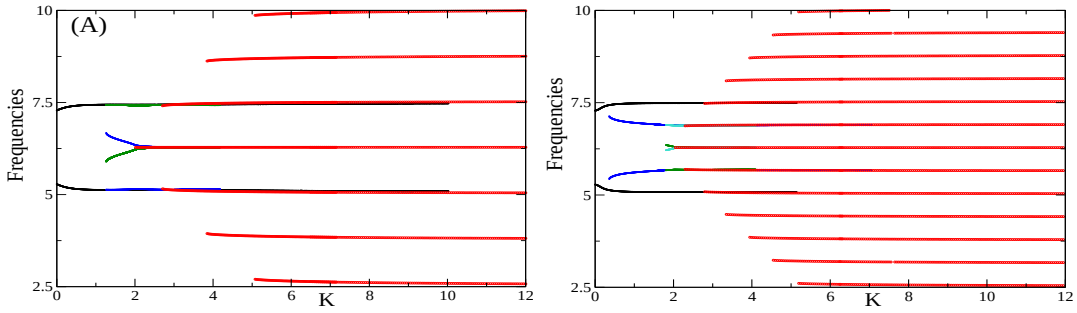

Figure 3.16: The averaged frequencies of the solutions of system (3.7) with $\omega_{1,2} = 2\pi \pm 1.0$. (A) $\tau = 5$, (B) $\tau = 10$. Red points depict synchronized solutions, whereas black, blue, green and turquoise points correspond to different desynchronized solution.

As follows, an increase of τ, for example, in two times results in the corresponding decrease also in two times of the step of the frequency "grid" for the synchronized solutions as well as for the desynchronized states. Therefore, with increasing τ we found linear increasing of the number of synchronized modes. We can conclude that the total number of desynchronized solutions increases as τ^2 as in the case of the system without self-feedback (3.2), see also Figure 3.7.

3.3 Conclusions

In this Chapter we have investigated two different models of two delay-coupled oscillators. The main results of this study are different variants of multistability in these systems. In the model with delayed interaction (3.2) number of synchronized solutions grows linearly with time delay τ or coupling strength K, whereas the number of desynchronized modes increases much faster under growing of time delay. The set of desynchronized solutions correspond to some set of the points in plane of the averaged oscillator frequencies $\left(\langle\dot{\theta}_1\rangle, \langle\dot{\theta}_2\rangle\right)$. These points are situated in some bounded domain and form a grid with stepsize proportional to $1/\tau$. We can see

that for the case of $N = 2$ coupled oscillators the total number of all desynchronized solutions increases quadratically with τ. Furthermore, we can expect that for such a system of N oscillators ($N > 2$) number of different desynchronized states may grow proportionally to τ^N as τ increases. The model with self-feedback (3.7) demonstrates much richer dynamics, so it is more difficult to perform a comprehensive study of it. But we can conclude that several features of both models are very similar, e.g., frequency discretization with increasing time delay τ.

These results are also important from the point of view of possible application to the development of novel deep brain stimulation (DBS) technique. The main idea of such novel technique can be implementation of the shift of the system dynamics from some undesirable (synchronized) state to the desirable (desynchronized) one. Such study in the case of the neuronal system with plasticity has been already performed in the Chapter 2 of the present thesis and in numerous theoretical works, see [35,36, 89, 91]. The common approach in these two directions of the present thesis (spike timing-dependent plasticity and time delay) is to consider multistability of different states and also their basins of attraction. Structure of the basins of attraction allows us to perform the mild perturbation providing long-lasting switching of the system dynamics between different states. Since we expect that the behavior of the delayed systems for $N > 2$ is similar to our result in the case $N = 2$, we may hypothesize that some desynchronizing stimulation protocols may exploit the special pathological features of networks, e.g., large delay or large coupling, to shift the system to desynchronized state. Such an approach can be transformed to clinical stimulation protocol with long-lasting therapeutic effects and, consequently, require smaller amount of stimulation compared to the standard (HF) protocol.

Chapter 4

Coordinated Reset Stimulation

In this Chapter we study dynamical properties of coordinated reset (CR) stimulation protocol when the system and stimulation parameters vary. CR stimulation technique was originally developed in the theoretical works [84, 85] in order to improve the existing method of deep brain stimulation (DBS) [6, 15]. From the one hand, CR stimulation method is aimed to be much milder decreasing the total amount of administered electrical current in the brain tissue. On the other hand, CR stimulation effectively desynchronizes neuronal population letting the individual neurons to fire in a perturbation-free transient desynchronous regime, which is a very important feature of the new method. The latter property of CR stimulation distinguishes it from the standard high-frequency deep brain stimulation (HF DBS) technique, which is known to significantly alter the individual dynamics of the stimulated neurons by suppressing or overactivating them [11, 72]. During the last decade several desynchronizing stimulation approaches have been developed including, among other, double-pulse reset stimulation [80–83]; multisite delayed feedback stimulation [31, 32, 90], nonlinear delayed feedback stimulation [28, 61–63, 90].

Among these stimulation techniques CR stimulation is one of the most promising from the point of view of application. The desynchronization effect of CR stimulation is characterized by its robustness with respect to the change of the system and stimulation parameters. The impact of the method on the behavior of the neuronal system and optimal values of the stimulation parameters can be investigated with

the methods of nonlinear dynamics, which attracts a great research interest to this type of DBS technique [33, 36, 90, 91]. In the present Chapter we theoretically study coordinated reset stimulation protocol. However, the mentioned works utilized CR stimulation with fixed parameters. The goal of the present investigation is to find the optimal stimulation parameters using different estimation techniques.

We briefly overview the main results obtained in the above works. The main object of study of the articles [84, 85] is the network of coupled phase oscillators (the Kuramoto model) under impact of CR stimulation. The network was subdivided into four equal subpopulations, assigned to four stimulation sites, being stimulated via the corresponding stimulation site with the corresponding stimulation sign. More precisely, the subpopulations are split into two pairs, the subpopulations in the same pair are simultaneously stimulated with the similar stimulation signal having opposite polarity. The onset of the stimulation in the second pair of the subpopulations is shifted in time by $T/4$ where T is the period of oscillations of the oscillators. After the offset of the stimulation the subpopulations form a four-cluster state uniformly distributed on the unit circle. The effective mechanisms of the choice of the rest time interval between two subsequent stimulations were considered as (a) with demand-controlled times of switching the stimulation on where the order parameter R_1 reaches value 0.5, (b) periodic stimulation with controlled length of individual stimulus.

In the study [91] the behavior of the system ($N = 100$) of coupled phase oscillators (the Kuramoto model) was considered where the oscillators are assumed to be arranged in the square-form grid. An important feature of that study was the involving of spike timing-dependent plasticity (STDP) into the model such that coupling was represented by a square matrix $K_{ij}(t)$ of the variable individual couplings between ith and jth neurons. The stimulation was performed via four contacts, which are situated in vertices of a smaller square. Such a system has an important feature of multistability due to plasticity and stimulation allows to switch between two stable states: synchronized and desynchronized ones. The novel stimulation technique was compared with the standard high-frequency stimulation technique.

In the works [33, 36, 90] an ensemble of coupled neurons represented by microscopic models was considered. Neurons were supposed to be arranged in a square-form

grid like in the work [91]. There was considered a modification of the Morris-Lecar model [55], which is able to demonstrate bursting activity, whereas the original model produces only tonic spiking. Also, the STDP was implemented in this model. The main attention of those studies was paid to the effectiveness of the novel CR stimulation technique in comparison to the standard HF stimulation.

In this thesis we will investigate several models of neuronal networks. In the following sections we consider phase model based on the Kuramoto system (section 4.1) and a neuronal model based on the system of FitzHugh-Nagumo neurons (section 4.2).

4.1 Coordinated Reset of the system of phase oscillators

In this section the model of coordinated reset stimulation of the Kuramoto system of phase oscillators is investigated. The considered model based on the phase oscillators cannot demonstrate such peculiar features of the real neurons as bursting, excitability etc. Nevertheless, it is important to study such model due to its ability to reflect some phenomenological macroscopic effects like synchronization, which is one of the most interesting and important phenomena for the real applications.

4.1.1 Model of the CR stimulation

In order to introduce the model of coordinated reset stimulation let us first consider a schematic description of the stimulating electrode for DBS with several contacts. In the part (A) of Figure 4.1 we depict a schematic draw for 4-contact stimulating electrode where the stimulation contacts are shown by red color, whereas insulator inter-contact intervals are depicted by green color. The brain tissue surrounding electrode can be considered (in the framework of our model) as cylindrical surface S, which is built around the electrode's longitudial axis. Therefore, all points of the surface are equally distanced from the electrode.

Part (B) of Figure 4.1 shows the unwrapped cylindrical surface S, which was shown

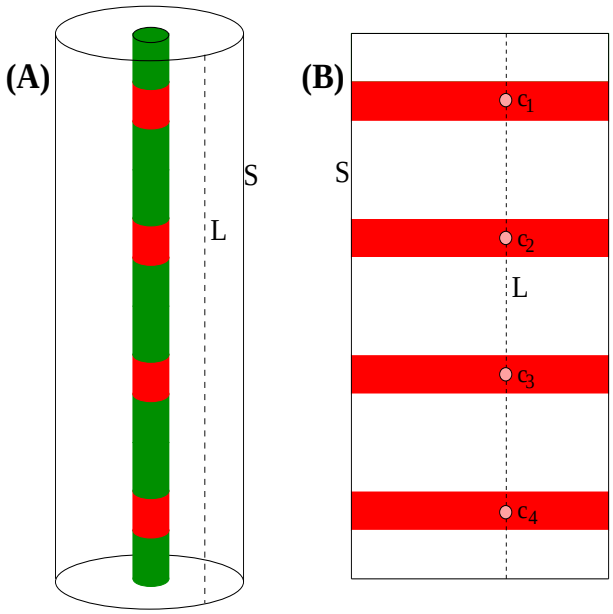

Figure 4.1: (A) Schematic draw of the stimulating electrode with four contacts. S is a cylindrical surface equidistant from the electrode. Contacts are shown by red color and insulator is shown by green color. (B) Unwrapped surface S.

in (A), surrounding the electrode. Unwrapping transforms cylinder to a rectangle where the red color depicts the "rings" of the surface, which are exactly facing the contacts of the electrode indicated by red color in Figure 4.1(A). If we consider the neurons along a straight line L from the cylindrical surface depicted by the dashed line in Figure 4.1(A), they correspond the neurons located along the dashed line L in the rectangle shown in Figure 4.1(B). All such neuronal populations have the same properties since they are placed on the same distance from the electrode and are fully equivalent from the point of view of received stimulation from the electrode. We can conclude that the properties of the neuronal population on the whole rectangle (B) are identical to the properties of the neurons on the line L from the point of view of the impact of the stimulation received from the stimulating electrode. Therefore, we can restrict our consideration of the neuronal network on the surface S to the case of neuronal population arranged in an one-dimensional lattice. The next step to simplification of our model is to replace the red intervals on the line L corresponding

to the stimulating contacts by their central points, which are shown in Figure 4.1(B) as c_1, c_2, c_3, and c_4. We will model the behavior of the neuronal population, that is arranged on line segment. The distances between the neighboring neurons are the same, and the neurons' coordinates x_j, $j = \overline{1, N}$ are given by expression (4.1). The distance between two consecutive contacts is constant and is two times larger than that between the first(last) contact and the corresponding end of the whole segment. Thus, we suppose that all contacts are uniformly distributed over the segment $[0, L]$. In what follows, the length of the segment $L = 10$. If the number of contacts equals N_c, then their coordinates c_i are given by the first formula in expression (4.1).

$$\begin{aligned} c_i &= (i - \frac{1}{2}) \cdot \frac{L}{N_c}, \ i = \overline{1, N_c}, \\ x_j &= \frac{j-1}{N} \cdot L, \ j = \overline{1, N}. \end{aligned} \tag{4.1}$$

Further we will use a system of $N = 200$ coupled phase oscillators. The schematic draw for the oscillators and stimulating contacts is shown in Figure 4.2.

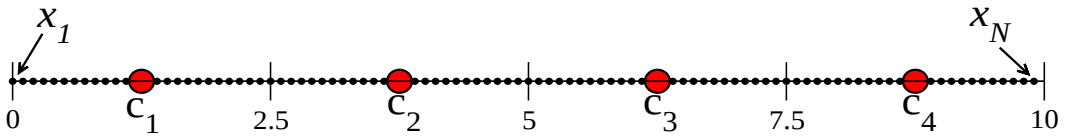

Figure 4.2: Schematic representation of neuronal population and stimulating contacts. The interval is of the length $L = 10$ of one-dimensional lattice and the number of contacts $N_c = 4$. For the illustrational purposes we consider $N = 100$ oscillators.

The spatial structure, i.e., the arrangement of oscillators and contacts, is not important if we consider pure dynamics of the Kuramoto model of globally all-to-all coupled phase oscillators without stimulation. Nevertheless, if one studies the impact of electrical stimulation on the neuronal population, the question of the topological arrangement of the stimulated neurons and the stimulating sites becomes crucial. Indeed, the influence of the electrical stimulation on the neuron strongly depends on their relative spatial positions. This problem is considered in many works devoted to the deep brain stimulation, see, e.g., [65,105]. In many theoretical works, see [31,91], the current spread is supposed to have an exponential form, i.e., the strength of the stimulation decays with increasing of distance between the contact and neuron as

$\sim \exp(-\alpha \left\| x_j - c_i \right\|^{\beta})$ where α, β are some positive coefficients. In the present thesis we will use quadratic decay of the stimulation, as it has been considered in [65]. The following expression (4.2) describes the decay of the stimulation strength, which will be used in our further analysis:

$$\begin{gathered} \tilde{I}_{ij}(t) = I_i(t) D(x_j,\, c_i),\ i = \overline{1,\, N_c},\ j = \overline{1, N}, \\ D(x_j,\, c_i) = \frac{1}{1 + \left| x_j - c_i \right|^2 / \sigma^2}\,. \end{gathered} \tag{4.2}$$

Here, $\tilde{I}_{ij}(t)$ is the time-dependent strength of stimulation received by the jth oscillator from the ith stimulating contact, $I_i(t)$ is the original stimulation signal of the ith contact, $D(x_j,\, c_i)$ is the decay coefficient with the values between 0 and 1, $|x_j - c_i|$ is the distance between the oscillator j and contact i. Parameter σ gives us the distribution width of the stimulation current. This coefficient of the distribution width is one of the most important parameters in our model. Indeed, this parameter determines how large part of the whole neuronal population is under impact of the single stimulation contact. Therefore, σ is one of the main parameters under consideration in the following analysis of the system. We cannot influence the changes of this parameter in the real stimulations since it is a property of the brain tissue. However, we have to understand the special features of the system behavior for different values of σ in order to provide the appropriate values of other stimulation parameters. The next Figure 4.3 shows exemplary decay coefficients $D(x,\, c_i),\ i = \overline{1,\, 4}$ (for all four stimulating contacts) as functions of the oscillator positions on the lattice x for the value of $\sigma = 0.4$, which will be used in some further simulations. Here we should mention several important features of the decay coefficients $D(x, c_i)$. First of all, the width of the graph peak depends on σ such that small σ implies narrow peak, whereas large values of σ correspond to wide peak. The height of all peaks is constant and equals to 1. Each oscillator in the lattice (represented by the point in the interval $[0,\, L]$) is under influence of the stimulation from all stimulating contacts. Figure 4.3 reveals the intervals in the segment $[0, L]$ where different contacts have the same or comparable impact on neurons from such locations in the lattice (intervals around points 2.5, 5, 7.5, which are equidistant, correspondingly, from the c_i and $c_{i+1},\ i = \overline{1,3}$). The presence of such intervals significantly complicates the system dynamics making it very nontrivial. Indeed, we cannot subdivide the whole neuronal ensemble on subpopulations assigned to

a single fixed stimulating contact. As we can see in Figure 4.3, such intervals of the overlapped stimulation current are relatively large already for $\sigma = 0.4$ and they becomes larger with further increasing of σ (because of increasing peak width). To understand the influence of such overlapping stimulation profiles on the outcome of the CR stimulation method the CR-stimulated system requires detailed analysis.

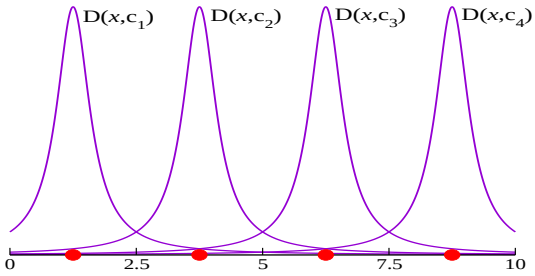

Figure 4.3: Decays of stimulation strengths $D(x,\, c_i)$, $i = \overline{1,\, 4}$, $\sigma = 0.4$, as functions of oscillator position $x \in [0,\, 10]$. Red circles depict stimulating contacts.

Keeping in mind that the total stimulation strength for the jth oscillator is equal to the sum of $\tilde{I}_{ij}(t)$ (see Eqs. (4.2)) over all i, we can write a model for a neuronal system under coordinated reset stimulation. This model is based on the standard Kuramoto system of coupled phase oscillators:

$$\dot{\theta}_j = \omega_j + \frac{K}{N}\sum_{k=1}^{N}\sin\left(\theta_k - \theta_j\right) + \underbrace{\left(\sum_{i=1}^{N_c} I_i(t) D(x_j,\, c_i)\right)\cos\theta_j}_{\text{stimulation term}},\ j = \overline{1, N}, \tag{4.3}$$

where ω_j are the natural frequencies of individual oscillators distributed according to some predefined unimodal density function. In what follows Gaussian (normal) distribution with the mean value $\omega_{\text{mean}} = \pi$ and the standard deviation 0.02 will be used. K is the coupling strength in the system. The value $K = 0.1$ will be taken in our following analysis where the Kuramoto threshold coupling value of the transition to synchronization for the mentioned distribution of ω_j is ≈ 0.032. Therefore, our coupling is strong enough and, as we will show later, it provides value of the first order parameter $R_1 \approx 0.98$. As follows from the above distribution of the natural frequencies, the mean period of the system is $T_{\text{osc}} = 2\pi/\omega_{\text{mean}} = 2$.

The electrical stimulation of a real neuron is phase-dependent [10]. This means that the neuronal response on external stimulation depends on the neuronal state. For example, response of the firing neuron is insignificant, whereas the stimulus application to the neuron in the resting state evokes spike or burst. Therefore, we can write the external stimulation of the Kuramoto model as $I\cos\theta_j$ where I is the aggregate stimulation strength [79] providing the phase-reset (phase converges to some fixed value) if stimulus is strong enough.

As the next step in the description of a model (4.3) we formulate the expression for the stimulation protocol, which is determined by the time-dependent functions $I_i(t)$. The original idea of CR stimulation (see [85]) is to achieve a transient desynchronized state in the system via a clustered state. We consider this outcome of CR stimulation below in more detail. The clustered state can be reached by a consecutive stimulation via different stimulating contacts. Indeed, such stimulation protocol provides consecutive reset of different subpopulations and splits the original one-cluster state into N_c clusters. During the stimulation through each stimulation contact a short high-frequency (HF) pulse-train is administered. The expressions for the functions $I_i(t)$, $i = \overline{1,\, N_c}$ are

$$\begin{aligned} I_i(t) &= I \cdot \mathrm{Ind}_i(t) = I \cdot \mathbb{I}_{\left[t_{\mathrm{begin}},\, t_{\mathrm{end}}\right]}(t) \times \\ &\times \left\{ \sum_{s=0}^{\infty} \sum_{p=1}^{N_p} \mathbb{I}_{[0,\, \delta T_p]} \left(t - \left(t_{\mathrm{begin}} + Ts + \frac{T}{N_c}(i-1) + T_p(p-1) \right) \right) \right\}. \end{aligned} \tag{4.4}$$

Here I is the stimulation strength, $\mathrm{Ind}_i(t)$ is a function of t taking two values 0 and 1 and detecting whether the ith contact is stimulating in the time moment t. $\mathbb{I}_A(x)$ is an indicator function of the set A and equals 1 if $x \in A$ and 0 otherwise. $[t_{\mathrm{begin}},\, t_{\mathrm{end}}]$ is a time interval where the stimulation is switched on. T is period of CR stimulation and T_p is period of pulses in the high-frequency train. In other words, T determines the period of the entire cycle of activity of all N_c stimulating contacts. Period T_p is equal to the time between starts of two consecutive pulses in one HF pulse-train. The sum over s is taken over the stimulation periods. Indeed, if we consider the fixed value of s, we obtain the function defining N_p pulses. This pulse series is shifted from the start of stimulation t_{begin} on time Ts. Therefore, for the fixed value of s we have the stimulation administered via the ith contact on the $(s+1)$th stimulation period. Variable p goes over the predefined number of pulses

N_p, which will be discussed later. All pulses have the same period T_p, which is much smaller than the stimulation period T. In real applications it is smaller than $0.05T$. The exemplary real values are $T = 0.25$ s, $T_p = 1/130 \approx 0.0077$ s. Indeed, T_p is defined by the frequency of the standard HF stimulation, which is often taken as 130 Hz [7, 46]. In our further considerations we will use value of $T = T_{\text{osc}} = 2$ and $T_p = 0.05$. In subsection 4.1.5 we study the dependence of the stimulation effect on the stimulation period T where T is varying.

The pulse period T_p consists of two parts. The active part has the length δT_p where the stimulation is switched on and the rest part without stimulation has the length $(1 - \delta)T_p$. Therefore, coefficient $\delta \in (0, 1)$ determines the relative length of the stimulation during one pulse period. To account this, we put an indicator function of the segment $[0, \delta T_p]$ under the sum over all N_p pulses. In the real applications pulses have more complicated form, e.g., there are two parts with the opposite signs in order to provide the charge balance of the stimulation. In the present study we consider the simpler case with one positive pulse during the pulse period. In all further simulations the value of $\delta = 0.5$ is used. This means that stimulus is switched on during one half of the pulse period. In expression (4.4) the part in the figure braces gives a sequence of the pulse trains of N_p pulses for ith stimulating contact starting from the time t_{begin}. An indicator function $\mathbb{I}_{[t_{\text{begin}},\, t_{\text{end}}]}(t)$ restricts the stimulation exactly to the time interval $[t_{\text{begin}},\, t_{\text{end}}]$.

In the considered stimulation protocol we assume that during the stimulation period T all N_c stimulation contacts administer their stimulation pulse trains to the neuronal tissue. In this way we also assume that each stimulation contact is active during the time interval of the length T/N_c. Therefore, the number of pulses in the corresponding time interval is $[T/(N_c T_p)]$ where square braces denote the integer part of the number (maximal integer, which is not larger than expression in braces). And the remaining interval of length $T/N_c - T_p \cdot [T/(N_c T_p)]$ is supposed to contain one pulse if its length is larger than the width of the pure pulse, i.e., δT_p. Summing this up, we can obtain the number of single pulses N_p administered during the stimulation period via a single stimulation site.

$$N_p = \left[\frac{\frac{T}{N_c} + (1 - \delta)T_p}{T_p} \right]. \tag{4.5}$$

For example, if we consider a 4-contact model with parameters $T = 2$, $T_p = 0.05$ and $\delta = 0.5$, then N_p is equal to 10. This system's configuration is the most common in our investigations. In the following Figure 4.4 the functions $\mathrm{Ind}_i(t)$ for the exemplary case of $N_c = 4$ are shown.

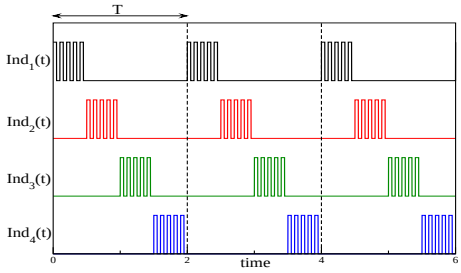

Figure 4.4: Stimulation signals of four contacts $\mathrm{Ind}_i(t)$, $i = \overline{1,4}$ from Eq. (4.4). System parameters $T = 2$, $\delta = 0.5$, and $T_p = 0.1$ is taken for the illustrational purposes, whereas in all simulations $T_p = 0.05$.

As we can see in Figure 4.4, the expressions for the stimulation activity (4.4) and (4.5) correspond to the idea of coordinated reset stimulation. Indeed, we have a consecutive stimulation via different stimulation contacts, and each contact performs a HF pulse-train stimulation. The values of the stimulation parameters of pulse period T_p, pulse width determined by values of δ, and the number of single pulses N_p in the pulse-train are fixed in this work and considered to be $T_p = 0.05$, $\delta = 0.5$ and $N_p = 10$.

In this subsection we have introduced model (4.3), which will be investigated in detail in the following subsections. To understand the influence of different system parameters on the stimulation outcome, we have to know the basic properties of the model. Thus, the impact of a HF pulse-train stimulation on a single neuron is important for the understanding of the entire dynamics of the system during CR stimulation. In the following subsection 4.1.2 we consider several basic resetting features of a HF pulse-train stimulation administered to the oscillators of the model (4.3).

4.1.2 Resetting properties of CR stimulation

In this subsection we will describe some fundamental properties of the coordinated reset stimulation, which is necessary for further analysis. First of all, in order to understand the dynamics of the system under impact of the CR stimulation by several ($N_c = 4$) stimulating contacts, we have to study the behavior of the system in the case of a single contact performing HF stimulation. It is well known [79,85] that strong enough stimulation results in the resetting of the neurons, i.e., their phases stop the natural growing and perform low-amplitude oscillations around some fixed value. Here, we will give a numerical estimation of such a phenomenon.

Consider the Kuramoto model with a single stimulating contact, which is placed exactly in the middle of the population segment $[0, L]$, $c_1 = L/2$.

$$\dot{\theta}_j = \omega_j + \frac{K}{N}\sum_{k=1}^{N}\sin\left(\theta_k - \theta_j\right) + I \cdot D\left(x_j, \frac{L}{2}\right) \cdot \left(\sum_{p=0}^{\infty}\mathbb{I}_{[0,\delta T_p]}\left(t - T_p p\right)\right)\cos\theta_j, \quad (4.6)$$

where function $D(\cdot,\cdot)$ is taken from Eq. (4.2). We can see that system (4.6) is a simplification of the general model (4.3) for the case of a single stimulation contact administering a permanent HF pulse train. In the following Figure 4.5 the averaged oscillators' frequencies are shown versus the stimulus strength I.

As revealed by Figure 4.5, if we consider frequency of some oscillator under variation of the stimulation strength, this frequency decays from the level of the synchronized system without stimulation, i.e., the common synchronized frequency is equal to $\omega_{\text{mean}} = \pi$, to zero value. The zero value of the averaged frequency corresponds to the full reset of the oscillator.

We can also see in Figure 4.5 that the resetting HF pulse-train stimulation can have different impacts on the stimulated oscillators. If the stimulation is weak, it does not significantly influence the frequency of the oscillator. For a stronger stimulation the oscillators are quickly slowed down. Finally, the oscillators are completely blocked where the frequencies vanish indicating that the stimulated oscillators are fully reset. Another important property of such a stimulation is a heterogeneous impact of the stimulus on the neuronal population due to decay of the stimulation strength. This decay is given by function $D(\cdot,\cdot)$ from Eq. (4.2). We can see that different curves

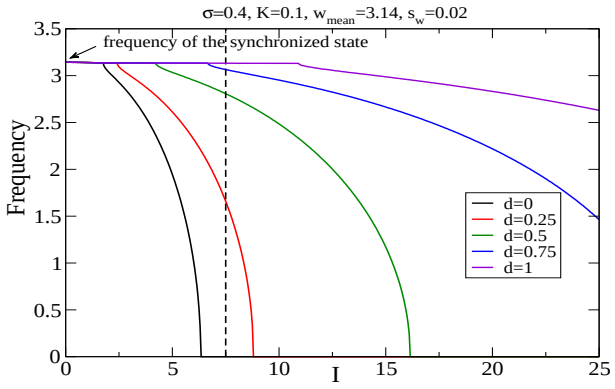

Figure 4.5: Impact of the permanent HF stimulation via a single contact, the averaged frequencies of five oscillators vs. stimulation strength are shown. The legend indicates the distances d between the placements of the corresponding oscillators and the stimulation contact.

in Figure 4.5, which correspond to the different oscillators, are characterized by the different critical values of I providing the full reset or start of the fast decay of the averaged frequencies $\langle \dot{\theta}_j \rangle$. The fastest resetting is demonstrated by the nearest to the contact neuron corresponding to the black curve where position of neuron coincides with the stimulating site. One can make conclusion that such a stimulation results in the total reset of the whole population in the case of large I. Indeed, if I is large enough, all neurons are suppressed and have zero averaged frequency. The stimulation can theoretically lead to a partial desynchronization in the system since all oscillators are stimulated with different strength, which results in the different frequencies, i.e., in a partial desynchronization. As an example, it is possible to consider the strength value $I = 7.5$, which is indicated in Figure 4.5 by dashed line. It is evident that all shown oscillators have for this stimulation strength different averaged frequencies and are thus desynchronized.

On the other hand, according to coordinated reset stimulation protocol, each stimulating contact performs sequentially quite short of the length T/N_c high-frequency stimulation. Therefore, the system behavior can be different from the above dynamics considered under the permanent stimulation. Figure 4.5 cannot explain the neuronal resetting in the case of moderate stimulation, e.g., in the interval of the

frequency decay from the synchronized mode to zero, see the black curve for $d = 0$ and $I = [1.75, 6.35]$. To provide a necessary analysis, the *cross-trial* (CT) technique can be useful. This method was discussed in detail in works [86, 87]. This technique allows to estimate how stereotypical the response of the oscillators on the stimulus is. Here we give a short description of the CT technique and its application to our problem.

The idea of the CT-analysis is to consider a large number (we use $N_{\text{trials}} = 1000$) of quite short stimuli to be analyzed in some specific manner. The series of the mentioned stimuli is delivered at random times $\tau_1, \tau_2, \ldots, \tau_{N_{\text{trials}}}$. The length of the time intervals between the stimuli is randomized according to

$$\tau_{k+1} = \tau_k + w + \xi_k, \tag{4.7}$$

where w is constant and large compared to the time scale of the system. ξ_k is uniformly distributed in $[0, 2\pi/\omega_{\text{mean}}]$. We attach an identical time window $[t_a, t_b]$ to each stimulus. It is supposed that inequalities $t_a < 0 < t_b$ and $t_b - t_a < w$ hold. The latter inequality guarantees the window length to be smaller than the length of interstimulus interval. Each window has a time axis t'. Therefore, $t' \in [t_a, t_b]$ and the onset of the stimulus in each window corresponds to $t' = 0$. In what follows, we drop the prime in t' for the sake of simplicity. We can consider the time-dependent distributions of the phase variables $\{\theta_j (t + \tau_k)\}_{k=1,\ldots,N_{\text{trials}}}$.

The CT technique is utilized here for analysis of the behavior of the oscillator, which placement coincides with the stimulating contact, i.e., $x_j = 5$, $j = 101$. We take $t_a = -10$ and $t_b = 70$. To quantify the extent of stimulus locking of phase θ_j for each time t we use the first stimulus locking index $\lambda^{(1)}(t)$ [87].

$$\lambda^{(1)}(t) = \left| \frac{1}{N_{\text{trials}}} \sum_{k=1}^{N_{\text{trials}}} \exp\left[i\, \theta_j\, (t + \tau_k)\right] \right|. \tag{4.8}$$

The main task of CT technique is to verify whether the response of the stimulated oscillator on stimulation is stereotypical. This can be evaluated by considering the large number of such "random" trials and estimating the response of the system on the stimuli for a variety of initial conditions. As an approach to the above analysis we use the stimulus locking index technique. Here, we base our analysis of the first

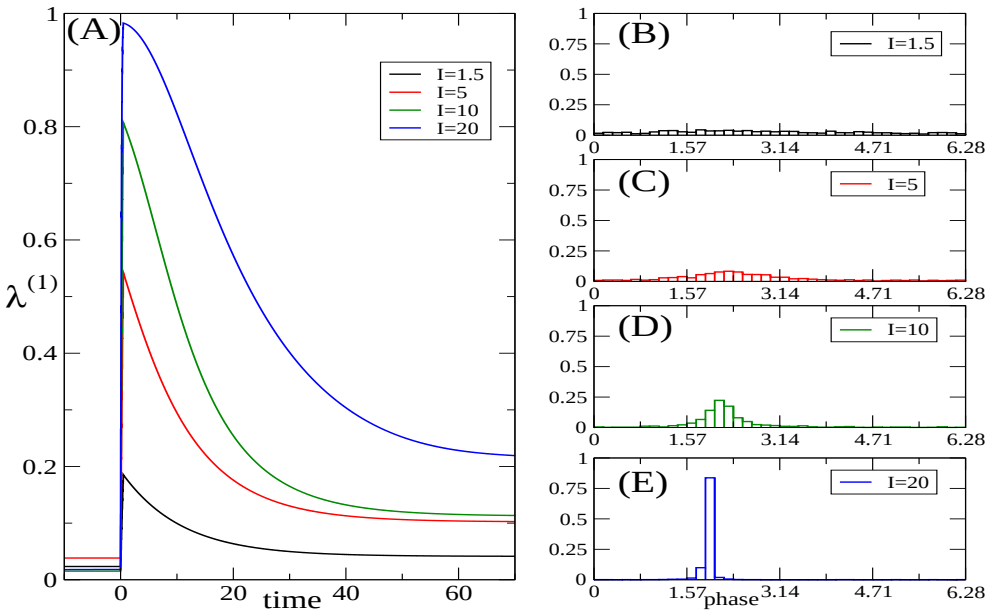

Figure 4.6: Cross-trial analysis of the HF stimulation via a single contact. Stimulation interval $t \in [0, 0.5]$ and the number of trials $N_{\text{trials}} = 1000$. (A) The first stimulus locking index $\lambda^{(1)}$ of the phases of oscillator with $x_j = 5$ (coincides with the contact) for the different values of the stimulation strength I. (B)-(E) The corresponding phase distributions $\{\theta_j(t + \tau_k)\}_{k=1,\ldots,N_{\text{trials}}}$ at the moment $t = 0.5$ (end of the stimulation) for four different stimulation strengths.

stimulus locking index $\lambda^{(1)}(t)$. The time courses of the index $\lambda^{(1)}(t)$ for different values of the stimulation strength are shown in Figure 4.6(A). As we can see here, the prestimulus interval $t \in [-10, 0)$ is characterized by negligibly small values of the first stimulus locking index $\lambda^{(1)} \sim (N_{\text{trials}})^{-1/2}$. Indeed, these values correspond to the uniform distribution of phases $\{\theta_j(t + \tau_k)\}_{k=1,\ldots,N_{\text{trials}}}$, $t < 0$. After the stimulation is switched on, we observe a fast increasing of $\lambda^{(1)}$ reaching its maximal value at the end of stimulation of the length 0.5. This time interval corresponds to the length of the active phase of a stimulation site in the case of CR stimulation administered via four stimulation sites and the stimulation period $T = 2$. We note here that the reached value of the stimulus locking index crucially depends on the stimulation strength where the larger values of I imply the larger values of $\lambda^{(1)}$. Therefore,

stronger stimulus results in more stereotypical response on the applied stimulation.

Subplots (B)-(E) in Figure 4.6 show distributions of phases after the end of stimulation at $t = 0.5$ where the highest level of $\lambda^{(1)}$ is reached. We can see consecutive transformation of the almost uniform distribution in the subplot (B) ($\lambda^{(1)} \approx 0.185$) to the distribution with narrow peak in the subplot (E) ($\lambda^{(1)} \approx 0.983$). One can note an interesting fact that after the end of stimulation we observe a process of system relaxation where the limit value of $\lambda^{(1)}$ is prominently larger than its initial value before stimulation. We present here a brief explanation of this phenomenon. Before the stimulus the whole system is characterized by the random values of its phases $\{\theta_j(t + \tau_k)\}_{k=1,\ldots,N_{\text{trials}}}$, $t < 0$. Here, the phases are tightly locked, randomness is reached due to the random choise of τ_k, see Eq. (4.7). The stimulation affects some subpopulation of oscillators according to the strength decay $D(\cdot, \cdot)$. Dynamics of this neuronal subpopulation becomes stereotypical depending on the stimulation strength, see Figure 4.6(B)-(E). Therefore, we can roughly say that after end of stimulation we have two different subpopulations in the system. The first subpopulation is unaffected by stimulation and has random phases. The second group of neurons, which phases are determined, i.e., are distributed closely to $\pi/2$. As the relaxation starts, the whole system resynchronizes to some intermediate state. The values of $\theta_j(t)$ are not uniformly distributed on $[0, 2\pi]$ due to non-zero size of the second mentioned subpopulation. Therefore, the limit value of $\lambda^{(1)}(t)$ after the relaxation is always larger than the values before the stimulation, i.e., those for $t < 0$.

Summarizing our analysis of Figure 4.6, we obtain that short pulse-train stimulation via a single stimulation site induces the reset of the neurons. Thus, the extent of this reset depends on the strength I of applied stimulation. Since the impact of the stimulus depends on the placement of the stimulated neuron, see Eqs. (4.2), the extent of reset is different for the different neurons.

Now we illustrate the impact of coordinated reset stimulation on the Kuramoto system of coupled phase oscillators. In Figure 4.7 three different states of the system of coupled oscillators are shown. Without stimulation system can demonstrate synchronized state for strong coupling (Figure 4.7(A)) or desynchronized state for vanishing coupling (Figure 4.7(B)). The latter state could be a goal state for a desyn-

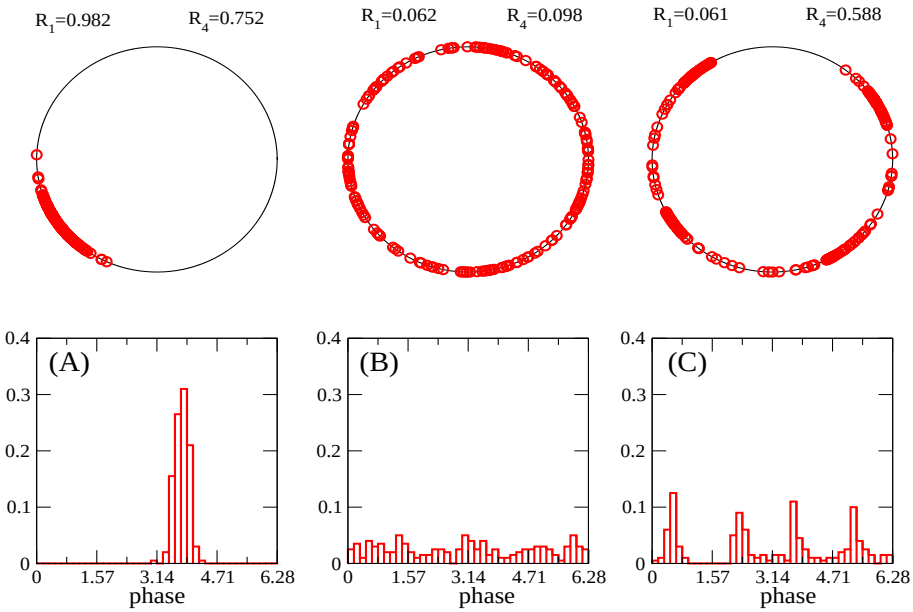

Figure 4.7: Different states of the phase model (4.3). Upper subplots illustrate the system states by points $(x_j, y_j) = (\cos\theta_j, \sin\theta_j)$, $j = \overline{1, N}$ on the unit circle where $\{\theta_j\}$ are the phases of the oscillators. The normalized histograms of the phases $\{\theta_j\}$ on interval $[0, 2\pi)$ are shown on the lower subplots. (A) Synchronized state of the system without stimulation, (B) desynchronized state in the system without coupling. (C) 4-contact CR stimulation induces the 4-cluster state in a model (4.3) of coupled phase oscillators where the stimulation parameters are $I = 10$ and $\sigma = 0.4$.

chronizing stimulation. Coordinated reset stimulation can induce in the stimulated ensemble a so-called clustered state shown in Figure 4.7(C).

We have also shown in Figure 4.7 the corresponding values of order parameters R_1 and R_4 calculated according to Eq. (2.3). Synchronized state is characterized by large values of R_1 and R_4. A desynchronized state is characterized by small values of R_1 and R_4. A four-cluster state is indicated by small R_1 and large R_4 values. We can conclude that CR stimulation indeed can lead to a clustered state for some parameter values. In the following text the effect of such a stimulation under parameter variation is studied in detail.

4.1.3 Averaged state of the model under permanent CR stimulation

In this subsection we will investigate the effect of coordinated reset stimulation for different values of stimulation parameters. The main parameters to be varied are the stimulus strength I and the distribution width σ of the stimulation strength. These parameters were chosen due to the following reasons. Parameter σ characterizes a decay rate of the current spread with the distance from the stimulating contact. In what follows we will use for the parameter σ the term *decay rate*. Its values strongly relate with electrochemical characteristics of the brain tissue, which are neither exactly known nor controlable during the stimulation. Thus, we have to be able to choose the appropriate stimulation for any value of the decay rate σ. On the other hand, the stimulation strength is the most natural parameter of the stimulation to be varried and which effect is quite easily to understand. Now we will consider two-dimensional pictures in the plane (I, σ) allowing us to estimate the stimulation effect.

The order parameter technique will be used to distinguish different types of the stimulation induced states. For each fixed values of parameters (I, σ) we consider a long permanent stimulation lasting for the time $t \in [0,\, 800] = [0, 400T]$. We found that during the stimulation system dynamics approaches a periodic trajectory. We can see examples of such trajectory in Figure 4.8 where the exemplary dynamics of two order parameters for different parameter values is shown. Dashed lines in Figure 4.8 depict the end of periods of stimulation where all four stimulation contacts sequentially administer their stimuli to the tissue.

Since the order parameters undergo quite strong oscillations, we consider $R_{1,4}$ averaged over time (actually, over one period of stimulation) in order to estimate the effect of stimulation. The following Figure 4.9 describes the dependencies of the averaged order parameters $\langle R_1 \rangle$ and $\langle R_4 \rangle$ on the stimulation parameters (I, σ) where blue points correspond to the smaller values of $\langle R_1 \rangle$ and $\langle R_4 \rangle$, and red points correspond to the larger values of the order parameters. We can see perfectly distinguishable orange island in the lower left corner on the picture for R_4 corresponding to the stimulation-induced four-cluster state. Indeed, in this region the values of

$\langle R_1 \rangle$ are small (dark blue) and $\langle R_4 \rangle$ is comparably large (orange).

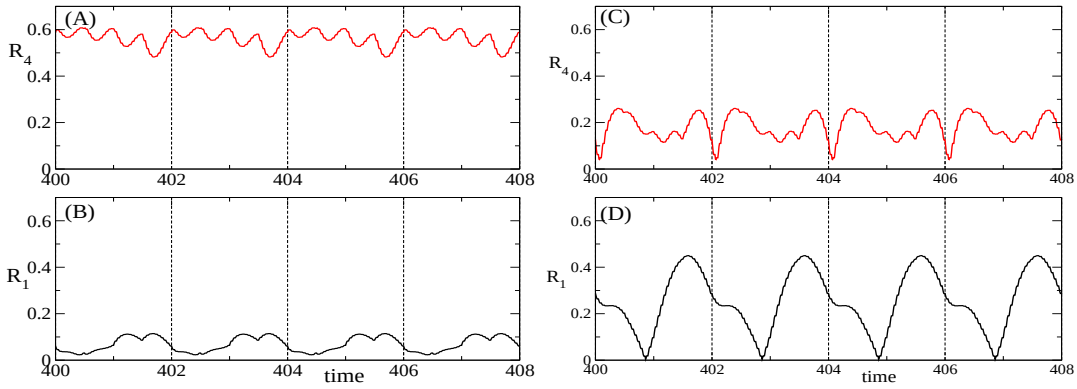

Figure 4.8: Oscillations of the order parameters R_1 and R_4 during 4-contact CR stimulation. Parameter values are (A),(B) $I = 10$, $\sigma = 0.4$, providing clustered state; (C),(D) $I = 7$, $\sigma = 2$, providing state, close to a desynchronized state.

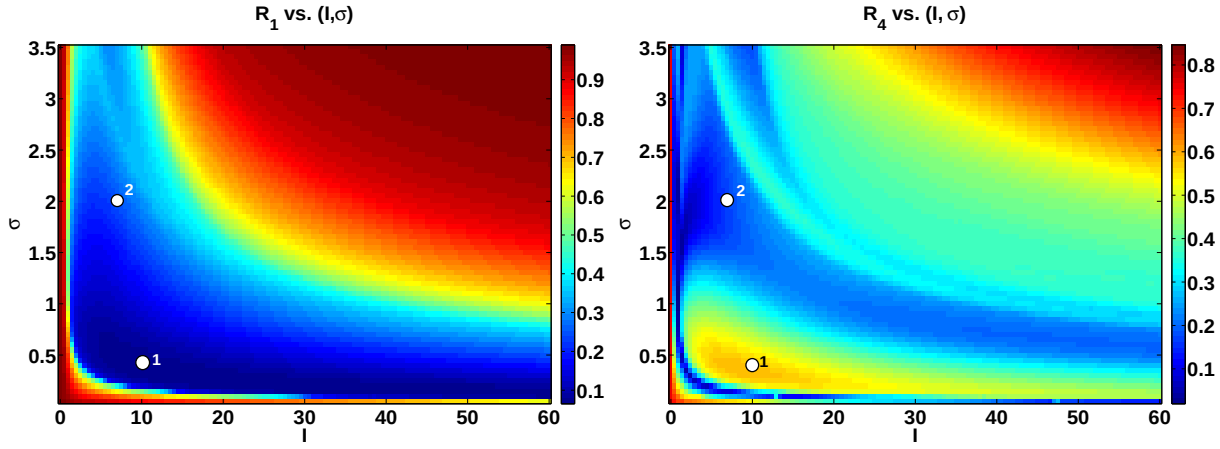

Figure 4.9: The averaged order parameters $\langle R_{1,4} \rangle$ versus the stimulation strength I and the decay rate σ. Depicted points are **1**: $I = 10$, $\sigma = 0.4$, **2**: $I = 7$, $\sigma = 2$. Values of order parameters in point **1**: $R_1 = 0.067$, $R_4 = 0.578$; **2**: $R_1 = 0.245$, $R_4 = 0.167$.

As we can see, the region of small values of $\langle R_1 \rangle$ has a band-like form leading to the conclusion that for the small values of σ a large interval of admissible stimulation

strength can be found. On the other hand, for large values of σ stimulation strength should be small enough if we would like to prevent a suppression of oscillations. Red regions in the right upper corners of both diagrams in Figure 4.9 correspond to the suppressed oscillations caused by strong stimulation and large coefficient of the decay rate σ. Indeed, oscillator phases $\{\theta_j\}$ do not perform full rotation on the unit circle under the corresponding stimulations. Phases fluctuate near the value $\theta = \pi/2$ imposed by the stimulation protocol, see also Figure 4.6. Thus, CR stimulation with these parameters mimics the effect of the HF stimulation since each of N_c stimulating contacts administers reset of the entire neuronal population. This results in large values of the averaged order parameters $\langle R_1 \rangle$ and $\langle R_4 \rangle$. Now we will discuss two different states, which are characterized by small values of the averaged order parameter $\langle R_1 \rangle$ corresponding to points **1, 2** in Figure 4.9.

Point **1**: Coordinated reset stimulation with parameters $I = 10$ and $\sigma = 0.4$ leads to a 4-cluster state. Indeed, this follows from the averaged values of order parameters $\langle R_1 \rangle = 0.067$ and $\langle R_4 \rangle = 0.578$ as well as from the normalized histogram of the system phases shown in Figure 4.10(B) at the end of stimulation period, i.e., at time $t = nT$, $n \in \mathbb{Z}$. There are four prominent peaks in this histogram showing the phase clusters in the model. An interesting fact is the presence of a "gap" in the phase distribution around the point $\theta = \pi/2$. The same effect will be present also for the second parameter point under consideration and will be explained later.

In Figure 4.10(A) the time courses of the order parameters R_1 and R_4 are shown for the case of the above stimulation parameters indicated by point **1** in Figure 4.9. In Figure 4.10(A) we can see a synchronization process to the stable synchronized state for $t \in [0, 100]$ where R_1 and R_4 approach large values. Switching the stimulation on at the moment $t = 200$ induces system clusterization where R_1 decays almost to zero and R_4 oscillates in interval $\approx [0.48, 0.61]$. The enlarged pictures of these oscillations are shown in Figure 4.8(A),(B). After the switching the stimulation off at time $t = 600$ we observe a transient process, which can be roughly subdivided into two phases. The first phase lasting approximately to the time moment $t = 640$ is characterized by the fast decay of the R_4-value, and the system approaches a desynchronized state with small values of both order parameters $R_{1,4}$. After this period we observe the second phase of resynchronization where the order parameters increase to their

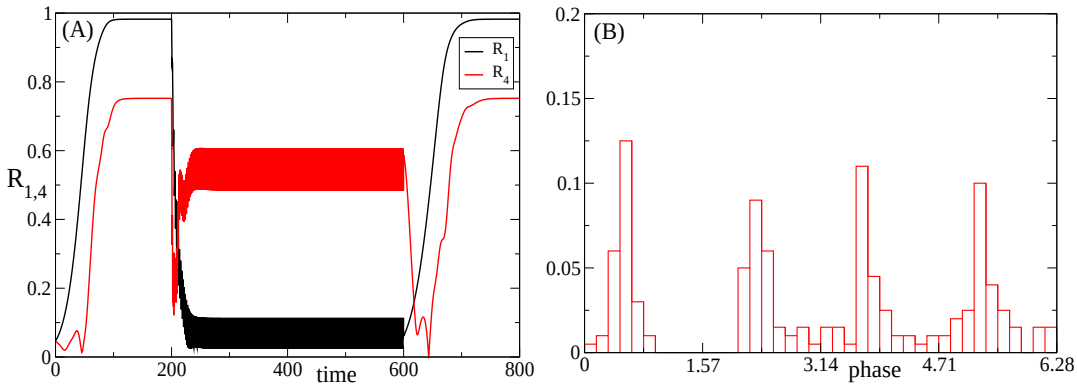

Figure 4.10: (A) Time courses of the order parameters of R_1 and R_4 under CR stimulation for $I = 10$, $\sigma = 0.4$ and the stimulation interval $[t_{\text{begin}}, t_{\text{end}}] = [200, 600]$; (B) 4-cluster phase distribution at the end of the stimulation period.

limit values of the fully synchronized state (time interval $[640, 700]$). More detailed analysis of the post-stimulus transient and its properties will be given in the following subsections. The precise technique of the estimation of a desynchronization in the system, so-called Kuiper index, will be also applied to analyze the transient process in our model (4.3).

Point **2**: The stimulation with parameters $I = 7$ and $\sigma = 2$ does not induce a clustered state, as we have observed in the previous case. This stimulation results in a system state characterized by values of the averaged order parameters $\langle R_1 \rangle = 0.245$ and $\langle R_4 \rangle = 0.167$.

As we can see in Figure 4.11, such stimulation parameters give rise to much larger amplitude of the oscillation of R_1 in comparison with the previous case illustrated in Figure 4.10. The enlarged diagrams for the order parameters for $I = 7$ and $\sigma = 2$ are shown in Figure 4.8(C),(D). As one can conclude from Figure 4.11(B), such stimulation parameters imply a system state similar to the desynchronized state, but with a gap in phase distribution around the value $\theta = \pi/2$. Now we will give the explanation of this fact (the similar phenomenon was mentioned for the previous point **1**).

In Figure 4.12 a snapshot of the phases of all oscillators is shown.

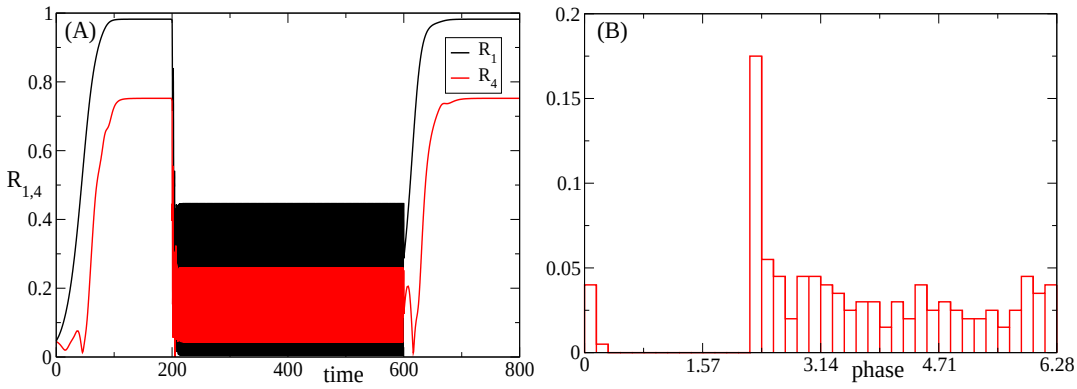

Figure 4.11: (A) Time courses of the order parameters R_1 and R_4 under CR stimulation for $I = 7$, $\sigma = 2$ and the stimulation interval $[t_{\text{begin}}, t_{\text{end}}] = [200, 600]$. (B) Distribution of the system phases (after the whole stimulation cycle), close to a desynchronized state.

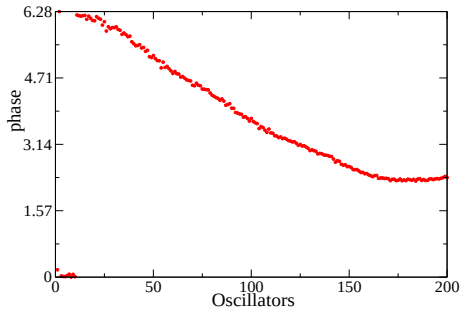

Figure 4.12: Phases of oscillators corresponding to the diagram Figure 4.11(B) versus the number of oscillators at the end of the completed stimulation cycle.

The time moment of the snapshot matches exactly the end of one cycle of CR stimulation. This means that the last stimulating contact was contact 4 coinciding with the oscillator 176, what results in a horizontal "shelf" on this curve for $j \in [150, 200]$ corresponding to the subpopulation around this contact. The gap in the phase distribution in Figure 4.11(B) corresponds to the absence of points in the band $y \in [0.2, 2.2]$ in Figure 4.12. Excepting this interval, all phases demonstrate a continuous curve, which appears due to the comparably large value of $\sigma = 2$. Under this condition each stimulating contact affects neighboring oscillators, attracting

them to the same phase value, see Figure 4.6(B)-(E). This results in such continuous structure of the phase snapshot. On the other hand, the impact of the stimulating contacts 1 and 4 is different from that of the contacts 2 and 3 placed in the inner part of the neuronal ensemble. The former contacts may affect oscillators, which are only on *one* side of the subpopulations surrounding the corresponding contact. The 2nd and 3rd contacts affect neurons, which are situated on *both* sides of the corresponding subpopulations. In other words, there is no impact of the 4th contact on the oscillators surrounding the 1st contact and vice versa. Thus, if we consider again Figure 4.12, the activity of the 4th contact is not able to decrease the gap in the phase values of oscillators from the 1st and 4th subpopulations.

It is supposed by CR stimulation protocol (4.4) that neurons are affected by the stimulation administered via the nearest contact on time interval of length $T/4$ during each stimulation period of length T. Therefore, in the case of the small σ all neurons oscillate without external impact on the time interval of length $3T/4$. Here, the length $3T/4$ corresponds to the entire stimulation cycle without activity of the nearest stimulating contact. For example, the oscillators $1-50$ cannot perform the whole rotation over the unit circle, which takes time T, during the time interval of length $3T/4$. Furthermore, for large values of σ the dynamics of these oscillators is slowed down by the activity of the 2nd and 3rd stimulating contacts. Therefore, these reasons result in a gap in the distribution of the neuronal phases, which is revealed by histograms in Figures 4.10 and 4.11.

4.1.4 Post-stimulus transient dynamics

In this section we study the behavior of a model (4.3) analyzing transient dynamics of the system after switching the stimulus off. In the stimulation-free regime the ensemble returns back to its synchronized state. Understanding the transient dynamics is important due to the practical aspects of the coordinated reset stimulation technique since this stimulation is usually used with periodic rest intervals. This question will be considered in more detail in the next subsection 4.1.6. Such rest intervals allow to decrease the total duration of the stimulation resulting in a milder stimulation technique. We are looking for a longer transient time from the state ob-

tained as a result of stimulation. Such parameter values of the longest transient after the stimulation belong to a set of optimal parameter values, which we investigate in this subsection. Another important question to be studied here is the dynamics of our system during and after the stimulation if the stimulation is stopped before CR stimulation cycle is completed, i.e., at some earlier time moment than the standard protocol.

First of all, we introduce the notion of *transient time* of the system.

Definition: *Transient time* (or, shortly, transient) t_{tr} for model (4.3) is the time after the end of stimulation t_{end}, which it takes for the first order parameter $R_1(t)$ to reach some predefined threshold L_{tr}. If $R_1\left(t_{\mathrm{end}}\right)$ is already larger than L_{tr}, then t_{tr} is set to zero.

Therefore, the following equality holds in the case where post-stimulus value of R_1 is smaller than the threshold value L_{tr}:

$$R_1(t_{\mathrm{end}} + t_{\mathrm{tr}}) = L_{\mathrm{tr}},$$

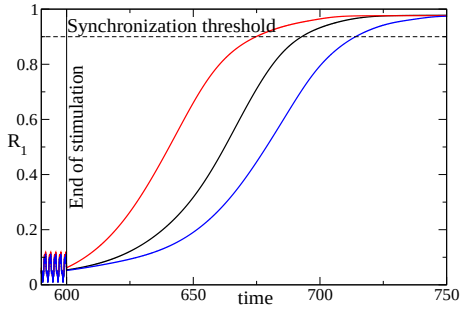

Figure 4.13: Illustration of the transient after switching the stimulation off. Dashed line depicts threshold of resynchronization L_{tr}. Different curves correspond to three different sets of natural frequencies. Stimulation parameters are $t_{\mathrm{end}} = 600$, $N_c = 4$, $I = 10$ and $\sigma = 0.4$.

We illustrate the conception of the transient time in Figure 4.13 where the time courses of the first order parameter $R_1(t)$ are shown after the end of stimulation for three different sets of natural frequencies $\{\omega_j\}_{j=1}^{N}$. The distributions of these frequencies are the same with the mean $\omega_{\mathrm{mean}} = \pi$ and the standard deviation 0.02.

Dashed line shows the resynchronization threshold $L_{\mathrm{tr}} = 0.9$, which will be used also in all further calculations. Note, the value of R_1 in the synchronized state without stimulation depends on the natural frequencies and the coupling strength, and its values are around 0.98. As we can see, during the stimulation $t \in (590, 600)$ is shown in Figure 4.13 the oscillations of R_1 are almost the same for the different sets of natural frequencies. However, the transient times demonstrate significant differences. For example, for the red curve $t_{\mathrm{tr}} \approx 74$, for the black curve $t_{\mathrm{tr}} \approx 92$, and for the blue curve $t_{\mathrm{tr}} \approx 114$.

In all further considerations of the transient time we will use the averaging technique. In order to determine the transient after the stimulation is switched off the large number of different sets of natural frequencies $\{\omega_j\}_{j=1}^{N}$ will be taken and the obtained transient times are averaged afterwards. We demonstrate this method in the following Figure 4.14 where the transients for different time moments of the stimulation break are shown.

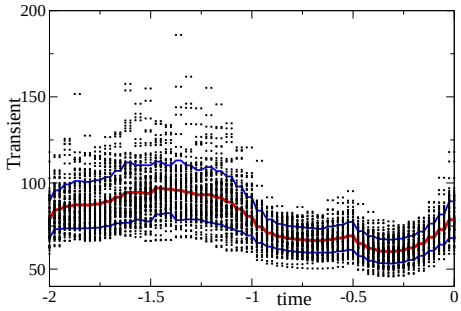

Figure 4.14: Transient time versus the moment of stimulation break ($T = 2$ is one stimulation period). Black points depict transients for single sets of the natural frequencies. The red curve shows averaging over 100 different sets. The blue curves correspond to the averaged value $\pm$ standard deviation. Horizontal axis indicates the time of the stimulation break minus time of the standard end of CR stimulation. Due to the periodic dynamics of the model (4.3) points -2 and 0 are identical. These two points correspond to the standard end of the stimulation. Stimulation parameters are $N_c = 4$, $I = 10$ and $\sigma = 0.4$.

We investigate stimulation cycle in order to find the optimal time to break the

stimulation from the point of view of longer averaged transient. We perform a large number of usual completed cycles of CR stimulation, but the last stimulation cycle can be truncated in some desirable time moment. Therefore, we investigate how the transient time dependes on the moment of time break. Thus, the time interval of length $T = 2$ is studied. The values on the horizontal axis in Figures 4.14 and 4.15 equal the differences between the break time and the moment of the standard end of CR cycle. Therefore, we obtain an interval $[-2, 0]$ where points -2 and 0 correspond to the standard CR stimulation end. We should mention some specific features of the diagram shown in Figure 4.14. The spread of the different transient values is relatively large especially near the point of maximum value of the averaged curve shown by red color, $t \in [-1.75, -1]$. This interval corresponds to the following segment $[T/8, T/2]$ in terms of the stimulation period. On the other hand, we can see a prominent maximal and minimal value of the averaged transient line $t_{\max} = -1.475$ (or $\approx 0.26T$) where the averaged transient equals ≈ 97, and $t_{\min} = -0.3$ (or $0.15T$) with transient time ≈ 60, whereas the result for the usual end of stimulation is $t_{\text{tr}} \approx 79$.

In the following figures we will compare transients for two different points (I, σ) of the stimulation parameters at the points **1, 2** considered above, see Figure 4.9. The objects of the consideration will also be two order parameters, R_1 and R_4. We would like to link together the internal dynamics and state of the system, which are determined by the order parameters and transient time t_{tr} after the stimulation is switched off.

The left part of Figure 4.15 corresponds to the stimulation parameters $I = 10$ and $\sigma = 0.4$ providing a clustered state. The right part of Figure 4.15 corresponds to the parameters $I = 7$ and $\sigma = 2$ implying a state, close to a desynchronized one (see previous subsection 4.1.3). We should mention here that the optimal stimulation break in the sense of the longest transient is close to $T/4$ for the clustered state. On the other hand, for the second (desynchronized) state this optimal time is $\approx 0.41T$. Therefore, for different parameters of stimulation (I, σ) the optimal time of stimulation break can also be different, a detailed picture will be shown later. Another characteristic property of the transient, as we can conclude from Figure 4.15, is a strong relationship between the minimal value of the first order parameter R_1

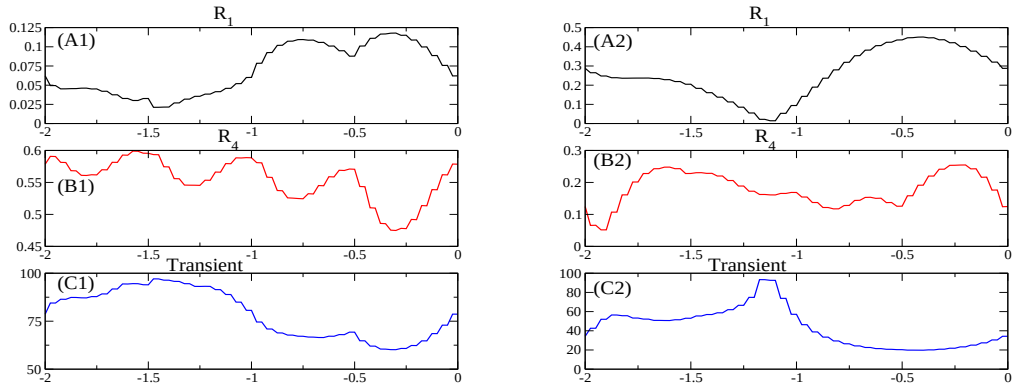

Figure 4.15: Averaged transient time (C) and the order parameters $R_{1,4}$ (A,B) during one stimulation period of the length $T = 2$. Parameters of the stimulation: **1**: $I = 10$ and $\sigma = 0.4$; **2**: $I = 7$ and $\sigma = 2$. Averaging was taken over 100 frequency sets.

and the optimal (maximal) transient time. Thus, for point **1** the minimal value of R_1 is reached at $t = -1.475$ and it coincides with the optimal point for transient. Analogously, for point **2** the minimal value of R_1 is reached at $t = -1.125$ and the optimal moment for transient is $t = -1.175$. This property is observed for almost all parameters of the stimulation. Another important feature is that the optimal transients for these two points are almost equal, but for the clustered state (point **1**) this maximum is not singular where the other breaks of the stimulation demonstrate a relatively long transient. On the other hand, for point **2** there is one narrow peak for the transient, and all other values are very small. For example, the whole diagram for the transient in the clustered case shown in Figure 4.15(C1) lies over the level of $t_{\text{tr}} = 60$. The transient time for the second parameter set shown in Figure 4.15(C2) overcomes this level only in a small region for $t \in [-1.33, -1.03]$.

In Figure 4.16 we can see how the maximal averaged transient time depends on the stimulation parameters. To build these pictures, the large number $N_{\text{set}} = 40$ of different sets of natural frequencies with the same distribution density was taken, and for each frequency vector the transient time is calculated versus the time moment of the stimulation break. Thus, we obtain functions of transient time

$$F^{(i)}_{(I,\sigma)}(t) = t_{\text{tr}},\ t \in [-2,\ 0],$$

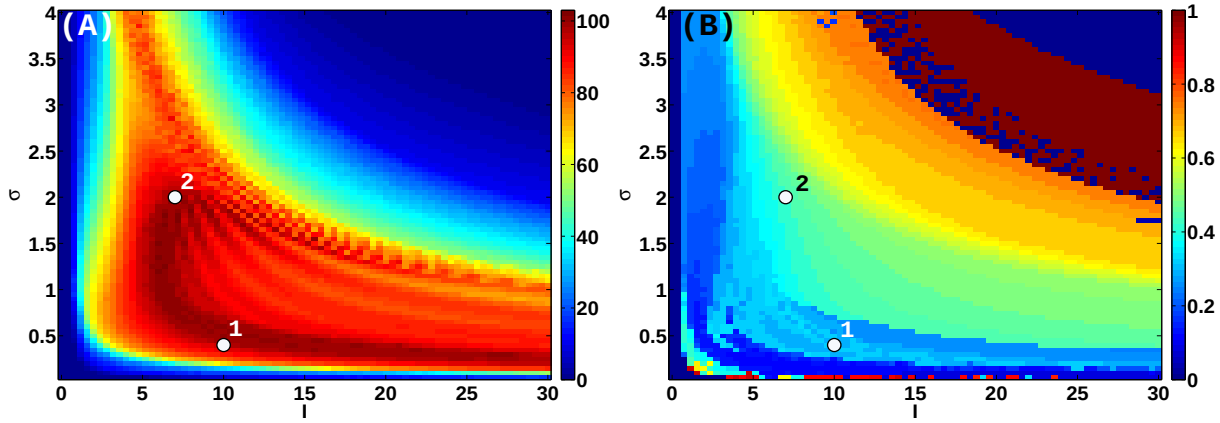

Figure 4.16: (A) Maximal averaged transient time $F_{\max}(I,\,\sigma)$ versus stimulation parameters $(I,\,\sigma)$, see Eq. (4.9). (B) Points of optimal stimulation break as part of the stimulation period $t_{\text{opt}}(I,\,\sigma)$ vs. $(I,\,\sigma)$, see Eq. (4.10). Points **1, 2** correspond to those in Figure 4.9. Number of stimulating contacts $N_c = 4$, period of stimulation $T = 2$.

where index i denotes the number of the set of the natural frequencies in the model (4.3). I is the stimulation strength and σ is the coefficient of decay rate. Variable t corresponds to that from Figure 4.14 and equals the difference between the time moment of the stimulation break and the standard end of CR stimulation, see also Figure 4.15. Afterwards the averaging over all sets of frequencies was done.

$$F_{(I,\sigma)}(t) = \frac{1}{N_{\text{set}}} \sum_{i=1}^{N_{\text{set}}} F^{(i)}_{(I,\sigma)}(t),$$

For each point $(I,\,\sigma)$ we find the maximal value $F_{\max}(I,\,\sigma)$ of the averaged function $F_{(I,\sigma)}(t)$ on interval $t \in [-2,\,0]$, which is reached in the point $t^*_{(I,\sigma)} \in [-2,\,0]$.

$$F_{\max}(I,\,\sigma) = \max_{t\in[-2,\,0]} F_{(I,\sigma)}(t) = F_{(I,\sigma)}(t^*_{(I,\sigma)}). \tag{4.9}$$

$$t_{\text{opt}}(I,\,\sigma) = (t^*_{(I,\sigma)} - (-2))/2. \tag{4.10}$$

The function $F_{\max}(I,\,\sigma)$ is shown in Figure 4.16(A). The time moments of the optimal stimulation break, resulting in the maximal transient, are defined by values $t^*_{(I,\sigma)} \in [-2,\,0]$. Since the stimulation period is $T = 2$, the relative time, i.e., the

part of period where the stimulation is switched on, of the optimal stimulation break is given by Eq. (4.10), $t_{\text{opt}}(I, \sigma) \in [0, 1]$.

One can see that region of the maximal transients (dark red) mostly corresponds to the parameters (I, σ) providing strongly clustered state (see Figure 4.9). On the other hand, there is a region in Figure 4.16(A) where the maximal transient is large, but the corresponding post-stimulus system state is far from being clustered as compared to the system state at point **1**. Point **2** belongs exactly to this region where the post-stimulus system state is characterized by the small values of the order parameter R_1 as well as the small values of the order parameter R_4.

The diagram in Figure 4.16(B) also reflects the fact that the optimal time breaks for our points **1, 2** are different. The point **1** lies in the blue region of picture (B) corresponding to the stimulus break close to $0.25T$, whereas **2** belongs to the domain, which can be roughly characterized as having optimal break, close to $0.5T$. In addition, in order to obtain the maximal transient at the parameter point **2** one has to precisely hit an optimal time of the stimulation break, see also Figure 4.15. This indicates a greater sensitivity of CR stimulation to the perturbations at point **2** as compared to the parameter values at point **1**. We should keep in mind that under the real application of CR the value of the decay rate σ is fixed. This corresponds to a horizontal slice in Figure 4.16. Therefore, it is possible to find an optimal value of the stimulation strength I and the time stimulation break, see Figure 4.16(B), providing an effective stimulation with long post-stimulus transient. This corresponds to red and dark red regions in Figure 4.16(A).

The following Figure 4.17 demonstrates the values of the order parameters R_1 and R_4 at the moment of the optimal interruption of the stimulation $t^*_{(I,\sigma)}$, i.e., exactly at the time, which is shown in Figure 4.16(B).

As mentioned above, the most important information, which we can extract from Figure 4.17, is the fact that points **1, 2** are characterized by the similar values of the first order parameter R_1 at the moment of stimulus break, whereas the corresponding values of R_4 are different. This observation also confirms the fact that the maximal transient time is closely related to the minimal value of R_1, which can be achieved during the stimulation. The second conclusion following from Fig-

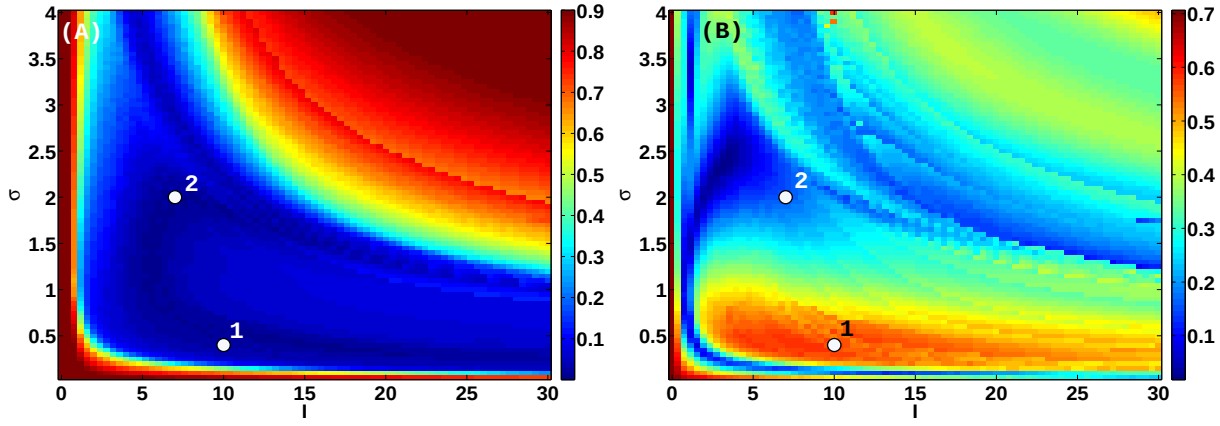

Figure 4.17: The order parameters (A) R_1 and (B) R_4 at the moment of the optimal break of CR stimulation $t^*_{(I,\sigma)}$ (see Figure 4.16(B)).

ure 4.17(A) concerns the values $R_1 > 0.9$, which are shown by dark red. For these parameter values transient time is equal to zero and any analysis of the optimal stimulation break with resynchronization threshold $L_{\rm tr} = 0.9$ cannot be applied.

Now we will compare already obtained results concerning the optimal break of the stimulation with results obtained by applying the standard full cycle of CR stimulation. In terms of Figure 4.15 this means that it is necessary to compare the maximal value of the corresponding curve with the values at points 0, -2. These two points are equivalent due to periodicity of the system and stimulation and correspond to the standard protocol of CR stimulation.

The transient time $t_{\rm tr}$ versus stimulation parameters (I, σ) is shown in Figure 4.18. The scale is the same as in the previous Figure 4.16(A). There are several specific differences between this diagram in Figure 4.18 and the corresponding diagram for the case of the maximal transient shown in Figure 4.16(A). First of all, the value in each point (I, σ) in the case of the standard CR stimulation is smaller than in the maximal case. This is an expected result since some fixed value from the set cannot be larger, than maximal one. The most fascinating feature of the diagram in Figure 4.18 is as follows. As we can see in Figures 4.16 and 4.18, large values in Figure 4.18 (orange points) approximately correspond to the clustered state of our

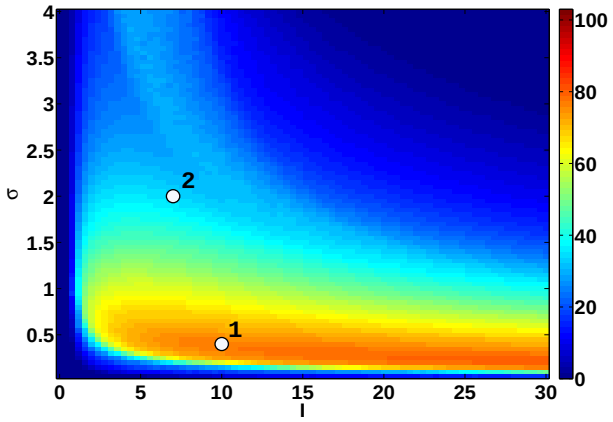

Figure 4.18: Transient time after normal end of CR stimulation where the whole cycle of the stimulation is administered versus stimulation parameters (I, σ).

model, see Figure 4.9. On the other hand, for the case of the optimal stimulation break the same results can be obtained not only in the clustered state, but also for some parameter regions leading to desynchronized state. For the stimulation parameters corresponding to the points **1, 2**, we will see that in the clustered state **1** the difference in transient between the usual and optimal cases is not significant. On the other hand, for the parameters in point **2** the question of the optimal choice of the interruption moment becomes more important.

In order to understand the phenomenon of system desynchronization after the stimulation, we perform the analysis of the system state during its course to the synchronized state. It is well known (see [88]) that, on its way from the clustered state, system undergoes a desynchronization (utilizing the slaving principle [29]). Afterwards a resynchronization starts, which is characterized by increasing of all order parameters ($R_{1\ldots4}$). The estimation of the desynchronization measure of the system phases will be given below.

The measure of desynchronization is so-called *Kuiper index*. It was suggested to use for the system of coupled oscillators in the work [88]. This index is the statistical measure taking its values in interval $[0, 1]$, showing us how close phase distribution is to a fully desynchronized state. The value of Kuiper index 1.0 corresponds to the

state characterized by phases uniformly distributed on interval $[0,\, 2\pi)$, whereas the zero value of Kuiper index indicates the state, which is far from being uniformly distributed on $[0,\, 2\pi]$.

Kuiper index Here we present an algorithm of numerical calculation of the Kuiper index. The details can be found in work [88]. The Kuiper test is a modification of the standard Kolmogorov-Smirnov test (KS test) for the case of the circular data. We briefly present the algorithm of the calculation of the Kolmogorov-Smirnov (KS) index.

Suppose, we have data sample of length l: $\theta_1, \ldots, \theta_l \in [0,\, 1]$. Let us denote by $G(\theta)$ the cumulative distribution function corresponding to the sample $\{\theta_j\}$. Then we can write the maximal distance between two cumulative distribution functions: empiric function $G(\theta)$ and the function, which is given by the uniform distribution $P(\theta) = \theta$.

$$D = \max_{0\le\theta\le 1} |G(\theta) - \theta| \,,$$

and the probability to reject the **true** hypothesis about the uniform distribution of $\{\theta_j\}$ reads

$$P_{\mathrm{KS}}(d) = 2\sum_{j=1}^{\infty} (-1)^{j-1} \exp\left(-2j^2 d^2\right),$$

$$d = D \cdot \left(\sqrt{\frac{l}{2}} + 0.12 + 0.11\sqrt{\frac{2}{l}}\right).$$

In order to perform the Kuiper test we have to use the following value V instead of D

$$V = D^+ + D^- \text{ where}$$

$$D^+ = \max_{0\le\theta\le 1} (G(\theta) - \theta),\ D^- = \max_{0\le\theta\le 1} (\theta - G(\theta)),$$

Now we will analyze the evolution of the Kuiper index (KI) after the switching stimulation off. In Figure 4.19 the different time courses of the KI are shown for the different sets of the natural frequencies $\{\omega_i\}$ for parameters $I = 10$ and $\sigma = 0.4$ given by point **1** in Figure 4.16. The stimulus break is chosen to be optimal, see Figure 4.15.

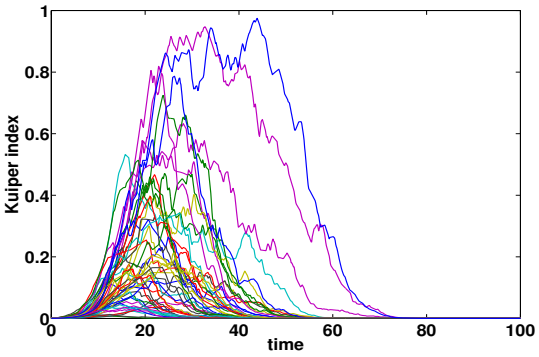

Figure 4.19: Examples of time courses of Kuiper index (50 trials). Zero corresponds to the begin of the post-stimulus transient. Stimulation parameters are $I = 10$, $\sigma = 0.4$ and $t_{\text{break}} = 0.525$ after the last entire cycle of CR stimulation.

The main conclusion following from Figure 4.19 is a significant dependence of the Kuiper index on the set of the natural frequencies. Therefore, to perform any further analysis, it will be necessary to make an averaging over a large number of frequency vectors. In what follows we will take 100 trials. We can also see that each trial demonstrates increasing from value close to zero imposed by the stimulation protocol and afterwards Kuiper index decays indicating the resynchronization.

The next Figure 4.20 reveals the averaged over 100 trials evolutions of the Kuiper index for the parameter set given by point **1** providing the prominent 4-cluster state during the stimulation. We consider three cases of stimulation the break. The first case is the optimal break with the longest transient time, the second case corresponds to the usual end of CR stimulation and the third case is the break, which is characterized by the shortest transient.

The structure of all curves in Figure 4.20 is the same. There exists one prominent peak with further decay of the index to zero. We can see that the optimal choice of the stimulus break allows us to achieve much better desynchronization during the post-stimulus transient.

In order to compare effects of the stimulation for the different values of parameters, we consider similar pictures for point **2** for parameters $I = 7$ and $\sigma = 2$. Analo-

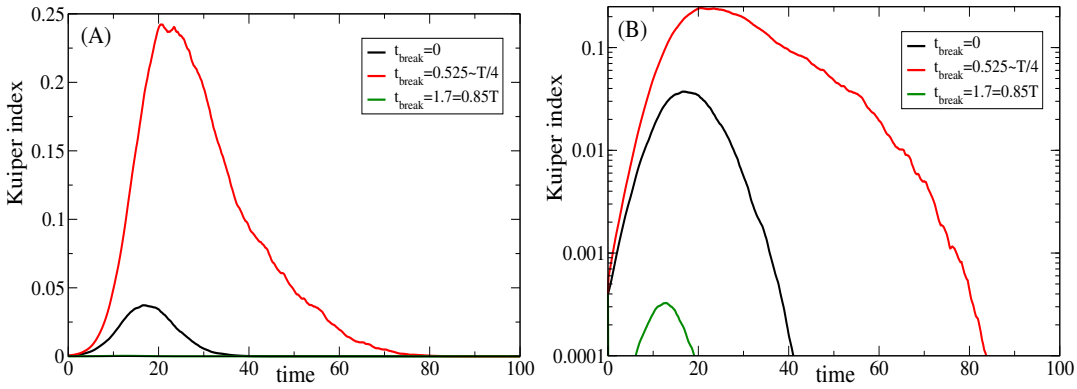

Figure 4.20: The averaged over 100 trials Kuiper indices for three different cases of the stimulation break. The red curve depicts the optimal stimulation break, the black curve corresponds to the usual end of stimulation (the entire cycle of CR stimulation) and the green curve depicts the worst from the point of view of transient break. (A) Linear scales for both axes, (B) linear scale for the horizontal axis and logarithmic scale for the vertical axis. Stimulation parameters are $I = 10$ and $\sigma = 0.4$ implying clustered state.

gously, we consider the time course of the averaged Kuiper indices for the optimal stimulation break and for the usual one.

In Figure 4.21 one can see that the optimal stimulation break implies much better (larger) maximum value of the Kuiper index than the usual end of CR stimulation. Comparing Figure 4.21 with the previous Figure 4.20 we can see that clusterizing stimulation provides much better approach to the desynchronized state during the post-stimulus transient. Indeed, the maximal value of the averaged KI achieved after the optimal break of the stimulation with parameters $I = 10$ and $\sigma = 0.4$, i.e., implying a clustered state, is 0.242. On the other hand, the maximal value of KI reached after the optimal stimulation break for the case of $I = 7$ and $\sigma = 2$ is only 0.052. Therefore, we can conclude that CR stimulation imposing a clustered state is better from the point of view of post-stimulus desynchronization than CR stimulation leading to the state close to desynchronized. We should also mention that for the clustered state the ratio of maximal value of KI for the optimal break to the usual one is approximately 6.5, whereas for the second stimulation this ratio

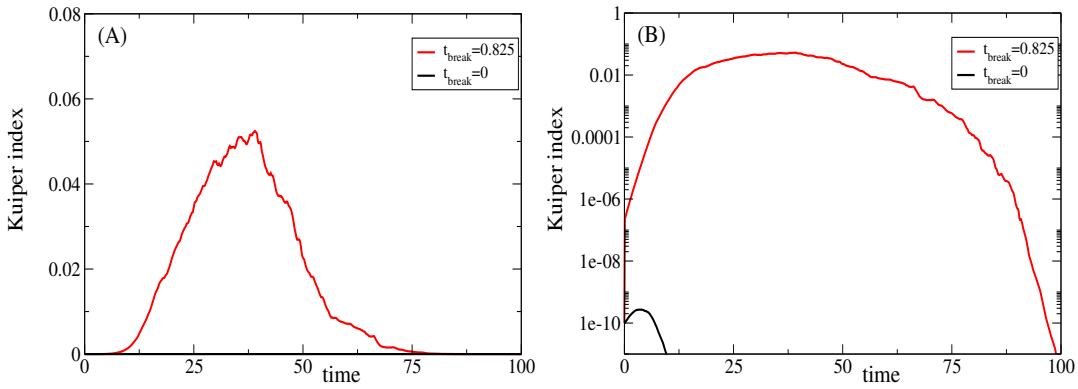

Figure 4.21: Averaged over 100 trials Kuiper indices for two different cases of stimulation break. The red curve depicts the optimal case and the black curve depicts the case of the usual end of stimulation (the entire CR cycle). (A) Diagram with linear scales, (B) linear scale for the horizontal axis and logarithmic scale for the vertical axis. Stimulation parameters are $I = 7$ and $\sigma = 2$ implying desynchronized state.

has order of 10^{-8}. We can again conclude that in the case of clusterizing stimulation the difference between the optimal and usual break of stimulation is much smaller, than in the case of stimulation imposing state close to desynchronized (point **2**).

We have considered in subsections 4.1.3 and 4.1.4 CR stimulation effects for the stimulation period T, which is equal to the natural period of the system of phase oscillators (4.3). In the following subsection 4.1.5 we study CR stimulation where the detuning between the natural system frequency and stimulation frequency is present.

4.1.5 Effect of frequency mismatch on CR stimulation

We investigate how robust the effect of CR stimulation is with respect to the detuning between the natural mean frequency of the system and the frequency of the CR stimulation. This question is very important from the practical point of view since the small difference between the frequency of the brain LFP and the stimulation frequency can exist, e.g., due to the small fluctuations of the LFP frequency. Another

aspect of the varying CR period is the following: if several different frequency peaks are present in the spectrum of the system, then it is necessary to understand the behavior of the model in the situation where the frequency detuning is large. This case we will study under the following restriction. We suppose that the stimulation period is a multiple of the internal period of the model (4.3).

The case of small detuning between the frequencies of the system and stimulation. Here we consider the case where the periods of the system and external stimulation do not differ too much. In the following Figure 4.22 we can see the averaged order parameters for the system under the stimulation with parameters $I = 10$ and $\sigma = 0.4$, see point **1** in Figure 4.9. The period of the ensemble is fixed to 2.

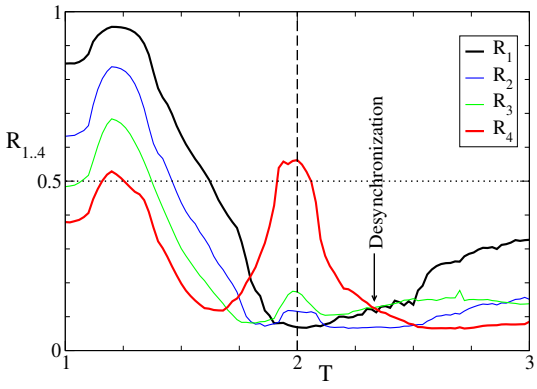

Figure 4.22: The averaged values of the order parameters $R_1, \ldots, R_4$ versus period of CR stimulation. Other parameters of stimulation are $N_c = 4$, $I = 10$ and $\sigma = 0.4$.

As follows from Figure 4.22, the minimal value of the averaged first order parameter $\langle R_1 \rangle$ is imposed by CR stimulation with period T, which coincides with the period of natural oscillations of the model. The natural period of the model equals 2.0 and is shown in Figure 4.22 by a vertical dashed line. As it has been already shown in Figure 4.9 in subsection 4.1.3, the mentioned stimulation parameters $I = 10$ and $\sigma = 0.4$ imply a 4-cluster state for the stimulation period $T = 2$. Thus, in Figure 4.22 we can see a prominent peak of $\langle R_4 \rangle$ and small values of the averaged order parameters $\langle R_1 \rangle, \langle R_2 \rangle$ and $\langle R_3 \rangle$ in vicinity of the point $T = 2$.

If some detuning is present, then the averaged value of $\langle R_1 \rangle$ increases. The interesting phenomenon is that CR stimulation with $T < 2$ implies larger values of $\langle R_1 \rangle$ than the stimulation with $T \in (2, 3)$. This fact can be explained as follows. If the stimulation period $T < 2$, then the neuronal subpopulations, which are reset by the different contacts, do not have enough time during their unaffected dynamics of length $3T/4$ to unwrap the phases over the entire unit circle. On the other hand, the stimulation period $T > 2$ allows the phases to unwrap on the unit circle. To estimate under which detuning CR stimulation is still effective, we introduce some critical value of the averaged order parameter $\langle R_1 \rangle$, which is not allowed to be crossed. We use the value $\langle R_1 \rangle = 0.5$ according to the work [85]. This value of $\langle R_1 \rangle = 0.5$ is depicted in Figure 4.22 by a dotted horizontal line. We can conclude that even in the case of relatively large period mismatch, which can reach up to 20% of the natural period of the model (4.3), the averaged order parameter $\langle R_1 \rangle$ is smaller than the predefined critical value. CR stimulation protocol is thus quite robust to the small changes of its period.

We should however mention that the change of the stimulation period T could induce changes in the stimulation impact on the neuronal ensemble. As we can see in Figure 4.22 for $T = 2$ a prominent 4-cluster state is induced, which is characterized by large value of $\langle R_4 \rangle$ and small values of the averaged order parameters $\langle R_1 \rangle, \langle R_2 \rangle$ and $\langle R_3 \rangle$, see also Figure 4.10. Figure 4.22 reveals that values of the stimulation period T larger than 2.0 can induce a desynchronized state where the averaged values of the order parameters $\langle R_1 \rangle, \ldots, \langle R_4 \rangle$ are small. This parameter region is depicted in Figure 4.22 by an arrow "Desynchronization". In the next Figure 4.23(A) we illustrate the behavior of the order parameters for the value of $T = 2.33$.

In order to illustrate the desynchronized behavior during such a stimulation, we plot in Figure 4.24 the time course of the Kuiper index for two CR stimulations with the different periods T (scale on vertical axis is logarithmic). The blue curve corresponds to the case $T = 2.33$. It is evident that the values of the Kuiper index for such stimulation are much larger than in the usual case of $T = 2$ shown by the red curve. We can also see that the oscillations of the blue curve are not so regular, as in the case of the standard period $T = 2$ of CR stimulation.

Summarizing our results, we can conclude that CR stimulation has a robust effect

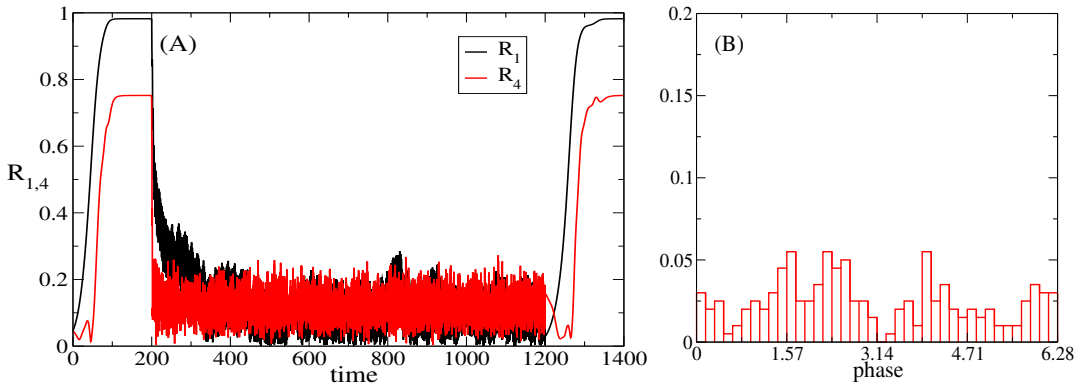

Figure 4.23: Coordinated reset stimulation with $T = 2.33$. (A) Time course of the order parameters R_1 and R_4. (B) Normalized histogram of phases for the time moment $t = 500$. Stimulation interval is $[t_{\text{begin}}, t_{\text{end}}] = [200, 1200]$.

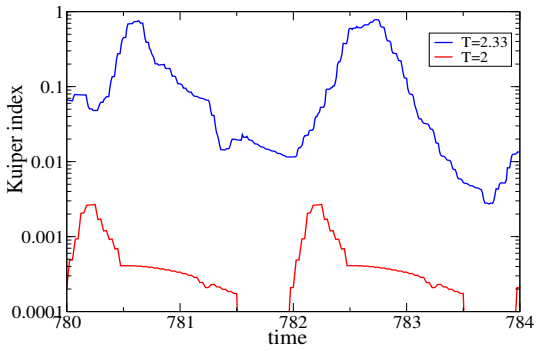

Figure 4.24: Time courses of the Kuiper indices during CR stimulations with the different stimulation periods. The blue curve correspons to $T = 2.33$, the red curve corresponds to $T = 2$. Stimulation parameters are $I = 10$ and $\sigma = 0.4$.

on the suppression of the first order parameter R_1. Furthermore, increasing of the stimulation period is characterized by a stronger suppression of R_1 than the corresponding decreasing of T. The second interesting phenomenon is that the changes of T can induce different states in the stimulated neuronal ensemble. We can observe clustered and desynchronized states for the same values of the stimulation strength I and the decay rate σ.

Large frequency detuning: the case of resonant relations between the natural and stimulation frequencies. Here we consider the situations where the stimulation period is equal to some multiple of the natural period, i.e., the period of the stimulated neuronal ensemble.

$$T = k_p \cdot 2\pi/\omega_{\text{mean}}, \tag{4.11}$$

where $k_p \in \mathbb{N}$ and ω_{mean} is the mean value of the natural frequencies $\{\omega_j\}$.

In the simplest case where the periods of the system and stimulation are equal ($T = 2\pi/\omega_{\text{mean}}$), we have an ideal situation of the clustered state provided the appropriate choice of other stimulation parameters, such as the stimulation strength I and the decay coefficient σ. The number of clusters equals the number of stimulating contacts N_c. It is possible to say that at some moment of time the system phases $\{\theta_j\}$ are located around the following points on the unit circle $\varphi_i = 2\pi i/N_c$, $i = \overline{1, N_c}$, giving us a perfect N_c-cluster state.

The situation becomes much more complicated if we have the stimulation period, which is some multiple of the natural period of our model, i.e., $k_p \geq 2$ in the expression (4.11). Now we can assert that the corresponding points on the unit circle are $\varphi_i = 2\pi k_p i/N_c$, $i = \overline{1, N_c}$. Therefore, it is possible for such stimulation that some of these N_c points coincide.

$$\text{There exist } i_1 \text{ and } i_2 \in [1,\ N_c]: \quad 2\pi k_p i_1/N_c \equiv 2\pi k_p i_2/N_c \ (\text{mod. } 2\pi)\,,$$

or, simplifying this expression,

$$\text{there exist } \ i_1 \text{ and } i_2 \in [1,\ N_c]: \quad k_p\,(i_1 - i_2) \equiv 0\,(\text{mod. } N_c)\,. \tag{4.12}$$

The necessary condition for statement (4.12) is the following: $(k_p,\ N_c) > 1$. The braces here denote *the greatest common divisor*, i.e., the largest integer number, which is a common divisor of two integer numbers in braces. This condition means that numbers k_p and N_c are not coprimes. The number of *different* points φ_i, i.e., the number of clusters under CR stimulation, equals

$$N_{\text{clusters}} = \frac{N_c}{(N_c,\ k_p)}. \tag{4.13}$$

One can see that formula (4.13) also holds for the case of the standard stimulation, i.e., $k_p = 1$ implies $N_{\text{clusters}} = N_c$. If k_p and N_c are coprimes expression (4.13) also holds, i.e., $(N_c, k_p) = 1$ implies $N_{\text{clusters}} = N_c$. The important corollary from (4.13) is the following, if $k_p = N_c$, then the denominator of the ratio is equal to N_c and the result value $N_{\text{clusters}} = 1$. This means that such CR stimulation does not have clusterizing effect and implies synchronization.

Now we will demonstrate the above effects by the simulations of our model (4.3) with the following periods of stimulation $T = 4$ ($k_p = 2$), $T = 6$ ($k_p = 3$) and $T = 8$ ($k_p = 4$) in Figure 4.25. Note that the natural period of the stimulated ensemble is 2. The diagram (A) in Figure 4.25 corresponds to the stimulation period $T = 4$ providing the evident 2-cluster state, which we can conclude from the histogram as well as from the analysis of the averaged order parameters. Indeed, the largest order parameter is R_2, values of R_1 and R_3 are small, the value of R_4 is comparably large.

The plots (B) and (C) in Figure 4.25 are built for the fixed number of HF-pulses $N_p = 10$ in the pulse train for each stimulating contact, see formula (4.4), p. 73, instead of using the total "filling" of the time interval, corresponding to the contact, by the pulses, which is given by (4.5). The case of $N_p = 10$ pulses corresponds to the stimulations with $T = 2$, $N_c = 4$. This number $N_p = 10$ of HF pulse is sufficient to perform the reset of the subpopulation of oscillators.

In Figure 4.25(B) we can see the result of CR stimulation with $T = 6$. This state is close to the 4-cluster as indicated by the values of the order parameters where R_4 is large and the values of the other considered order parameters are small. The plot (C) reveals a 1-cluster (fully synchronized) state, which is obtained under CR stimulation with $T = 8$.

We can conclude that CR stimulation with the stimulation period being a multiple of the natural period of the stimulated system induces a clusterization in the system. The number of the stimulation-induced clusters can range from 1 cluster corresponding to the stimulation-induced synchronization up to the number of stimulating sites N_c clusters.

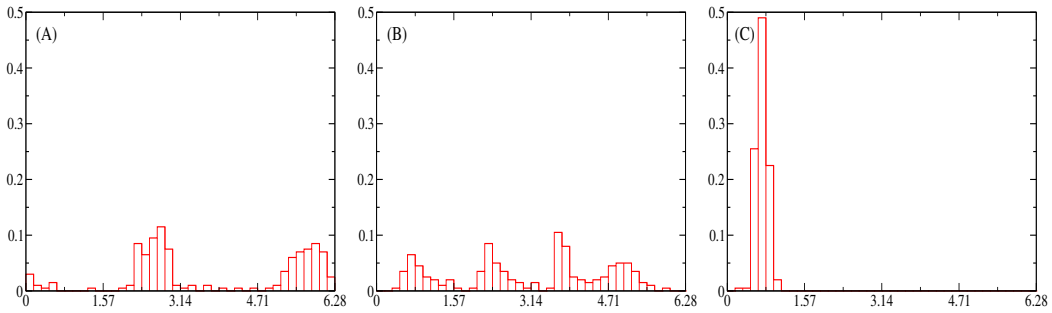

Figure 4.25: Normalized histograms for the system phases on interval $[0, 2\pi)$ for the following values of the stimulation period. (A) $T = 4$, 2-cluster state, the averaged values of the order parameters during the stimulation are $(R_1, R_2, R_3, R_4) = (0.11, 0.72, 0.23, 0.33)$. (B) $T = 6$, state, close to the 4-cluster one, the averaged values of R_i during the stimulation are $(R_1, R_2, R_3, R_4) = (0.16, 0.15, 0.17, 0.44)$. (C) $T = 8$, 1-cluster (synchronized) state, the averaged values of R_i are $(R_1, R_2, R_3, R_4) = (0.99, 0.98, 0.95, 0.90)$.

4.1.6 On-Off stimulation

In this subsection we investigate the dynamics of the Kuramoto system of phase oscillators (4.3) with one specific type of CR stimulation corresponding to the real application of this novel stimulation technique to deep brain stimulation. Thus, we study CR stimulation protocol including pauses between series of stimulation cycles. The presence of pauses in the stimulation protocol allows to decrease the impact of the administered stimulation on the brain tissue. This technique also utilizes the slaving principle, see also [29], where the system after the stimulation is switched off approaches a desynchronized state before resynchronization starts. We will use the term "on-off CR stimulation" for this intermittent technique. Below we give the definition of this stimulation protocol.

Definition: $m : n$ *on-off* or *intermittent CR stimulation* protocol defines periodic stimulation with period $(m + n)T$. Consider one period of the mentioned length, the first part of the period with length $T_{\text{active}} = mT$ determines the interval where the standard CR stimulation with period T is applied. The second part of period with length $T_{\text{rest}} = nT$ gives the interval without stimulation.

Thus, $m : n$ on-off stimulation protocol implies the intermittent intervals of length mT where CR stimulation with period T is applied and rest intervals of length nT without stimulation. In what follows, we will use the value of $T = 2\pi/\omega_{\text{mean}} = 2$, i.e., equal to the natural period of the system. In the above definition the numbers m and n can be positive real numbers. The main goal of this study is to consider dependence of the $m : n$ on-off stimulation effect on the numbers m and n. The notion of effect of such a stimulation is based on the values of the first order parameter and will be explained in detail later. In order to investigate the impact of the lengths of stimulation and rest intervals, which are given by m and n, we fix other parameters of CR stimulation. For further simulations we will use the values of the stimulation strength I and the decay rate σ corresponding to the point **1** from Figure 4.9 with $I = 10$ and $\sigma = 0.4$. This parameter values imply strong clusterization in our model under CR stimulation, which has been analyzed above.

The following Figure 4.26 demonstrates exemplary functions of the contact activities in the case of 4-contact $3.5 : 1.5$ stimulation. Functions, corresponding to different contacts, i.e., $\text{Ind}_i(t)$, $i = \overline{1,4}$, see Eqs. (4.3), (4.4), are shown by different colors. The length of the complete cycle of the intermittent CR stimulation is $(3.5+1.5)\cdot 2 = 10$ where the rest interval has duration $1.5 \cdot 2 = 3$. As it is shown in Figure 4.26, the active intervals are [0, 7] and [10, 17] and the rest intervals are [7, 10] and [17, 20]. The diagram also demonstrates the important property of the on-off stimulation if m is not integer. We can see that the last cycle of CR stimulations between dotted and dashed lines is incomplete since its length is smaller than one period of CR stimulation. In this way the investigation performed in the previous subsection 4.1.4 devoted to the optimal stimulation break is also useful for the case of the on-off stimulation.

We divide the investigation of the $m : n$ on-off CR stimulation into the following steps: first of all, the on-off stimulation with the integer values of m and n will be considered; afterwards, we investigate the behavior of the system in the case of integer m and real n, and only after that the most complicated case of both real m and n can be studied.

We briefly introduce the criterion of the quality of the on-off stimulation based on the values of the order parameter R_1. We consider typical time courses of R_1, which

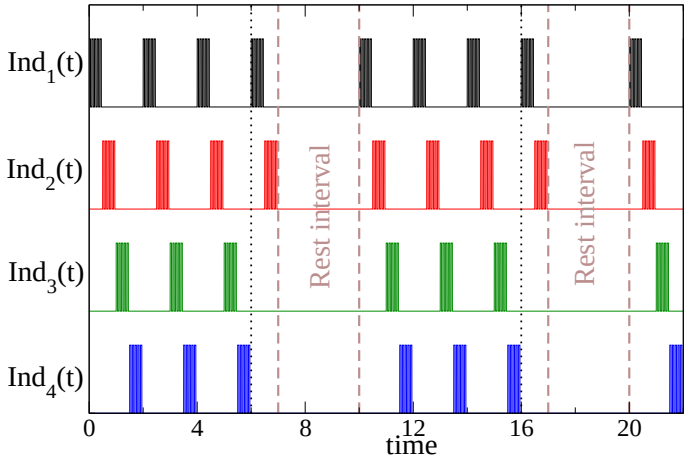

Figure 4.26: Schematic example of the stimulation signals for the 4-contact on-off 3.5 : 1.5 CR stimulation protocol. Brown dashed lines separate the stimulation and rest intervals.

are shown in Figure 4.27 for the on-off 2 : 3 and 2.5 : 3 stimulations. In the case of 2 : 3 stimulation its period $5T$ is a multiple of the natural system period T. Then the dynamics of R_1 is periodic with period $5T$, see Figure 4.27(A). The order parameter R_1 reaches its maximal value at the end of each rest period, which are marked by the red circles. Due to periodicity all these values are the same. In the case of 2.5 : 3 stimulation dynamics of the system is much more complicated. Thus, the maximal values of the order parameter R_1 reached during the rest periods are different as illustrated in Figure 4.27(B).

Thus, we can introduce the maximal values of R_1 during the rest periods

$$r_k = \max_{t \in I_k} \left(R_1(t) \right), \tag{4.14}$$

where I_k is the kth rest interval, $I_k = [(m+n)kT - nT, (m+n)kT]$, $k \geq 1$. As a characterizing quantity we consider the mean value of a large number N_{int} of r_k, $k = \overline{1, N_{\text{int}}}$.

$$r = \frac{1}{N_{\text{int}}} \sum_{k=1}^{N_{\text{int}}} r_k. \tag{4.15}$$

In our consideration the number of intervals will be $N_{\text{int}} = 400$. The behavior of the system in terms of the quantity r will be now described for the case of integer

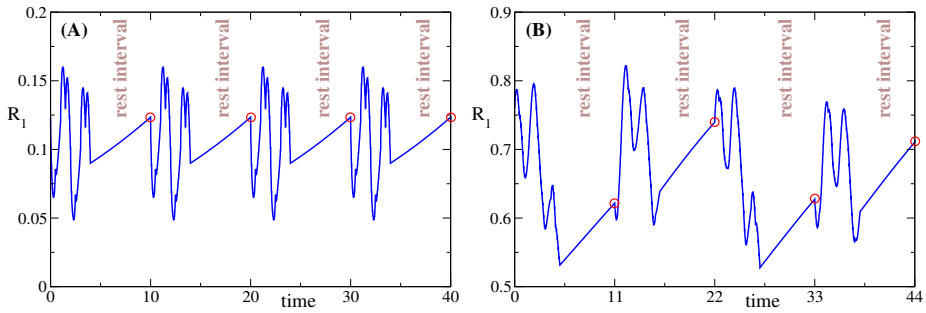

Figure 4.27: Time courses of R_1 during the on-off CR stimulation. (A) $2:3$ on-off stimulation and (B) $2.5:3$ stimulation. Red circles depict the maximal values of R_1 on each rest interval, which coincide with the values of R_1 at end points of rest intervals.

m and n values. In Figure 4.28 the values of r are encoded by color and depicted versus the numbers $(m,\, n) \in [1..30]^2$.

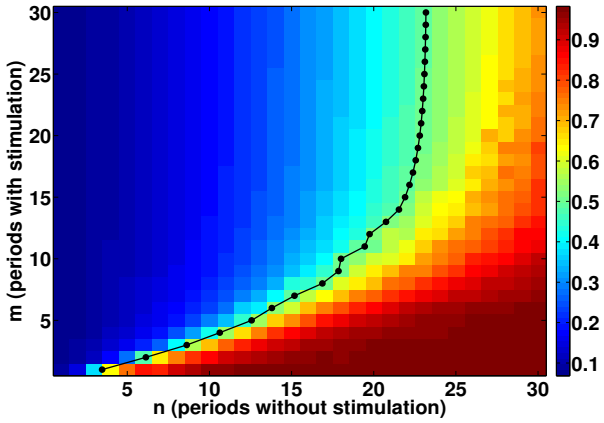

Figure 4.28: Quality of the on-off stimulation r versus integer $(m,\, n)$ values, see Eq. (4.15). Black line depicts delimiting level of $r = 0.5$.

We mention several important properties of the on-off CR stimulation with integer $(m,\, n)$ values. First of all, if the number of active periods m (vertical axis) is fixed and the number of the rest periods n increases, then there is an evident growing of r up to the maximal value of R_1 for the synchronized state without stimulation, i.e.,

approximately 0.98. As follows, with increasing of the rest interval the system has enough time to complete the transient after the switching stimulus off and returns to the fully synchronized state characterized by large value of the order parameter R_1. The second property is much more interesting and important and reflects the fundamental feature of the system. We consider some level of r delimiting the "desired" (small values of r) and "undesired" (large values of r) states of the system. In the work [85] the chosen level was 0.5. The corresponding curve is shown as black line in Figure 4.28. We can see that for large values of m this curve as a function $n(m)$ becomes constant. Indeed, if m is large, e.g., $m > 30$, then even larger m, i.e., even longer stimulation does not bring any changes to the post-stimulus transient dynamics of the system. System is already set to the same clustered state and then it takes the same time for R_1 to reach any predefined level, e.g., $R_1 = 0.5$, after the switching the stimulation off. To illustrate this property, we plot in Figure 4.29 the time courses of R_1 for the different on-off stimulations with the same values of $n = 25$ and different values of m. We consider large values of $m = 30$ and $m = 45$. The time courses of the order parameter R_1 during the on-off CR stimulation with the above parameters are depicted in Figure 4.29(A) for $m = 30$ and Figure 4.29(B) for $m = 45$. As we can see, even increasing in 1.5 times the length of the stimulation subinterval in on-off stimulation does not give any positive effect. After the post-stimulus transient the order parameter R_1 reaches the same maximal value irrespectively of the length of the stimulation.

Now we describe the dynamics of the model in the case of non-integer values of m and n. In the following Figure 4.30 the values of r as functions of real $n \in [1, 9]$ for two fixed values of $m = 5$ and $m = 8$ are shown by red curves.

Figure 4.30 illustrates several important conclusions. First of all, the periodic structure of the graph $R_1(t)$ is present only for intervals of n near the integer values where the standard deviation equals to zero where the blue curves coincide with the red curve. We can also see that these windows of periodicity become more and more narrow under increasing of n, e.g., in Figure 4.30(B) this window around the point $n = 2$ has length ≈ 0.3, whereas the corresponding window around $n = 8$ has length ≈ 0.17. We can also mention that between the windows of periodic behavior around the integer values of n there are significant peaks of r characterized by large

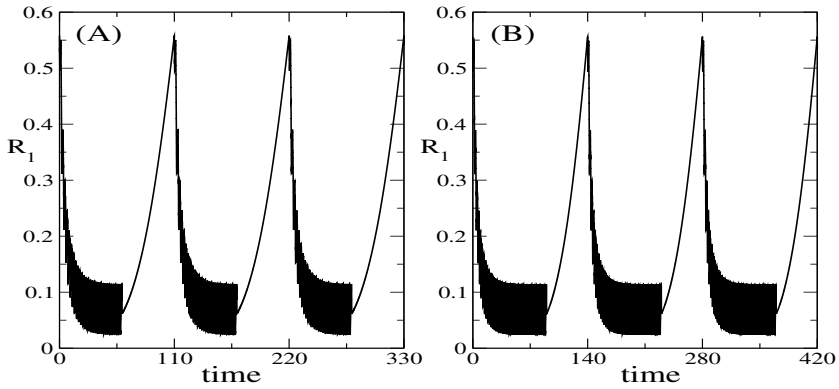

Figure 4.29: Time courses of the order parameter R_1 for two different on-off CR stimulations. Stimulation parameters are (A) $30 : 25$ and (B) $45 : 25$.

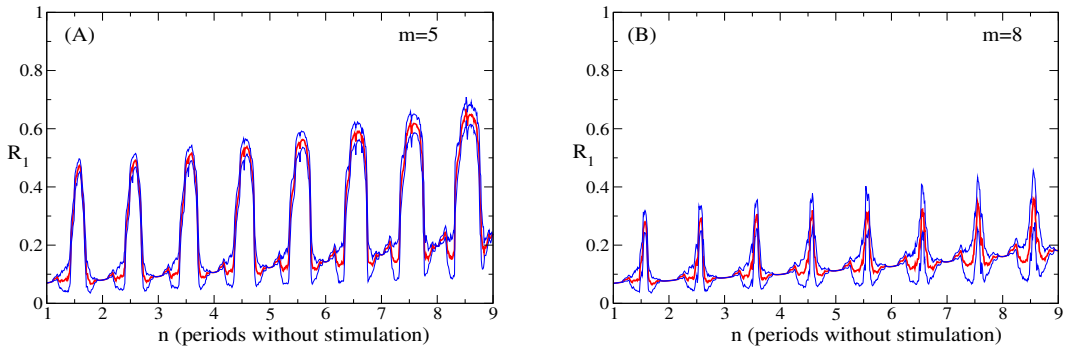

Figure 4.30: Values r as functions of real n determining the length of the rest interval in the $m : n$ on-off CR stimulation are shown by the red curves. Values $r \pm$ std.dev $\{r_k\}$ versus n are depicted by the blue curves. The length of the stimulation interval is given by the values of (A) $m = 5$ and (B) $m = 8$.

standard deviation. We can conclude that these intervals between periodic windows are undesirable from the point of view of DBS implementation of on-off $m : n$ CR stimulation, because the stimulation admits large values of the order parameter indicating strong synchronization in the neuronal population. The peak heights increase with increasing n. Another peculiar feature of these diagrams is that for larger m ($m = 8$) the heights and widths of the peaks of the graphs of the quantity r are significantly smaller than those for smaller m ($m = 5$).

All these facts can be explained by a resonance between the original system with period T and the external force (stimulation) with period $(m+n)T$. If we consider integer values of m, there is a resonant behavior near the integer values of n where the dynamics of the system perturbed by an external force is periodic, i.e., is locked by this force. The periodic dynamics results in zero values of the standard deviation of r_k values since all rest intervals contribute the same values r_k, see Eq. (4.14). The strength of the external force is determined by relation between m and n values. Increasing of m value keeping n fixed results in the larger strength of the external force since the relative part of the stimulation subinterval increases. On the contrary, increasing n for the fixed value of m corresponds to the decay of the external strength. Therefore, larger value of m provides larger sizes of resonant windows. This phenomenon is similar to the resonant Arnold tongues with increasing width as external strength increases. The opposite effect takes place if we increase duration of the rest subinterval (determined by n) and the windows of periodicity shrink.

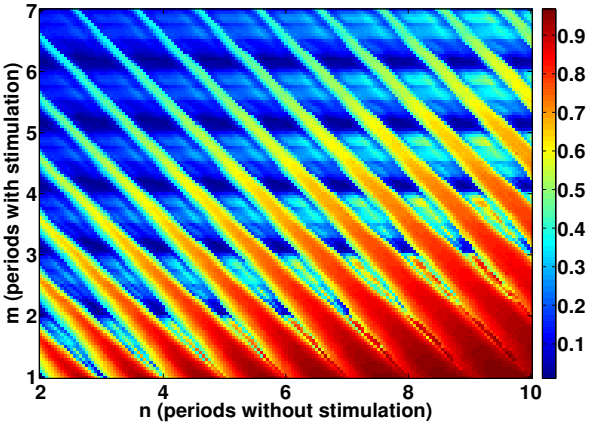

Figure 4.31: Quality r of the on-off CR stimulation given by Eq. (4.15) versus real values of $(m,\, n) \in [1,\, 7] \times [2,\, 10]$. Other parameters of stimulation are $I = 10$ and $\sigma = 0.4$.

We present a general picture for arbitrary positive real values of m and n, which is shown in Figure 4.31. We can see an extremely complicated structure, which can be explained as superimposing of a few different effects. The most prominent detail in Figure 4.31 is the presence of red diagonal tongues, which are situated

approximately along the lines $m + n = P + 0.5$, $P \in \mathbb{Z}$. They correspond to the peaks in Figure 4.30 and can be explained as strongly non-resonant cases of system dynamics. Similarly, the bands between them (which lie along the lines $m + n = P$, $P \in \mathbb{Z}$) demonstrate better effect of the stimulation, i.e., smaller r, due to the resonance between the extrernal stimulation and the oscillatory system. In the latter case period of the external force is a multiple of the system period. Furthermore, we can see in Figure 4.31 the horizontal dark blue lines reflecting the effect of CR stimulation with an appropriate choose of the stimulation break moment. These lines are situated above the "integer" lines $m \in \mathbb{N}$ matching with the corresponding result from the previous subsections. Indeed, one may compare the discussed effects with those from subsection 4.1.4 devoted to the transient analysis for the parameter point **1** where the optimal break of the stimulation has been found to closely approximate the point $T/4$.

We also note the change of the width of the red non-resonant tongues. These tongues are narrow for larger m and/or smaller n, similarly to the pictures in Figure 4.30. As mentioned above, the reason of it is the resonance where the sizes of resonant windows depend on the external force, which is given by relative length of the active subinterval in one cycle of the on-off CR stimulation.

To link together results from Figures 4.31 and 4.28, we can recall that results from the previous less general diagram 4.28 coincide with the separate points of an integer grid in the general picture 4.31. Summarizing results of the mentioned diagrams, we can describe the diagram of r versus real (m, n). The right lower corner, i.e., with small m and large n values, is characterized by large values of r and is dark red. There are red tongues originating from this region and stretching to the left upper corner, which become more and more narrow for smaller n/larger m. Furthermore, there exist dark blue horizontal lines situated approximately at the values of $m = k + 0.25$, $k \geq 2$, $k \in \mathbb{Z}$.

In the present section 4.1 we have considered an impact of CR stimulation on the neuronal population modelled by the Kuramoto system of phase oscillators. The effect of the stimulation has been estimated utilizing different techniques. The main attention was paid to the problem of the optimal values of different stimulation parameters. In the following section 4.2 we consider a network of the FitzHugh-

Nagumo neurons demonstrating tonically spiking behavior under CR stimulation.

4.2 Coordinated Reset of the system of the FitzHugh-Nagumo neurons

In this section we investigate the behavior of the system of tonically spiking FitzHugh-Nagumo oscillators under the impact of CR stimulation. The main goal is to consider different effects of the stimulation revealed for the phase model (see section 4.1) for the case of more complicated neuronal model involving amplitude dynamics and different time scales characteristic for real neurons. The study of a spiking FitzHugh-Nagumo (FHN) model contributes to the realistic modelling of the neuronal dynamics under CR stimulation. First of all, we describe this model and its well-known features in subsection 4.2.1. The system of coupled FitzHugh-Nagumo oscillators under CR stimulation and its basic properties will be investigated in subsection 4.2.2.

4.2.1 The FitzHugh-Nagumo model

The FitzHugh-Nagumo model is one of the modifications of the Van der Pol nonlinear oscillator [96] describing relaxation oscillations in electrical circuits. This famous relaxation oscillator is often used to describe behavior of biological systems, e.g., cardiac activity [97]. Our main object of interest, which is often called BVP model (Bonhoeffer-van der Pol model), was presented in the work [23]. This model can demonstrate several types of neural activity: silent excitatory neuron, which can have several rest states, and tonically spiking neuron.

The classical FitzHugh-Nagumo neuronal model is described by two ordinary differential equations for the state variables v and w

$$\begin{aligned} \dot{v} &= v - \tfrac{1}{3}v^3 - w + I, \\ \dot{w} &= \varepsilon\left(v + a - bw\right), \end{aligned} \tag{4.16}$$

where ε is a small parameter, a and b are the model parameters, I is an external current. The standard values of these parameters given in the original article [23]

are $a = 0.7$, $b = 0.8$ and $\varepsilon = 0.08$. In the present thesis we will use the above mentioned values of a and b. The used values of I and ε will be discussed below.

As in the case of the phase model, we suppose that all individual oscillators (neurons) have different frequencies (firing rates), which are distributed according to a Gaussian distribution density. In order to incorporate this property into a model (4.16), we consider a network of coupled neurons having slightly different values of parameter. This is possible to perform in different ways, because the frequency of oscillations of system (4.16) depends on all its parameters. As we will demonstrate later, dependence of the spiking rate on the value of the small parameter ε is (under some approximation) almost linear making this parameter quite convenient to determine the frequency of each individual neuron.

To understand the dynamics of system (4.16), we find its fixed points given by the following conditions: $\dot{v} = 0$, $\dot{w} = 0$. The equations of the corresponding nullclines in the plane (v, w), i.e., curves providing the zero values of the derivatives, are

$$\begin{aligned} \dot{v} = 0 \quad &\Rightarrow \quad w = v - \tfrac{1}{3}v^3 + I, \\ \dot{w} = 0 \quad &\Rightarrow \quad w = (v + a)/b. \end{aligned} \tag{4.17}$$

These nullclines are shown in Figure 4.32 depicted by black and red curves.

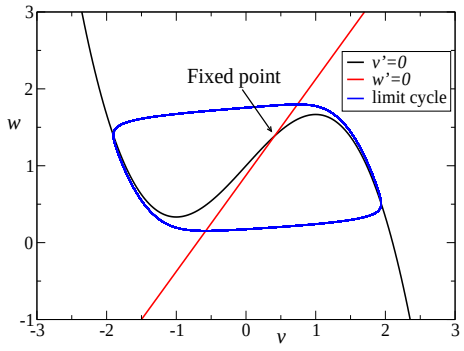

Figure 4.32: State space of the FitzHugh-Nagumo model with parameters $a = 0.7$, $b = 0.8$, $I = 1$ and $\varepsilon = 0.08$. Red and black lines are nullclines (4.17) of the system. Blue curve indicates a stable limit cycle of the model.

The intersection of two nullclines gives a fixed point (equilibrium) of the system, which is indicated in Figure 4.32. To determine the stability of this fixed point, we

should consider a linearized system (4.16) in the vicinity of the analyzed solution. We consider the parameter values $a = 0.7$ and $b = 0.8$ providing a single fixed point for a system (4.16). The following Figure 4.33 describes the bifurcation structure of a system (4.16) if the value of I varies.

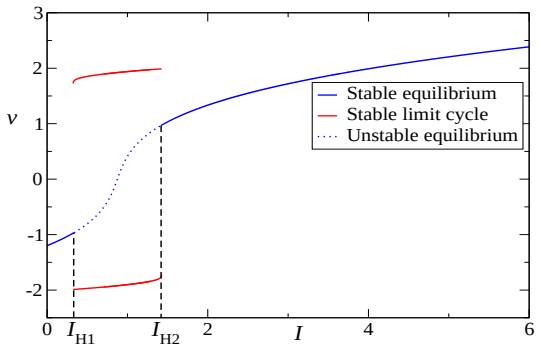

Figure 4.33: System dynamics under the variation of the external current I. The minimal and maximal values of the variable v of system (4.16) are shown versus parameter I. Other parameters are $a = 0.7$, $b = 0.8$ and $\varepsilon = 0.08$. Blue curves indicate stable fixed points, red curves indicate stable limit cycle. Dotted blue line depict unstable fixed points.

We can see in Figure 4.33 the minimal and maximal values of $v(t)$ of the dynamical states for each fixed value I. At the fixed point the minimum and maximum of v coincide with each other giving a single point for each value of I (blue curves). On the other hand, a limit cycle in the plane (v, w) guarantees the presence of at least *two* different point for the corresponding values of I. A stable limit cycles is shown in Figure 4.33 by a pair of red points, depicting the interval of oscillations of the variable v. There are small parameter intervals of multistability where two attractors, the fixed point and the limit cycle, are present in the system for the same parameter values, which is difficult to resolve in Figure 4.33. The equilibrium loses its stability at the points I_{H1} and I_{H2} via subcritical Hopf bifurcations. The corresponding unstable fixed point is depicted by the dotted blue curve.

For our simulations we need the spiking behavior of the FitzHugh-Nagumo oscillator. For this we will take for all our further considerations the value $I = 1$ implying an oscillatory state of the neurons.

Another important conclusion, which can be drawn from the analysis of Figure 4.33 is that, applying a short and strong enough stimulus, i.e., increasing value of I, we can shift the system dynamics from the stable limit cycle to the stable equilibrium. This means that external stimulation can result in a system *reset* providing a stereotypical response of the system on the stimulus. In other words, the system state after such a stimulation being a fixed point does not depend on the system state before stimulation. The same behavior we have observed in the case of phase oscillators, see section 4.1. Therefore, we are able to perform an effective CR stimulation of the model of the FitzHugh-Nagumo oscillators since effect of CR stimulation is based on a neuronal reset.

Now we consider the dependence of the frequency of oscillations (firing rate) on the value of small parameter ε. The corresponding diagram is shown in Figure 4.34.

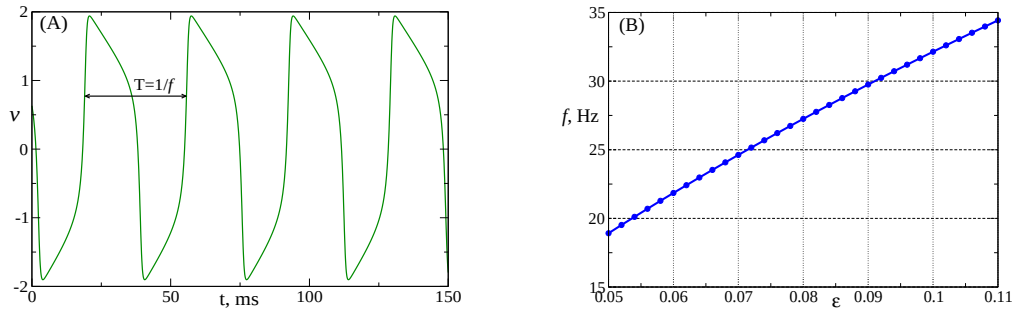

Figure 4.34: (A) Oscillating trajectory $v(t)$ of the system (4.16) with $\varepsilon = 0.08$. $T = 1/f$ is the period of oscillations where f is a frequency of oscillations. (B) Frequency of FHN oscillating model (4.16) vs. small parameter ε (time unit in the system is supposed to be equal to 1 ms). Parameters are $a = 0.7$, $b = 0.8$ and $I = 1$.

As we can see in Figure 4.34(B), the dependence of frequency of the oscillations on the parameter ε is almost linear. This allows to consider an ensemble of neurons oscillating with slightly different frequencies by simply varying ε value for each neuron keeping all other parameters the same for all oscillators.

4.2.2 FitzHugh-Nagumo neurons under CR stimulation: model description

We introduce the model, which we will investigate in order to understand the effect of CR stimulation on the system of neuronal oscillators. We suppose that the spatial structure of our model is the same as in the case of the coupled phase oscillators, see Figure 4.2, p. 70. Thus, all oscillators are arranged on a line segment of the length $L = 10$ having coordinates $\left\{x_j,\, j = \overline{1, N}\right\}$. We also consider $N_c = 4$ stimulating sites with coordinates $\left\{c_i,\, i = \overline{1,\, N_c}\right\}$. Each of N FitzHugh-Nagumo neurons is described by the following differential equations based on system (4.16).

$$\begin{aligned} \dot{v}_j &= v_j - \tfrac{1}{3}v_j^3 - w_j + I + I_{\text{syn}} + I_{\text{stim}}, \\ \dot{w}_j &= \varepsilon_j \left(v_j + a - b w_j\right), \qquad\qquad j = \overline{1, N}, \\ \dot{s}_j &= \alpha H(v_j)(1 - s_j) - \beta s_j, \end{aligned} \tag{4.18}$$

where $a = 0.7$, $b = 0.8$ and $I = 1$, these values have been already discussed above. ε_j give us the frequencies of individual uncoupled oscillators, see Figure 4.34. In our simulations the values of ε_j are distributed according to the Gaussian probability density with the mean value $\varepsilon_{\text{mean}} = 0.08$ and the standard deviation $\varepsilon_\sigma = 0.002$. The synaptic input I_{syn} from other neurons can be written in the following way with the use of the approach from Eq. (1.4), p. 13.

$$I_{\text{syn}} = \frac{K}{N}\left(V_{\text{syn}} - v_j\right) \sum_{\substack{k=1 \\ k \neq j}}^{N} s_k. \tag{4.19}$$

Here, K is the coupling strength, which is divided by N in order to provide a stability of the results with respect to the different number of cells in our model. V_{syn} is a reversal potential determining the type of synaptic connection. We consider the case of excitatory synapses. Then V_{syn} should be larger than the dynamical values of $v_j(t)$. In all further simulations we will use the value $V_{\text{syn}} = 2$. $s_j \in [0,\, 1]$ are the indicator variables of each cell reflecting the appearance of each spike. As follows from Eq. (4.18), if $v_j < 0$, then the corresponding $s_j \to 0$, otherwise, s_j attains some positive value smaller than 1.0. The physiological meaning of the variable $s_j(t)$ is the *postsynaptic* conductance generated by the presynaptic membrane potential $v_j(t)$. $H(v_j)$ is a smooth approximation of the Heaviside function: $H(v) = 1.0/\left[1 + \exp\left(-\lambda x\right)\right]$ where $\lambda = 10$.

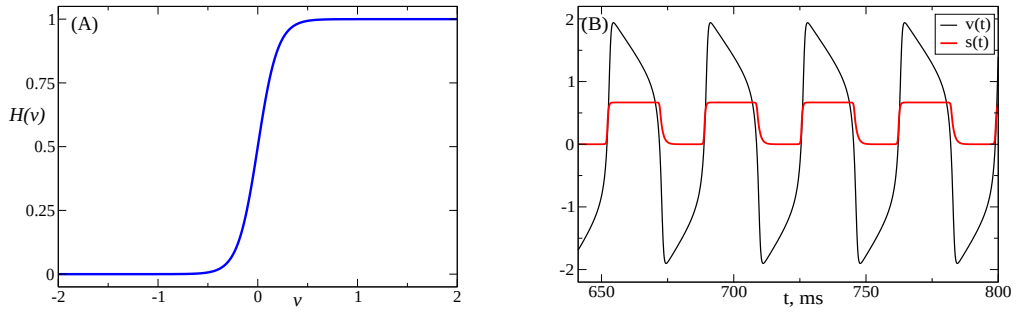

Figure 4.35: (A) Smoothed Heaviside function $H(v)$ for $\lambda = 10$. (B) Exemplary time course of the FitzHugh-Nagumo model represented by variable v (black curve) and the corresponding trajectory $s(t)$ (red curve), generated by the neuron. Parameters are $\alpha = 2$, $\beta = 1$ and $\varepsilon = 0.08$.

We can see in Figure 4.35 the function $H(v)$ (part (A) of the Figure) and trajectories of $v(t)$ and $s(t)$ (part (B)). The spikes of $s(t)$ almost coincide with those of $v(t)$, which is supported by the comparably large values of α and β. In what follows we will use the same values of α, β as in Figure 4.35. This type of synapse is called the *fast* synapse characterized by the values of α and *beta* of order $O(1)$. The *slow* synapse has α of order $O(1)$ and β of order $O(\varepsilon)$ [93]. The height of s-spike is mostly determined by the α and β values and is close to $\alpha/(\alpha+\beta)$, see Eq. 4.18.

The external stimulation current I_{stim} can be written similarly to the expression (4.2), p. 71

$$I_{\text{stim}} = \sum_{i=1}^{N_c} I_i(t) D\left(x_j,\, c_i\right), \tag{4.20}$$

where $I_i(t)$ characterizes the strength and switching time of the stimulation via the ith contact, and $D(x_j,\, c_i)$ reflects the decay coefficient of the stimulation strength in the neuronal tissue with the distance to the stimulation site.

Recalling the expression (4.4) for the functions $I_i(t)$, we should note that the basic pattern of the contact activity is a HF pulse train with pulse period T_p. In the case of phase model, see section 4.1, we have used the value $T_p = 0.05$, which is equal to $1/40$ of the oscillation period $T = 2$ of the synchronized system. As we have already mentioned in Figure 4.34 for the neuronal frequencies, the periods of the oscillations

of individual neurons are close to 40.0, which corresponds to the frequency 25 Hz. In order to preserve the same ratio of the period of HF pulses to the period of system oscillations, we will take the value of $T_p = 1$. The relative length of a single stimulation pulse, which is determined by parameter δ, see Eq. (4.4), is taken to be the same, as in the case of phase oscillators $\delta = 0.5$.

4.2.3 Estimation of CR stimulation effect

In this subsection we investigate the impact of CR stimulation on the system of the FitzHugh-Nagumo neurons (4.18). We will use two different techniques to perform such analysis. The first technique is the method of the phase-based **order parameter** and the second approach is the **mean field** analysis. We give a short description of these methods.

Method of the order parameter This technique is based on the idea to build a phase representation for each individual FHN oscillator, i.e., to calculate the phases $\left\{\theta_j(t),\, j = \overline{1,N}\right\}$ for each individual neuron. There are different methods to reconstruct the phase of a given signal [59, 92], such as method of Hilbert transform or event-related method. We will use the latter method due to its simplicity. The algorithm of the phase reconstruction is the following. For an oscillatory trajectory a sequence of characteristic events is defined such that each event corresponds to the onset of single oscillation of the system. Taking into account the typical form of the trajectory of membrane potential $v(t)$, see Figure 4.35(B), we can consider the appearance of v-spikes as such events. Therefore, we take as events the time points $\{t_k : k \geq 0\}$ of the intersection of the threshold line $v = 0$ by the increasing trajectory $v(t)$. Then the phase $\theta(t)$ can be written on the interval $[t_k, t_{k+1}]$ in the following way

$$\theta(t) = 2\pi k + 2\pi \frac{t - t_k}{t_{k+1} - t_k},\ t \in [t_k,\, t_{k+1}]. \tag{4.21}$$

Therefore, $\theta(t)$ is a piecewise linear function increasing on 2π per each oscillation of the system trajectory $v(t)$. We illustrate the dynamics of the phase in Figure 4.36(A).

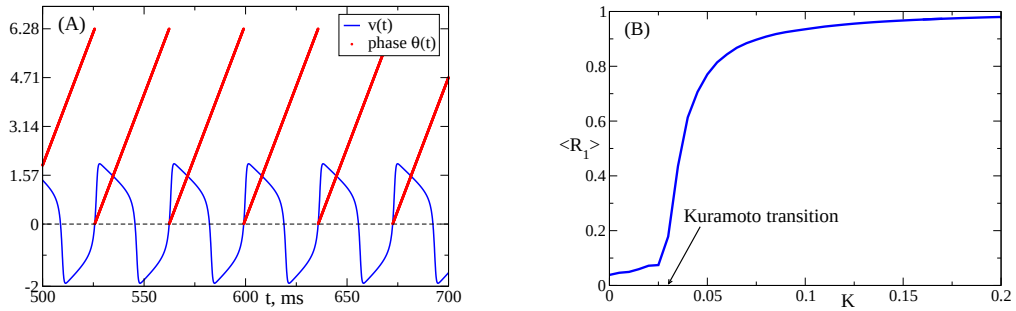

Figure 4.36: (A) Illustration of the phase reconstruction for the trajectory of FHN neuron with parameters $\varepsilon = 0.08$, $a = 0.7$, $b = 0.8$ and $I = 1$. The membrane potential $v(t)$ is depicted by blue curve and the phase $\theta(t) \bmod 2\pi$ is shown by red curve. (B) Kuramoto transition for the system of $N = 500$ FHN oscillators. The blue curve corresponds to the values of the phase-based averaged order parameter $\langle R_1 \rangle$ versus the coupling strength K.

If the trajectory $v_j(t)$ does not intersect the threshold level $v = 0$, we set the corresponding phase $\theta(t) \equiv 0$ (silent neuron). After the introduction of the phases for the FitzHugh-Nagumo neurons, we can calculate the values of the order parameters $R_m(t)$ based on the vector of N phases $\theta_j(t)$, see Eq. (2.3). The behavior of the first order parameter R_1 versus the coupling strength K is similar to that in the case of the system of coupled phase oscillators. The course of the Kuramoto transition from desynchronized state to the synchronized state as the coupling strength K increases is shown in Figure 4.36(B) for the system of FHN oscillators. We can observe a similar dynamics of R_1 to that of the Kuramoto model shown in Figure 2.2(B), p. 22. Based on the results shown in Figure 2.2(B), for all further simulations we will take the value $K = 0.11$, which leads to a synchronized state in the model with the value of the first order parameter $R_1 \approx 0.952$.

Mean field analysis This method is based on the analysis of the mean value of all membrane potentials $v_j(t)$ in the system:

$$V(t) = \frac{1}{N} \sum_{j=1}^{N} v_j(t). \tag{4.22}$$

This variable has a physiological meaning as the local field potential (LFP) of neuronal activity. This signal is usually measured and analyzed in practical applications for example, via a deeply implanted macroelectrode used for deep brain stimulation.

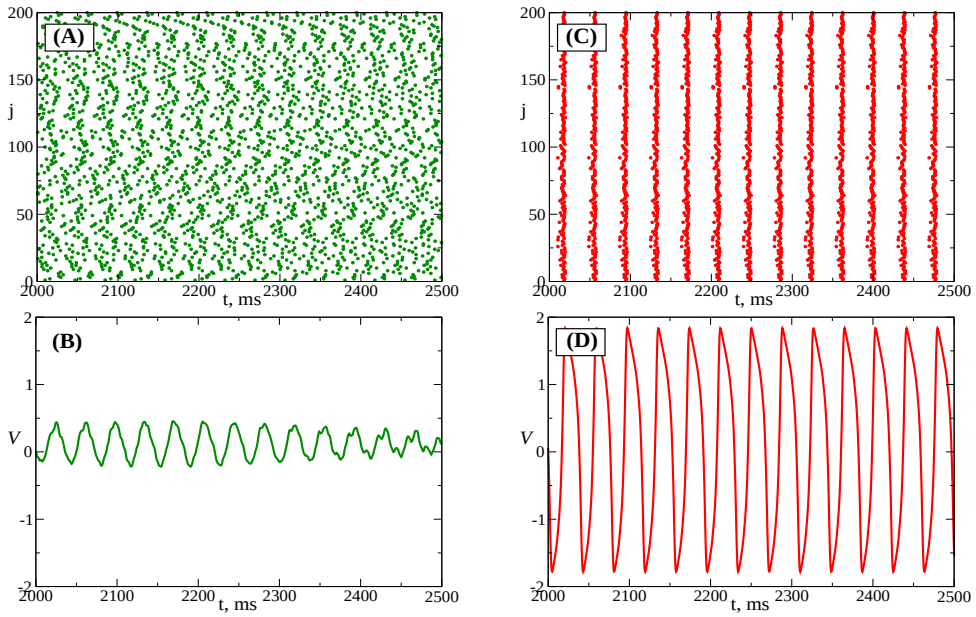

Figure 4.37: Subplots (A) and (C) reveal events (spikes) of the FHN neurons in the model in desynchronized ($K = 0.01$) and synchronized ($K = 0.11$) states, respectively. Point with coordinates (t, j) indicates that neuron j in the moment t produces a spike. Subplots (B) and (D) reveal time courses of the mean fields $V(t)$ in desynchronized (B) and synchronized (D) states.

Diagrams (A) and (C) in Figure 4.37 show the space-time dynamics of the ensemble of coupled neurons (4.18) without stimulation for different coupling strengths. In the desynchronized case shown in Figure 4.37(A) the points form some irregular structure. On the other hand, in the synchronized case shown in Figure 4.37(C) there are clearly distinguishable vertical lines indicating that all cells produce spikes almost simultaneously, which indicates a strong neuronal synchronization. In Figure 4.37(B),(D) we can see the corresponding trajectories of the mean field $V(t)$ in the case of desynchronized ($K = 0.01$, subplot (B)) and synchronized ($K = 0.11$, subplot (D)) system (4.18). As follows the desynchronized state is characterized

by much smaller amplitude of the oscillations of $V(t)$. This characteristic property of the mean field can be used to estimate the effect of CR stimulation from the point of view of depression of unwanted pathologically strong synchronized activity in the system. Therefore, our goal is to minimize the oscillations of $V(t)$, what corresponds to the real DBS application decreasing strongly synchronized activity in certain frequency bands of the LFP signal. In order to estimate the strength of LFP oscillations, we will calculate the standard deviation of the signal $V(t)$.

$$S_V \stackrel{\text{def}}{=} \sqrt{\mathbb{E}\left(V(t) - \mathbb{E}V(t)\right)^2} \tag{4.23}$$

where symbol $\mathbb{E}$ denotes mathematical expectation, i.e., the mean value. For example, desynchronized state for $K = 0.01$ implies the value $S_V \approx 0.13$, whereas $S_V \approx 1.28$ for the synchronized state for $K = 0.11$.

Effect of CR stimulation Now we investigate effects of CR stimulation on the FHN neuronal ensemble. The results of numerical simulations are illustrated as 1-D pictures where the time averaged first order parameter R_1 and the standard deviation of the mean field signal S_V will be plotted versus the stimulation strength I for several fixed values of the decay rate σ. We also show the similar pictures for the system of phase oscillators from section 4.1 where more general 2-D picures have been calculated (see Figure 4.9). The 1-D diagrams for the Kuramoto model are just slices from the already built 2-D pictures.

The averaged order parameter R_1 for the case of permanent stimulation is shown in Figure 4.38. Diagram (A) corresponds to system (4.18) based on FitzHugh-Nagumo neuronal model, and diagram (B) reveals the results for the phase model (4.3). We emphasize the common important properties of these diagrams. For small values of σ, e.g., $\sigma = 0.4$, there is a fast decay of $\langle R_1 \rangle$ as the stimulation strength I increases. Afterwards $\langle R_1 \rangle$ *slowly* increases. On the contrary, large values of σ imply fast increasing of $\langle R_1 \rangle$ with increasing I. We can introduce a notion of an *interval of appropriate stimulation strength* providing the values of $\langle R_1 \rangle$ smaller than some predefined threshold level, e.g., $R_1 = 0.5$.

This threshold level is depicted in Figure 4.38 by the horizontal black dashed line. Figure 4.38 reveals that for large values of σ interval of the appropriate stimulation

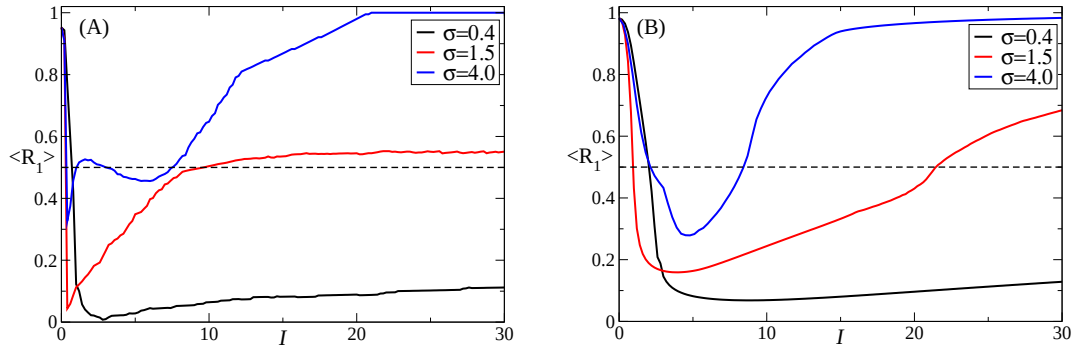

Figure 4.38: The averaged order parameter $\langle R_1 \rangle$ during the permanent CR stimulation versus stimulation strength I for three different values of σ, 0.4, 1.5, and 4.0. (A) System (4.18) of coupled FHN neurons. (B) System (4.3) of coupled phase oscillators.

strength becomes smaller. Therefore, the problem of the choice of the appropriate stimulation strength is more complicated for large σ since the system behavior in terms of $\langle R_1 \rangle$ is more sensitive to the variation of I than in the case of small σ. We can also see in Figure!4.38 that strong enough stimulation can imply oscillation death. Indeed, the blue curve in diagram (A) ($\sigma = 4.0$) achieves the maximal value $\langle R_1 \rangle = 1.0$. Such value corresponds to situation that all neurons in the population become silent. A very strong stimulation reset all neurons such that trajectories of membrane potential $\left\{v_j(t), j = \overline{1, N}\right\}$ stop to oscillate and are kept by stimulation in a region above the predefined threshold value $v = 0$. There is the similar situation in the diagram for coupled phase oscillators Figure 4.38(B). Here, due to the strong stimulation and large value of σ, each stimulating contact has strong impact on the *entire* population. This results in the stereotyped behavior of all oscillators in network where the oscillators die out. Unlike the system of FHN neurons, phase oscillators demonstrate oscillations around the value of $\pi/2$, which is a stable point imposed by the stimulation. Nevertheless, the phase slips, i.e., the rotation of phases over the unit circle, are absent as well as in the case of FHN-based model.

Figure 4.39 reveals the dependence of S_V value introduced by Eq. (4.23) on the stimulation strength I for different values of σ, which are the same as in the previous Figure 4.38. We can see that the general structure of the curves S_V versus I is very

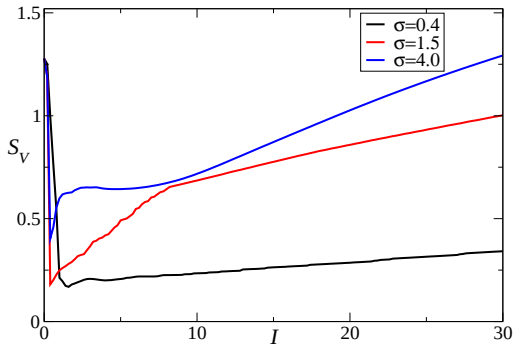

Figure 4.39: Standard deviation of the mean field S_V (4.23) for model (4.18) versus stimulation strength I for three values of σ, 0.4, 1.5, and 4.0.

similar to that for the phase-based order parameter $\langle R_1 \rangle$. The presence of a well-defined minimal value of S_V for the cases of large σ (1.5, 4.0) is evident as well as a slow increase of the variations of the mean field with increasing of I for $\sigma = 0.4$. Since S_V value is closely related to the neuronal activity in the human brain given by the LFP signal of neuronal population, the similar behavior of the estimations of the system state in terms of phase-based order parameter $\langle R_1 \rangle$ and of amplitude-based standard deviation of meanfield S_V is very important for the development and simulations of novel DBS techniques.

4.3 Conclusions

In the present chapter we have studied the effect of CR stimulation on two different models of neuronal population. For the first model (4.3) considered in section 4.1, which is based on the Kuramoto system of coupled oscillators, we revealed the influence of such stimulation parameters as the stimulation strength I, the stimulation period T and the decay rate σ on the effect of stimulation. One of the problems to be solved by the present chapter was to understand the dynamics of the system during CR stimulation. The main goal of the study was to find the optimal parameter values. As estimation measure we have used two different approaches. The first approach is based on the values of the order parameter parameters. As the second

estimation of the CR stimulation quality the length of the post-stimulus transient was taken. We have revealed the influence of the parameters I and σ of CR stimulation on the order parameters and on the post-stimulus transient. The modification of CR stimulation protocol with arbitrary stimulation break and its properties have been also studied. We have also considered the on-off CR stimulation, which is close to the real DBS algorithm, and found an influence of its parameters on the stimulation quality.

For the second model (4.18) based on the system of FitzHugh-Nagumo neurons we have considered two different estimation techniques. The first estimation technique utilized the values of the phase-based order parameter R_1. The second method was based on the mean field analysis. Both methods revealed the system response on CR stimulation similar to the response of the phase model (4.3). Thus, it has been found that different values of the decay rate σ imply different responses of the models on the applied CR stimulation.

Chapter 5

Conclusions

In the present thesis we investigated a number of mathematical models of the pathological synchronization of the human brain activity and methods of its suppression. The considered problems are of great importance within the medical field since many neurological disease, e.g., Parkinson's disease or essential tremor are closely related to the abnormal synchronization in the human brain [9, 57, 60].

We have considered the model of the neuronal network involving spike timing-dependent plasticity in Chapter 2 and two models of the neuronal systems with time-delayed interaction in Chapter 3. In these two chapters we have studied the dynamics of the corresponding models. The most important problem was to study the conditions of abnormal synchronization in the models and to find out the regions of multistability in the parameter space where several qualitatively different solutions of the systems are simultaneously stable. These results allow to find the proper perturbation of the system providing the switching of the dynamics between different stable states. From the point of view of real application this means that appropriate stimulation technique can change crucially the system behavior switching it from unhealthy (pathologically) state to healthy (desynchronized) state. Stability of the corresponding healthy states can provide long-lasting therapeutic effect of the stimulation. In order to study this problem the basins of attraction for different coexisting states have been investigated. We have also estimated the relative sizes and structures of the basins of attraction.

In Chapter 2 we have considered the Kuramoto system of phase oscillators involving spike timing-dependent plasticity rule for the varying coupling strength. Systems under consideration have small number of oscillators $N = 2$ and $N = 3$ allowing to perform a detailed analysis of the rich system dynamics. This model reflects the behavior of several neuronal populations where each group of neurons is supposed to be strongly synchronized. In this way the interactions between different subpopulations can be investigated. This assumption justifies the consideration of a low-dimensional model. For the introduced model we have revealed coexistence of synchronized, desynchronized and clustered dynamical states for a wide range of parameter values. An important role of the non-equal values of the constants τ_p and τ_d determining time scale for the synaptic potentiation/depression processes for the multistability mechanism was also discovered. We have also described the coupling structure of different dynamical regimes in the system (2.7) and (2.8). Thus, the hierarchical unidirectional coupling structure for the synchronized solution has been found. We have also illustrated a multistability under the variation of different parameter sets. In particular the diagrams revealing the dependence of the averaged oscillator frequencies on maximal coupling strength were calculated. These diagrams describe the multistability in terms of different coupling strength among the oscillators. Figure 2.9 illustrates the stability of different solutions in the (ω_2, α) parameter plane for different values of coupling strength and natural frequencies of the oscillators. We have also considered systems of $N = 5$, $N = 10$ and $N = 20$ oscillators. These systems demonstrate the behavior similar to that in the case of low-dimensional systems. We have found the relative sizes of basins of attraction for different solutions of the systems of $N = 5$ and $N = 10$ oscillators. It was shown that there are many different states with large enough basins of attraction allowing the switching of system dynamics by appropriate perturbation.

In Chapter 3 we have considered two different phase models with time-delayed interaction. Both models consist of $N = 2$ phase oscillators. Similarly to the low-dimensional model in Chapter 2, these systems can reflect the behavior of two large interacting neuronal subpopulations where each subpopulation is supposed to be synchronized and to act as one large oscillator. The difference between two systems with time delay is that the first of them does not contain self-feedback term,

whereas the second one includes self-feedback term as well as delayed term of interaction between two oscillators. For the first system (3.2) we have investigated the appearance and stability of the different phase-locked state as coupling strength K or time delay τ increases. The fascinating coexisting of numerous desynchronized and synchronized states has been revealed for large values of time delay τ. It was shown that total number of stable synchronized states is proportional to τ, whereas the number of desynchronized stable solutions is proportional to τ^2 as τ increases. The averaged frequencies of the oscillators are arranged on a grid with the distance between the nodes proportional to $1/\tau$ provided time delay τ is large enough. We call this phenomenon *frequency discretization*. For the phase-locked solutions we have also investigated the structure of basins of attraction, which can be important for the development of stimulation techniques switching the system dynamics between different stable states. The second system (3.7) considered in Chapter 3 demonstrates even more complicated dynamics than the system without self-feedback term. Thus, we have found a supercritical Hopf bifurcation of an anti-phase synchronized solution. As a result of this bifurcation a synchronized solution with oscillating phase difference appears. This solution also demonstrates a series of period-doubling bifurcations leading to chaos. Another characteristic property of this system (3.7) is the presence of a stable desynchronized solution for large values of the coupling strength K provided the frequency detuning $\Delta\omega$ is large enough. Such specific states are shown in Figures 3.13, 3.14. The model (3.7) also exhibits the frequency discretization similarly to the the model without self-feedback term (3.2). Summarizing, we can state that models with delayed interaction (3.2) and (3.7) demonstrate fascinating multistability, which can be utilized in the medical application of this theoretical study.

The main part of the thesis, Chapter 4, was devoted to the coordinated reset (CR) stimulation technique [84,85,91]. Since this stimulation technique allows to perform mild deep brain stimulation (DBS) utilizing the internal properties of the stimulated system, the obtained results contribute to the understanding of the mechanisms of action as well as to the choice of the optimal parameter values of the coordinated reset stimulation. The idea of the CR stimulation is to provide effective suppression of the pathological synchronized activity in the certain brain areas like subthalamic

nucleus (STN) or globus pallidus external (GPe). This novel technique was developed to perform the stimulation in a milder way and to decrease some unwanted side effects of the standard high-frequency DBS. The goal of the study was to reveal the dependence of the stimulation effect on the values of the stimulation parameters and to find the optimal parameter set for the stimulation. We have considered two models of the neuronal population under the CR stimulation. The first model studied in section 4.1 is based on the Kuramoto system of coupled phase oscillators and the second model investigated in section 4.2 describes the population of FitzHugh-Nagumo neurons. For both models we have introduced the mathematical model of the CR stimulation.

As the first step of the study of the CR model based on phase oscillators, the influence of a single stimulation contact has been investigated. Afterwards the permanent CR stimulation was considered in subsection 4.1.3. We have studied the state of the system under stimulation reflected by the averaged over time order parameters, see also Figure 4.9. This figure demonstrates our important finding that the system behavior during the CR stimulation crucially depends on the value of decay coefficient σ. Small values of σ allows quite wide variation of the stimulation strength without sufficient change of the stimulation effect. On the contrary, if the values of σ are large, the system behavior is much more sensitive to the changing of the stimulation strength I. This means that for large σ the stimulation strength has to be properly adjusted in order to obtain a desired effect of the stimulation.

In subsection 4.1.4 we have investigated transient times after the stimulation is switched off. The investigation of the post-stimulus transient is very important for the practical application of the CR stimulation for DBS. Indeed, transient time allows to estimate the duration of a pause where the stimulation can be switched off. This technique allows to decrease the amount of the stimulation current administered to the brain tissue [85]. We have also considered the transient time if CR stimulation is terminated at some arbitrary moment. This study brings together the information about the system state during the stimulation and the information about the transient time from stimulus-induced state to the synchronized state during resynchronization process when the stimulation is switched off. Thus, we have investigated the optimal time of stimulation break providing the longest transient.

The dependence of the optimal transient and the corresponding stimulation break on parameters (I, σ) has been illustrated in Figure 4.16. The course of the transient process was also demonstrated by the Kuiper index technique. Summarizing our findings devoted to the transient time, the optimal transient time does not always coincide with the standard end of the CR stimulation. The difference between standard and optimal stimulation break is significant for large σ, whereas it is less appreciable for small σ.

In subsection 4.1.5 we have studied the effect of the CR stimulation for different values of the stimulation period since all previous results have been obtained for the stimulation period.Two different cases have been considered. The first case corresponded to the small variation of the stimulation period around the period of system oscillations. The second part of the study was devoted to the periods of stimulation, which are multiples of the system period. Summarizing our main results, we can state that the effect of the CR stimulation is robust with respect to small changes of the stimulation period unless the resulting system state can be different from the clustered state, which is the usual result of an appropriate stimulation. Multiplication of the stimulation period on integer constant different from the number of stimulating contacts also preserves the stimulation effect. However, if the multiplier equals the number of contacts, stimulation results in a strong undesired synchronization of the stimulated neurons.

In subsection 4.1.6 we considered the on-off CR stimulation protocol used in the real application. The intriguing dependence of the stimulation effect on the *sum* of the lengths of the stimulation and rest intervals also called by period of the on-off CR stimulation cycle has been discovered. The main result of this subsection was illustrated in Figure 4.31. If period of the on-off CR stimulation cycle is in a resonant relation with the natural mean period of the stimulated neuronal population, then the desynchronizing effect of the on-off CR stimulation is more pronounced than in the non-resonant case. The results of the optimal stimulation break from subsection 4.1.4 are also reflected in the entire diagram of the on-off stimulation effect.

The CR stimulation of the population of FitzHugh-Nagumo neurons was considered in section 4.2. To perform the analysis of the stimulation effect, two different

techniques have been used. The first one is the method of the phase-based order parameter where the event-related phases have been used. The second method is based on the amplitude of the mean field of the entire neuronal population. The standard deviation of the mean field has been taken as the estimated value. It was shown that behavior of the system of the FitzHugh-Nagumo oscillators during CR stimulation is similar to the case of the phase model. We have illustrated this phenomenon by both mentioned estimation techniques. The corresponding diagrams are shown in Figures 4.38 and 4.39.

The obtained theoretical results can contribute to the better understanding of the mechanisms of the pathological neuronal synchronization as well as to the optimization of the stimulation techniques designed for the deep brain stimulation in patients with neurological diseases like Parkinson's disease or essential tremor.

Prospects

In the present thesis we have considered a number of problems devoted to synchronized oscillator systems and to the methods of their desynchronization. However, there are several interesting aspects, which have been left for the future studies. We can mention some of those topics. First of all, it is important to consider the application of the CR stimulation to the system involving STDP (spike timing-dependent plasticity) since the crucial role of the rewiring in the human brain is nowadays well-known. The next direction of the investigation could be the study of the CR stimulation in the case of more realistic neuronal models including bursting neurons since in the present thesis only the phase model and FitzHugh-Nagumo spiking model have been considered. Thus, one can investigate a more complicated structure of the brain pacemaker, e.g., a system STN-GPe consisting of the neurons of two different types, for instance, excitatory and inhibitory neurons.

Chapter 6

Summary

For an effective control of pathological neuronal synchronization characteristic for Parkinson's disease and essential tremor by deep brain stimulation a profound understanding of synchronization mechanisms in the neuronal networks is required. This understanding can be then used to optimize the novel stimulation technique based on the coordinated reset. A modelling approach utilizing the methods of nonlinear dynamics is used to unfold the mechanism of multistability in neuronal population. In the present thesis a number of mathematical models of synchronized neuronal activity and coordinated reset (CR) stimulation are considered. The dynamical regimes of the models were investigated by analytical methods, bifurcation theory and numerical simulations.

The first model describes a neuronal oscillatory network involving spike-timing dependent synaptic plasticity (STDP). The considered systems consist of a small number of oscillators. For the introduced model the coexistence of synchronized, desynchronized and clustered states was found. The stability properties of the above states were investigated as system parameters vary. The basins of attraction of different states for the systems of $N = 5$ and $N = 10$ oscillators were described and their relative sizes were estimated.

Other considered models involve delayed interaction between oscillators including delayed feedback terms. The emergence of different stable states under variation of the coupling strength and time delay was investigated. The phenomenon of

frequency discretization for the coexisting stable synchronized and desynchronized states was discovered and described in detail. In addition, the structure of the basins of attraction for the different stable synchronized states was studied for the model with delayed interactions. It was found that the delayed self-feedback term induces a significant complication of the system dynamics leading to stabilization of desynchronized states for large coupling strength.

The common characteristic shared by the considered models with STDP and time delay was found to be the coexistence of different stable dynamical states, i.e., multistability. The obtained results allow to find a proper perturbation of the systems by external stimulation resulting in an effective switching from undesired (pathological) to desired (healthy) state. Stability of a healthy state can provide long-lasting therapeutic effect of the stimulation.

The main part of the thesis is devoted to the study of the CR stimulation technique and its optimal parameter values. Two models of the neuronal networks under the CR stimulation are considered. The first model is based on the Kuramoto phase model, whereas the second model describes a network of the FitzHugh-Nagumo oscillators. The system state imposed by the CR stimulation is described in terms of the order parameters. The influence of the stimulation strength, stimulation period and the characteristics of the neuronal tissue on the stimulation outcome was described. The study of the system post-stimulus transient allows to estimate the rest pause in the stimulation protocol important for real application. This investigation brings together the results about the system state during stimulation and results about the post-stimulus transient from stimulation-induced state to the synchronized state. The study of the on-off CR stimulation protocol revealed the influence of the lengths of the active and rest subintervals in the on-off stimulation protocol on the desynchronizing effect of the stimulation. For the model based on the network of the FitzHugh-Nagumo oscillators two methods of the estimation of the desynchronizing effect of the CR stimulation are utilized. The results of the stimulation were estimated and compared with the analysis of the CR stimulation of the phase model. The common properties of the CR stimulation responses for both models were shown. The obtained results contribute to the understanding and optimization of the stimulation methods designed for deep brain stimulation.

Chapter 7

Zusammenfassung

Für die effektive Kontrolle pathologischer neuronaler Synchronisation, die für die Parkinson'sche Krankheit und den essentiellen Tremor charakteristisch ist, ist ein profundes Verständnis der Mechanismen der Synchronisation in neuronalen Netzwerken nötig. Dieses Verständnis kann benutzt werden, um das neuartige Stimulationsverfahren der tiefen Hirnstimulation, das auf Coordinated Reset (CR) basiert, zu optimieren. Die modellbasierenden Methoden nichtlinearer Dynamik werden benutzt, um den Mechanismus der Multistabilität in neuronalen Populationen zu untersuchen. In der vorgelegten Doktorarbeit wurden verschiedene mathematische Modelle für synchronisierte neuronale Aktivität und Coordinated Reset Stimulation betrachtet. Die dynamischen Regime der Modelle wurden mittels analytischer Methoden, der Bifurkationstheorie und numerischer Simulationen untersucht.

Das erste verwendete Modell beschreibt ein neuronales oszillierendes Netzwerk, das insbesondere synaptische Plastizität (STDP) berücksichtigt. Die betrachteten Systeme bestehen aus einer kleinen Anzahl von Oszillatoren. Für die eingeführten Modelle wurde die Koexistenz von synchronisierten, desynchronisierten und sogenannten Cluster-Zuständen gefunden. Die Stabilitätseigenschaften der vorgegebenen Zustände wurden untersucht, wobei die Systemparameter variiert wurden. Die Einzugsgebiete der unterschiedlichen Zustände für die Systeme von $N = 5$ und $N = 10$ Oszillatoren wurden beschrieben und ihre relative Größe wurde bewertet.

Die weiterhin betrachteten Modelle berücksichtigen eine zeitverzögerte Interaktion

zwischen den Oszillatoren und ein zeitverzögertes Feedback. Das Entstehen von verschiedenen stabilen Zuständen wurde untersucht, wobei die Kopplungsstärke und die Zeitverzögerung variiert wurde. Das Phänomen der Frequenzdiskretisierung für die koexistierenden stabilen synchronisierten und desynchronisierten Zustände wurde entdeckt und detalliert beschrieben. Außerdem wurde die Struktur der Einzugsgebiete der verschiedenen stabilen synchronisierten Zustände für das Modell mit zeitverzögerter Interaktion untersucht. Zeitverzögertes Feedback führt zu einer signifikanten Komplikation der Systemdynamik, die zu einer Stabilisierung desynchronisierter Zustände für starke Kopplung führt.

Die allgemeine Charakteristik, die bei beiden betrachteten Modellen mit STDP und Zeitverzögerung beobachtet wurde, ist die Koexistenz von verschiedenen dynamischen Zuständen, d.h. Multistabilität. Die Ergebnisse unterstützen die Entwickling einer effektiven Störung von Systemen mittels einer externen Stimulation, die eine zielgerichtete Umschaltung von dem nicht erwünschten (pathologischen) zu dem erwünschten (gesunden) Zustand zur Folge hat. Die Stabilität des gesunden Zustandes kann dauerhafte therapeutische Effekte der Stimulation gewährleisten.

Der Hauptteil der vorgelegten Doktorarbeit ist mit der Untersuchung der CR Stimulationstechnik und ihren optimalen Parameterwerten befasst. Zwei Modelle von neuronalen Netzwerken unter CR Stimulation wurden betrachtet. Das erste Modell basiert auf dem Kuramoto Phasenmodell; das zweite Modell beschreibt ein Netzwerk von FitzHugh-Nagumo Neuronen. Der bei der CR Stimulation entstehende Systemzustand wurde mittels Ordnungsparametern beschrieben. Der Einfluss der Stimulationsstärke, Stimulationsperiode und der Charakteristiken des neuronalen Gewebes auf das Resultat der Stimulation wurde beschrieben. Die Studie der Post-Stimulus-Transientzeit des Systems ermöglicht, die Stimulation-Pause in dem Stimulationsprotokoll, die für die reale Applikation wichtig ist, zu bewerten. Diese Untersuchung analysiert die Ergebnisse bezüglich des Systemzustands während der Stimulation und die Ergebnisse bezüglich der Post-Stimulus-Transientzeit des Systemzustands. Die Untersuchung der On-Off-Phasen im CR Stimulationsprotokoll bellegt den Einfluss der Länge des aktiven Intervalls und des Ruheintervalls. Für das auf einem Netzwerk von FitzHugh-Nagumo Oszillatoren basierende Modell wurden zwei Methoden zur Bewertung des Desynchronisierungseffekts angewendet. Die

Resultate der Stimulation wurden bewertet und mit der Analyse der CR Stimulation des Phasenmodells vergleichen. Die allgemeinen Eigenschaften der Antworten der beiden Modelle auf die CR Stimulation wurden dargestellt. Die Ergebnisse tragen zu einem tieferen Verständnis und zu einer Optimierung der Stimulationsmethoden bei, die für die tiefe Hirnstimulation entwickelt wurden.

Chapter 8

References

[1] Abbott, L. F., and Nelson, S. B. Synaptic plasticity: taming the beast. *Nature Neuroscience 3* (2000), 1178–1183.

[2] Albin, R. L., Young, A. B., and Penney, J. B. The functional anatomy of basal ganglia disorders. *Trends in Neurosciences 12*, 10 (1989), 366–375.

[3] Amtage, F., Henschel, K., Schelter, B., Vesper, J., Timmer, J., Lücking, C. H., and Hellwig, B. Tremor-correlated neuronal activity in the subthalamic nucleus of parkinsonian patients. *Neuroscience Letters 442* (2008), 195–199.

[4] Atay, F. M. Distributed delays facilitate amplitude death of coupled oscillators. *Phys. Rev. Lett. 91*, 9 (2003), 094101.

[5] Benabid, A., Benazzous, A., and Pollak, P. Mechanisms of deep brain stimulation. *Movement Disorders 17*, 3 (2002), 73–74.

[6] Benabid, A., Pollak, P., Gervason, C., Hoffmann, D., Gao, D., Hommel, M., Perret, J., and de Rougemount, J. Longterm suppression of tremor by chronic stimulation of ventral intermediate thalamic nucleus. *The Lancet 337*, 8738 (1991), 403–406.

[7] Benabid, A. L., Benazzouz, A., Hoffmann, D., Limousin, P., Krack, P., and Pollak, P. Long-term electrical inhibition of deep brain targets in movement disorders. *Movement Disorders 3* (1998), 119–125.

[8] Bergman, H., Feingold, A., Nini, A., Raz, A., Slovin, H., Abeles, M., and Vaadia, E. Physiological aspects of information processing in the basal ganglia of normal and parkinsonian primates. *Trends Neurosci. 21* (1998), 32–38.

[9] Bergman, H., Wichmann, T., Karmon, B., and DeLong, M. R. The primate subthalamic nucleus. II. neuronal activity in the MPTP model of parkinsonism. *Journal of Neurophysiology 72*, 2 (1994), 507–520.

[10] Best, E. N. Null space in the Hodgkin-Huxley equations. *Biophys. J. 27* (1979), 87–104.

[11] Beurrier, C., Bioulac, B., Audin, J., and Hammond, C. High-frequency stimulation produces a transient blockade of voltage-gated currents in subthalamic neurons. *Journal of Neurophysiology 85(4)* (2001), 1351–1356.

[12] Bevan, M. D., Magill, P. J., Terman, D., Bolam, J. P., and Wilson, C. J. Move to the rhythm: oscillations in the subthalamic nucleus-external globus pallidus network. *TRENDS in Neurosciences 25*, 10 (2002), 525–531.

[13] Bi, G. Q. Spatiotemporal specificity of synaptic plasticity: cellular rules and mechanismsl. *Biological Cybernetics 87* (2002), 319–332.

[14] Bi, G. Q., and Poo, M. Synaptic modifications in cultured hippocampal neurons: Dependence on spike timing, synaptic strength, and postsynaptic cell type. *Journal of Neuroscience 18*, 24 (1998), 10464–10472.

[15] Blond, S., Caparros-Lefebvre, D., Parker, F., Assaker, R., Petit, H., Guieu, J.-D., and Christiaens, J.-L. Control of tremor and involuntary movement disorders by chronic stereotactic stimulation of the ventral intermediate thalamic nucleus. *Journal of Neurosurgery 77* (1992), 62–68.

[16] Brown, P., Oliviero, A., Mazzone, P., Insola, A., Tonali, P., and Di Lazzaro, V. Dopamine dependency of oscillations between subthalamic nucleus and pallidum in Parkinson's disease. *Journal of Neuroscience 21* (2001), 1033–1038.

[17] Brown, P., and Williams, D. Basal ganglia local field potential activity: Character and functional significance in the human. *Clinical Neurophysiology 116* (2005), 2510–2519.

[18] Buck, J. Synchronous rhythmic flashing of fireflies. ii. *The Quarterly Review of Biology 63*, 3 (1988), 265–286.

[19] Campbell, S. A., Ncube, I., and Wu, J. Multistability and stable asynchronous periodic oscillations in a multiple-delayed neural system. *Physica D 214* (2006), 101–119.

[20] Cymbalyuk, G. S., and Calabrese, R. L. Oscillatory behaviors in pharmacologically isolated heart interneurons from the medicinal leech. *Neurocomputing 32–33* (2000), 97–104.

[21] Dan, Y., and Poo, M. Spike timing-dependent plasticity: From synapse to perception. *Physiol. Rev. 86* (2006), 1033–1048.

[22] Deuschl, G., Raethjen, J., Baron, R., Lindemann, M., Wilms, H., and Krack, P. The pathophysiology of parkinsonian tremor: a review. *Journal of Neurology 247*, Suppl 5 (2000), V/33–V/48.

[23] FitzHugh, R. Impulses and physiological states in theoretical models of nerve membrane. *Biophysical Journal 1*, 6 (1961), 445–466.

[24] Garcia, L., Audin, J., D'Alessandro, G., Bioulac, B., and Hammond, C. Dual effect of high-frequency stimulation on subthalamic neuron activity. *Journal of Neuroscience 23*, 25 (2003), 8743–8751.

[25] Garcia, L., D'Alessandro, G., Fernagut, P.-O., Bioulac, B., and Hammond, C. Impact of high-frequency stimulation parameters on the pattern of discharge of subthalamic neurons. *Journal of Neurophysiology 94* (2005), 3662–3669.

[26] Gerstner, W., and Kistler, W. M. *Spiking Neuron Models*. Cambridge University Press, Cambridge, UK, 2002.

[27] Glass, L., and MacKey, M. C. *From clocks to chaos: the rhythms of life*. Princeton University Press, Princeton, N.J., 1988.

[28] Hadamschek, V. *Brain stimulation techniques with the aid of nonlinear delayed neurofeedback and MEG inverse methods*. PhD thesis, Technische Universität Berlin, 2006.

[29] Haken, H. *Advanced synergetics*. Springer, Berlin, 1983.

[30] Hauptmann, C., Popovych, O., and Tass, P. A. Delayed feedback control of synchronization in locally coupled neuronal networks. *Neurocomputing 65-66* (2005), 759–767.

[31] Hauptmann, C., Popovych, O., and Tass, P. A. Effectively desynchronizing deep brain stimulation based on a coordinated delayed feedback stimulation via several sites: a computational study. *Biological Cybernetics 93* (2005), 463–470.

[32] Hauptmann, C., Popovych, O., and Tass, P. A. Multisite coordinated delayed feedback for an effective desynchronization of neuronal networks. *Stochastics and Dynamics 5*, 2 (2005), 307–319.

[33] Hauptmann, C., Popovych, O., and Tass, P. A. Demand-controlled desynchronization of oscillatory networks by means of a multisite delayed feedback stimulation. *Comput. Visual Sci.* (2007), DOI 10.1007/s00791–006–0034–9.

[34] Hauptmann, C., Popovych, O., and Tass, P. A. Desynchronizing the abnormally synchronized neural activity in the suthalamic nucleus: a modeling study. *Expert Rev. Med. Devices 4*, 5 (2007), 633–650.

[35] Hauptmann, C., and Tass, P. A. Therapeutic rewiring by means of desynchronizing brain stimulation. *BioSystems 89* (2007), 173–181.

[36] Hauptmann, C., and Tass, P. A. Cumulative and after-effects of short and weak coordinated reset stimulation: a modeling study. *Journal of Neural Engineering 6* (2009), 016004.

[37] Hindmarsh, J., and Rose, R. A model of neuronal bursting using three coupled first order differential equations. *Proc. R. Soc. Lond. B. 221* (1984), 87–102.

[38] Hodgkin, A. L., and Huxley, A. F. A quantitative description of membrane current and application to conduction and excitation. *Journal of Physiology 117* (1952), 500–544.

[39] Hopfield, J. J. Neurons with graded response have collective computational properties like those of two-state neurons. *Proc. Natl. Acad. Sci. USA 81* (1984), 3088–3092.

[40] Izhikevich, E. M. *Dynamical Systems in Neuroscience: The Geometry of Excitability and Bursting*. The MIT Press, 2005.

[41] Karbowski, J., and Ermentrout, G. B. Synchrony arising from a balanced synaptic plasticity in a network of heterogeneous neural oscillators. *Phys. Rev. E 65* (2002), 031902.

[42] Knight, B. W. Dynamics of encoding in a population of neurons. *The Journal of General Physiology 59* (1972), 734–766.

[43] Koch, M., Mostert, J., Heersema, D., and Keyser, J. D. Tremor in multiple sclerosis. *J. Neurol. 254* (2007), 113–145.

[44] Krachkovskyi, V. *Stimulus-induzierte Desynchronisation von gekoppelten Oszillatoren mit Zeitverzögerung: Theorie und Anwendung bei neurologischen Patienten*. PhD thesis, Universität zu Köln, 2006.

[45] Krachkovskyi, V., Popovych, O. V., and Tass, P. A. Stimulus-locked responses of two phase oscillators coupled with delayed feedback. *Phys. Rev. E 73*, 6 (2006), 066220.

[46] Kühn, A. A., Doyle, L., Pogosyan, A., Yarrow, K., Kupsch, A., Schneider, G.-H., Hariz, M. I., Trottenberg, T., and Brown, P. Modulation of beta oscillations in the subthalamic area during motor imagery in Parkinson's disease. *Brain 129* (2006), 695–706.

[47] Kühn, A. A., Kupsch, A., Schneider, G.-H., and Brown, P. Reduction in subthalamic 8-35 Hz oscillatory activity correlates with clinical improvement in Parkinson's disease. *European Journal of Neuroscience 23* (2006), 1956–1960.

[48] Kuramoto, Y. *Chemical oscillations, waves, and turbulence.* Springer, Berlin Heidelberg New York, 1984.

[49] Kuznetsov, Y. A. *Elements of applied bifurcation theory.* Springer, New York, 1998.

[50] Levy, R., Aschby, P., Hutchinson, W. D., Lang, A. E., Lozano, A. M., and Dostrovsky, J. O. Dependence of subthalamic nucleus oscillations on movement and dopamine in Parkinson's disease. *Brain 125* (2002), 1196–1209.

[51] Levy, R., Hutchison, W. D., Lozano, A. M., and Dostrovsky, J. O. High-frequency synchronization of neuronal activity in the subthalamic nucleus of parkinsonian patients with limb tremor. *The Journal of Neuroscience 20* (2000), 7766–7775.

[52] Lysyansky, B., Maistrenko, Y. L., and Tass, P. A. Coexistence of numerous synchronized and desynchronized states in a model of two phase oscillators coupled with delay. *International Journal of Bifurcation and Chaos 18*, 6 (2008), 1791–1800.

[53] Maistrenko, Y. L., Lysyansky, B., Hauptmann, C., Burylko, O., and Tass, P. A. Multistability in the Kuramoto model with synaptic plasticity. *Phys. Rev. E 75* (2007), 066207.

[54] Markram, H., Lübke, J., Frotscher, M., and Sakmann, B. Regulation of synaptic efficacy by coincidence of postsynaptic APs and EPSPs. *Science 275* (1997), 213–215.

[55] Morris, C., and Lecar, H. Voltage oscillations in the barnacle giant muscle fiber. *Biophysical Journal 35*, 1 (1981), 193–213.

[56] Niebur, E., Schuster, H. G., and Kammen, D. M. Collective frequencies and metastability in networks of limit-cycle oscillators with time delay. *Phys. Rev. Lett. 67* (1991), 2753–2756.

[57] Nini, A., Feingold, A., Slovin, H., and Bergman, H. Neurons in the globus pallidus do not show correlated activity in the normal monkey, but phase-locked oscillations appear in the MPTP model of parkinsonism. *Journal of Neurophysiology 74* (1995), 1800–1805.

[58] Peskin, C. S. *Mathematical aspects of heart physiology.* Courant Institute of Mathematical Sciences, New-York, 1975.

[59] Pikovsky, A., Rosenblum, M., and Kurths, J. *Synchronization, a universal concept in nonlinear sciences.* Cambridge University Press, Cambridge, 2001.

[60] Plenz, D., and Kital, S. T. A basal ganglia pacemaker formed by the subthalamic nucleus and external globus pallidus. *Nature 400* (1999), 677–682.

[61] Popovych, O., Hauptmann, C., and Tass, P. A. Effective desynchronization by nonlinear delayed feedback. *Phys. Rev. Lett. 94* (2005), 164102.

[62] Popovych, O. V., Hauptmann, C., and Tass, P. A. Control of neuronal synchrony by nonlinear delayed feedback. *Biological Cybernetics 95* (2006), 69–85.

[63] Popovych, O. V., Hauptmann, C., and Tass, P. A. Desynchronization and decoupling of interacting oscillators by nonlinear delayed feedback. *International Journal of Bifurcation and Chaos 16*, 7 (2006), 1977–1987.

[64] Ramana Reddy, D. V., Sen, A., and Johnston, G. L. Time delay induced death in coupled limit cycle oscillators. *Phys. Rev. Lett. 80*, 23 (1998), 5109–5112.

[65] Richardson, K. A., Gluckman, B. J., Weinstein, S. L., Glosch, C. E., Moon, J. B., Gwinn, R. P., Gale, K., and Schiff, S. J. In vivo modulation of hippocampal epileptiform activity with radial electric fields. *Epilepsia 44*, 6 (2003), 768–777.

[66] Rinzel, J., and Ermentrout, G. Analysis of neural excitability and oscillations. In *Methods in Neuronal Modelling From Synapses to Networks*, C. H. Koch and I. Segev, Eds. MIT Press, Cambridge, MA, 1989, pp. 135–169.

[67] Rivlin-Etzion, M., Marmor, O., Heimer, G., Raz, A., Nini, A., and Bergman, H. Basal ganglia oscillations and pathophysiology of movement disorders. *Curr. Opin. Neurobiol. 16*, 6 (2006), 629–637.

[68] Rodriguez-Oroz, M. C., Obeso, J. A., Lang, A. E., Houeto, J.-L., Pollak, P., Rehncrona, S., Kulisevsky, J., Albanese, A., Volkmann, J., Hariz, M. I., Quinn, N. P., Speelman, J. D., Guridi, J., Zamarbide, I., Gironell, A., Molet, J., Pascual-Sedano, B., Pidoux, B., Bonnet, A. M., Agid, Y., Xie, J., Benabid, A.-L., Lozano, A. M., Saint-Cyr, J., Romito, L., Contarino, M. F., Scerrati, M., Fraix, V., and Blercom, N. V. Bilateral deep brain stimulation in Parkinson's disease: a multicentre study with 4 years follow-up. *Brain 128*, 10 (2005), 2240–2249.

[69] Rosenblum, M. G., and Pikovsky, A. S. Controlling synchronization in an ensemble of globally coupled oscillators. *Phys. Rev. Lett. 92* (2004), 114102.

[70] Rubin, J. E., and Terman, D. High frequency stimulation of the subthalamic nucleus eliminates pathological thalamic rhythmicity in a computational model. *Journal of Computational Neuroscience 16* (2004), 211–235.

[71] Schuster, H. G., and Wagner, P. Mutual entrainment of two limit cycle oscillators with time delayed coupling. *Prog. Theor. Phys. 81* (1989), 939–945.

[72] Schuurman, P. R., Bosch, D. A., Bossuyt, P. M., Bonsel, G. J., van Someren, E. J., de Bie, R. M., Merkus, M. P., and Speelman, J. D. A comparison of continuous thalamic stimulation and thalamotomy for suppression of severe tremor. *N. Engl. J. Med. 342*, 7 (2000), 461–468.

[73] Seliger, P., Young, S. C., and Tsimring, L. S. Plasticity and learning in a network of coupled phase oscillators. *Phys. Rev. E 65*, 4 (Mar 2002), 041906.

[74] Shilnikov, A., Calabrese, R. L., and Cymbalyuk, G. Mechanism of bistability: Tonic spiking and bursting in a neuron model. *Physical Review E 71* (2005), 056214.

[75] Shriki, O., Hansel, D., and Sompolinsky, H. Rate models for conductance-based cortical neuronal networks. *Neural Computation 15*, 8 (2003), 1809–1841.

[76] Smirnov, D. A., Barnikol, U. B., Barnikol, T. T., Bezruchko, B. P., Hauptmann, C., Bührle, C., Maarouf, M., Sturm, V., Freund, H.-J., and Tass, P. A. The generation of Parkinsonian tremor as revealed by directional coupling analysis. *Europhysics Letters 83* (2008), 20003.

[77] Strogatz, S. H. From Kuramoto to Crawford: exploring the onset of synchronization in populations of coupled oscillators. *Physica D 143*, 1-4 (2000), 1–20.

[78] Tasker, R. R. Depp brain stimulation is preferable to thalamotomy for tremor suppression. *Surgical Neurology 49* (1998), 145–154.

[79] Tass, P. A. *Phase resetting in medicine and biology: stochastic modelling and data analysis*. Springer, Berlin, 1999.

[80] Tass, P. A. Desynchronizing double-pulse phase resetting and application to deep brain stimulation. *Biological Cybernetics 85* (2001), 343–354.

[81] Tass, P. A. Effective desynchronization by means of double-pulse phase resetting. *Europhys. Lett. 53*, 1 (2001), 15–21.

[82] Tass, P. A. Effective desynchronization with a resetting pulse train followed by a single pulse. *Europhys. Lett. 55*, 2 (2001), 171–177.

[83] Tass, P. A. Desynchronization of brain rhythms with soft phase-resetting techniques. *Biological Cybernetics 87* (2002), 102–115.

[84] Tass, P. A. Desynchronization by means of a coordinated reset of neural subpopulations - a novel technique for demand-controlled deep brain stimulation. *Prog. Theor. Phys. Suppl. 150* (2003), 281–296.

[85] Tass, P. A. A model of desynchronizing deep brain stimulation with a demand-controlled coordinated reset of neural subpopulations. *Biological Cybernetics 89* (2003), 81–88.

[86] Tass, P. A. Stochastic phase resetting of stimulus-locked responses of two coupled oscillators: Transient response clustering, synchronization, and desynchronization. *Chaos 13*, 1 (2003), 364–376.

[87] Tass, P. A. Stochastic phase resetting of two coupled phase oscillators stimulated at different times. *Phys. Rev. E 67* (2003), 051902.

[88] Tass, P. A. Transmission of stimulus-locked responses in two coupled phase oscillators. *Phys. Rev. E 69* (2004), 051909.

[89] Tass, P. A., and Hauptmann, C. Long-term anti-kindling effects induced by short-term, weak desynchronizing stimulation. *Nonl. Phen. Compl. Syst. 9* (2006), 298–312.

[90] Tass, P. A., Hauptmann, C., and Popovych, O. V. Development of therapeutic brain stimulation techniques with methods from nonlinear dynamics and statistical physics. *International Journal of Bifurcation and Chaos 16*, 7 (2006), 1889–1911.

[91] Tass, P. A., and Majtanik, M. Long-term anti-kindling effects of desynchronizing brain stimulation: a theoretical study. *Biological Cybernetics 94*, 1 (2006), 58–66.

[92] Tass, P. A., Rosenblum, M. G., Weule, J., Kurths, J., Pikovsky, A., Volkmann, J., Schnitzler, A., and Freund, H.-J. Detection of $n : m$ phase locking from noisy data: Application to magnetoencephalography. *Phys. Rev. Lett. 81*, 15 (1998), 3291–3294.

[93] Terman, D. An introduction to dynamical systems and neuronal dynamics. In *Tutorials in Mathematical Biosciences I*, vol. 1860 of *Lecture Notes in Mathematics*. Springer, Berlin Heidelberg, 2005, pp. 21–68.

[94] Terman, D., Rubin, J. E., Yew, A. C., and Wilson, C. J. Activity patterns in a model for the subthalamopallidal network of the basal ganglia. *Journal of Neuroscience 22* (2002), 2963–2976.

[95] Timmermann, L., Gross, J., Dirks, M., Volkmann, J., Freund, H.-J., and Schnitzler, A. The cerebral oscillatory network of parkinsonian resting tremor. *Brain 126* (2003), 199–212.

[96] van der Pol, B. On "relaxation-oscillations". *The London, Edinburgh, and Dublin Philosophical Magazine and Journal of Science. Ser. 7 2* (1926), 978–992.

[97] van der Pol, B., and van der Mark, J. The heartbeat considered as a relaxation oscillation, and an electrical model of the heart. *The London, Edinburgh, and Dublin Philosophical Magazine and Journal of Science Ser.7 6* (1928), 763–775.

[98] Volkmann, J. Deep brain stimulation for the treatment of Parkinson's disease. *J. Clin. Neurophysiol. 21* (2004), 6–17.

[99] Wichmann, T., Bergman, H., Starr, P. A., Subramanian, T., Watts, R. L., and DeLong, M. R. Comparison of MPTP-induced changes in spontaneous neuronal discharge in the internal pallidal segment and in the

substantia nigra pars reticulata in primates. *Exper. Brain Res. 125* (1999), 397–409.

[100] Winfree, A. T. Biological rhythms and the behavior of populations of coupled oscillators. *J. Theoret. Biol. 16* (1967), 15–42.

[101] Winfree, A. T. *The geometry of biological time*. Springer, Berlin, 1980.

[102] Wünsche, H.-J., Bauer, S., Kreissl, J., Ushakov, O., Korneyev, N., Henneberger, F., Wille, E., Erzgraber, H., Peil, M., Elsasser, W., and Fischer, I. Synchronization of delay-coupled oscillators: A study of semiconductor lasers. *Phys. Rev. Lett. 94*, 16 (2005), 163901.

[103] Yanchuk, S. Discretization of frequencies in delay coupled oscillators. *Phys. Rev. E 72*, 3 (2005), 036205.

[104] Yeung, M. K. S., and Strogatz, S. H. Time delay in the Kuramoto model of coupled oscillators. *Phys. Rev. Lett. 82*, 3 (1999), 648–651.

[105] Yousif, N., and Liu, X. Modeling the current distribution across the depth electrode – brain interface in deep brain stimulation. *Expert Rev. Med. Devices 4*, 5 (2007), 623–631.

Chapter 9

Preliminary publications

1. Lysyansky, B., Maistrenko, Y. L., & Tass, P. A. (2008). Coexistence of numerous synchronized and desynchronized states in a model of two phase oscillators coupled with delay. *International Journal of Bifurcation and Chaos*, 18(6), 1791–1800.

2. Maistrenko Y. L., Lysyansky, B., Hauptmann, C., Burylko, O., & Tass, P. A. (2007). Multistability in the Kuramoto model with synaptic plasticity. *Phys. Rev. E*, 75, 066207.

Chapter 10

Lebenslauf

Borys Lysyansky, geboren am 21 Oktober 1982 in Kiew, Ukraine,

Nationalität: ukrainisch

Eltern: Vater: Igor Lysyanskyy, geboren am 17.12.1948 in Kiew
Mutter: Soffa Lysianska, geboren am 28.10.1947 in Weissrussland

Privatadresse: Friedrich-Ebert-Str. 39, 52428 Jülich

Familienstand: ledig

Arbeitsstelle: Doktorand am Forschungszentrum Jülich GmbH
Institut für Neurowissenschaften und Medizin – 7
Tel.: +49-2461-616582, +49-178-5597153
E-mail: b.lysyansky@fz-juelich.de

Ausbildung

1989–1999 Reifezeugnis mit Auszeichnung (Goldene Medaille), Schule N145, Kiew

1999–2003 Bachelor der Mathematik, Kiewer Nationale Universität, Mechanisch-Mathematische Fakultät, Diplom mit Auszeichnung

2003–2005 Magister der Mathematik, Kiewer Nationale Universität, Mechanisch-Mathematische Fakultät, Diplom mit Auszeichnung

Diplomarbeit

Titel: A priori Abschätzungen von Lösungen der parabolischen Randwertprobleme im Bereich mit zugespitztem Punkt

Diplombetreuer: Dr. Igor Romanenko, Dozent, Kiewer Nationale Universität

Note: Ausgezeichnet

Arbeitserfahrung

09-12.2003, 07-10.2004 **Gastwissenschaftler,** Forschungszentrum Jülich GmbH, INB-3, MEG und DBS Arbeitsgruppe

2005–2009 **Doktorand,** Forschungszentrum Jülich GmbH, INM-7 (Neuromodulation). Betreuer: Prof. Dr. Dr. P. A. Tass, Jülich

Tagungsbeiträge

2004 CML-2004, Paris

2005 Seminarbeitrag, WIAS, Berlin

2006 6^{th} Crimean School "Nonlinear Dynamics, Chaos and Application", Yalta

2006 Workshop "Complex Dynamics and Delay Effects in Coupled Systems", WIAS, Berlin

2007 School "Dynamical Chaos and its Application", Moscow

2008 Workshop "Mathematical Modeling in Neuroscience", Kiev

2008 Workshop "Complex Dynamics of Large Coupled Systems", WIAS, Berlin

Wissenschaftliche Publikationen

1. Y. L. Maistrenko, B. Lysyansky, Ch. Hauptmann, O. Burylko, and P. A. Tass. Multistability in the Kuramoto model with synaptic plasticity, Phys. Rev. E 75, 066207 (2007)

2. B. Lysyansky, Y. L. Maistrenko, and P. A. Tass. Coexistence of numerous synchronized and desynchronized states in a model of two phase ocillators coupled with delay, International Journal of Bifurcation and Chaos, Vol. 18, Issue 6, pages 1791–1800 (2008)

Wissenschaftliche Interessen

- Modelierung der Tiefenhirnstimulation
- Mathematische Untersuchung neuronaler Aktivität und neuronaler Synchronisation
- Anwendung von Methoden nichtlinearer Dynamik in Biologie und Medizin
- Komplexe dynamische Systeme